AEOSR-TR- 94 0305

USC

*Competition Between Electromagnetic Modes in a Free-Electron Maser**

AD-A279 546

Alan H. McCurdy

Department of Electrical Engineering, University of Southern California, Los Angeles, CA 90089-0271

Final Technical Report for AFOSR Grant # AFOSR-90-0155

for the period

March 1, 1990 to February 28, 1994

DTIC
ELECTE
MAY 23 1994
S   B   D
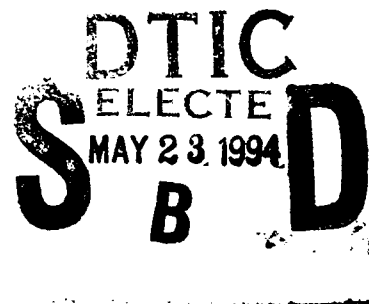
Prepared for the Air Force Office of Scientific Research,
Division of Plasma Physics AFOSR/NP ,
Bolling Air Force Base, Washington D.C. 20332-6448

94-15208

94   5   20   005

FINAL   01 Mar 90 TO 28 Feb 94

Competition Between Electromagnetic Modes in a
Free-Electron Maser

AFOSR-90-0155

Dr Alan H. McCurdy

University of Southern California
Department of Electrical Engineering
University Park CA 90089

AFOSR-TR· 94 0305

AFOSR/NE
110 Duncan Avenue, Suite B115
Bolling AFB Washington DC 20332-0001
Dr Robert Barker

2305 ES

11. Supp

A three part report is presented describing the mode competition in a gyroton
oscillator with two competing electromagentic modes. Part I gives the theory
of this mode coupling is presented using a quasi-linear assumption which is
valid for small power levels. The results are interpreted in terms of the
phase plane. These general results are applied to a specific case of mode
competition, that between TE_{101} and TE_{011} modes in a cavity of rectangular
cross section. Part II presents the theory of coupling which amy occur
between any number of cavity modes through finite conductivity in the cavity
walls, holes in the conducting cavity walls, or though interaction with an
electron beam. Part III details the experimental work. The electrodynamic
circuit is described as are microwave and electron beam diagnostics. Results
of initial tests are also given.

14. SUBJECT

17. SECURITY CLASSIFICATION OF REPORT	18. SECURITY CLASSIFICATION OF THIS PAGE	19. SECURITY	
UNCLASSIFIED	UNCLASSIFIED	UNCLASSIFIED	UNLIMITED

NSN 7540-01-280-5500
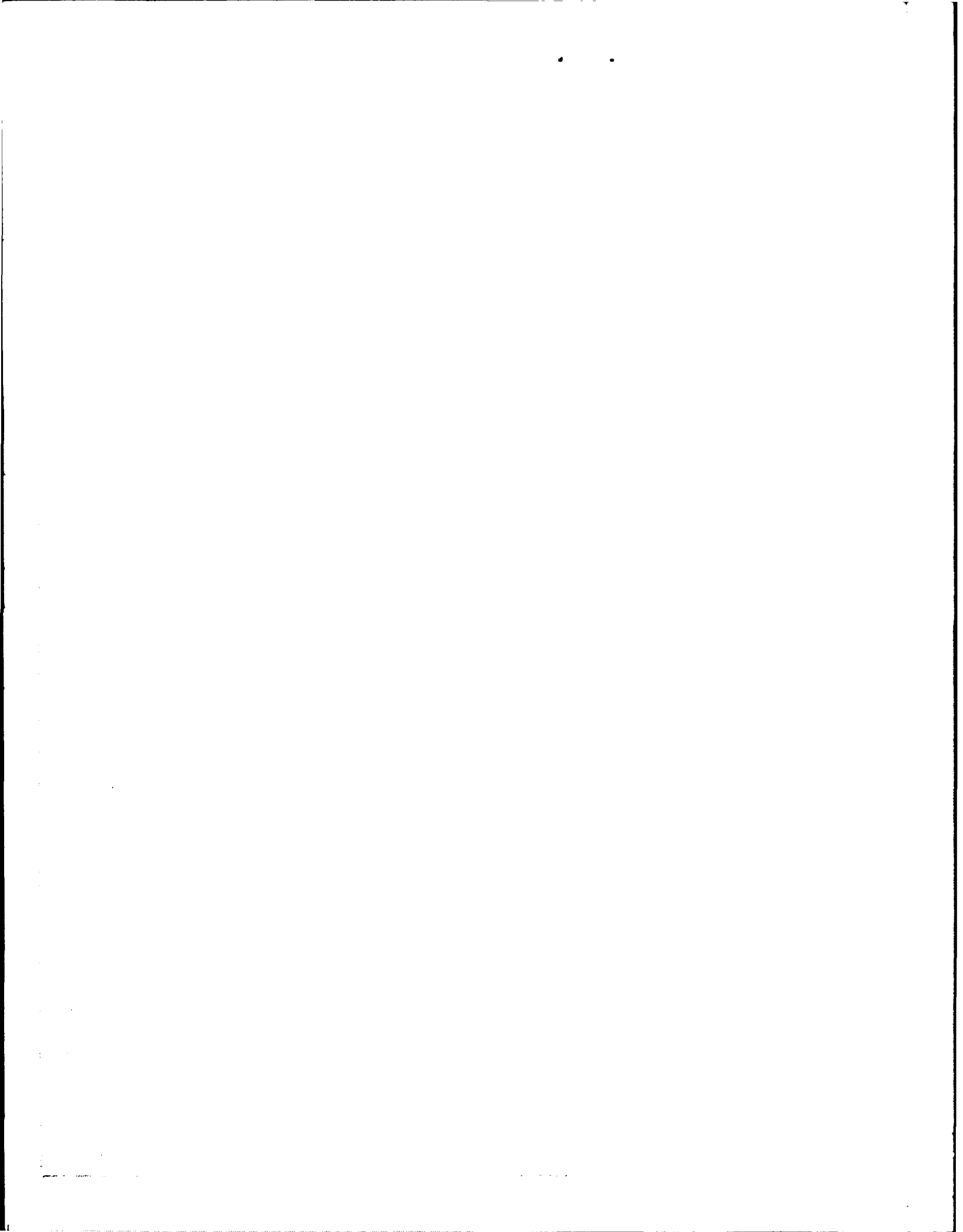
Competition Between Electromagnetic Modes
in a
Free-Electron Maser

Abstract

A three part report is presented describing the mode competition in a gyrotron oscillator with two competing electromagnetic modes. Part I gives the theory of this mode coupling is presented using a quasi-linear assumption which is valid for small power levels. The results are interpreted in terms of the phase plane. These general results are applied to a specific case of mode competition, that between TE_{101} and TE_{011} modes in a cavity of rectangular cross section. Part II presents the theory of coupling which may occur between any number of cavity modes through finite conductivity in the cavity walls, holes in the conducting cavity walls, or though interaction with an electron beam. Part III details the experimental work. The electrodynamic circuit is described as are microwave and electron beam diagnostics. Results of initial tests are also given.

2

Contents

3

PART I

Mode Interaction through Amplitudes and Phases
in a Two-Mode Gyrotron Oscillator

Abstract - Part I

An analysis is made of the temporal evolution of electromagnetic modes in a two-mode gyrotron oscillator characterized by phase and amplitude interaction through the terms linear in the oscillator power. The problem is solved in the context of amplitudes and phases which vary slowly compared to the period of oscillation. Specific reference is made to competition between TE_{11q} modes in a closed cavity gyrotron. Qualitative features which are found include phase locking, beat frequencies, periodic pulling and mode excitation. This work has applicability when the frequency separation between the modes is on the order of the frequency bandwidth of each mode, or the modes are equally spaced in frequency. Gyrotrons of this type include those with low quality factor modes or degenerate modes. Phase interaction in the case of equally spaced cavity modes is of importance in analyzing mode locking phenomena.

I. INTRODUCTION

Operation of high power microwave oscillators at high frequencies typically involves the competition between many electromagnetic modes. In vircators [1] and gyrotrons [2], researchers have attempted to optimize the devices for power and efficiency in spite of multi-mode effects. In many cases the modes are spaced far apart in frequency compared to the modal linewidth. If the modes are unequally spaced in frequency then they will interact primarily through their amplitudes. However, in the cases where 1) the modal quality factors are such that modes are approximately equally spaced in frequency: $2\,\omega_2 - \omega_3 - \omega_1 \sim \omega_2/Q$ (Q is the loaded cavity quality factor) or 2) the modal lineshapes directly overlap $\omega_2 - \omega_1 < \omega_2/Q$ then the relative phase between the modes will play an integral role in the temporal evolution. Several factors tend to enhance the probability that one of these cases will be realized in practice. First, high frequency oscillators typically have closely spaced modes simply because the mode spacing varies as λ^n, where λ is the wavelength and n is a positive number. Secondly, it is often desired to keep the energy density stored in the cavity at a minimum. For a high output power oscillator this implies that the cavity modal quality factors will be low. Thus it is important to study the case where phase interaction between modes is possible. A closely related problem is that of the phase locking of two strongly coupled oscillators, such as magnetrons [3]. It is to be noted, however, that in the magnetron locking problem there is an intrinsic time delay due to the physical separation of the oscillators. Here the modes communicate instantaneously since they are not separated in space.

This work complements previous theoretical work on gyrotron mode competition in that 1) it is in the spirit of the analytical rate equation approach of [4] rather than the largely numerical work of [2], [5], and [6] and 2) it emphasizes the low quality factor regime where phase interaction occurs. The complication due to the inclusion of phases in the rate equations goes so far as to provide phase coupling through the linear terms. Hence there is no regime of unimpeded linear modal growth. Of particular concern here is the temporal evolution of the modes and the nature of the final steady state. An analysis of the effects of these phase dependent linear terms reveals phenomena similar to those seen when an external signal is injected into a single-mode oscillator. One practical consequence of this work is that two-mode oscillators may well produce single frequency output, since the modes are generally phase locked.

This work examines the coupling of two modes through amplitudes and phases and makes specific application to the closed cavity gyrotron oscillator. The rate equations for the electromagnetic modes are given in Section II and the linear cross-coupling coefficients are calculated for the gyrotron. The rate equations are analyzed in the linear regime in Section III in order to quantitatively describe the phase locking phenomenon. Typical parameters are given for the gyrotron. In Section IV, the effect of the nonlinear rate equation terms is outlined with emphasis on phase locking.

5

II. GYROTRON RATE EQUATIONS

Here we focus on the simplest case of phase-amplitude mode interaction, that of two modes with an arbitrary frequency separation. A restriction will be made to only odd powers of the field amplitude in the electronic susceptibility. Microwave devices, such as the gyrotron oscillator, utilizing a phase mixed electron beam demonstrate this property.

A. Temporal Evolution of Electromagnetic Modes

A set of equations for the evolution of the jth electromagnetic mode can be written [7]

$$\left[\frac{d^2}{dt^2} + c^2 k_j^2\right] \tilde{a}_j(t) + \omega_j \sum_{j'} L_{jj'} \frac{d}{dt} \tilde{a}_{j'}(t) = -\mu_o c^2 \frac{d}{dt} \int_V d^3r \, \tilde{J}_{osc} \cdot e_j^* \tag{1}$$

where the complex modal amplitudes, electron beam current contributions and cavity quality factors are

$$\tilde{a}_j(t) = \frac{1}{2} A_j(t) \, e^{i[\psi_j(t) + \omega_j t]} \quad , \quad \int_V d^3r \, \tilde{J}_{osc} \cdot e_j^* = \frac{1}{2} J_j(t) \, e^{i[\psi_j(t) + \omega_j t]} \quad , \tag{2}$$

$$\text{and} \quad L_{jj'} = \frac{(1+i) k_j}{k_{j'} Q_o^{jj'}} + \frac{1}{Q_e^{jj'}}$$

respectively. Here $A_j(t)$ and $y_j(t)$ are the slowly varying amplitude and phase of the cavity electric field and $J_j(t)$ is the slowly varying component of the electron beam current. The beam current can be related to the cavity fields by the electron equations of motion

$$J_j(t) = \frac{i \, 4 \, \varepsilon_o}{A_j} \left\{ \sum_\sigma \tilde{a}_\sigma \tilde{a}_j^* \, \alpha_{j\sigma} + 4 |\tilde{a}_j|^4 \, \beta_j + \dots \right\} \tag{3}$$

where $\alpha_{j\sigma}$ are the linear growth and cross coupling coefficients and β_j is the coefficient of self-saturation. Higher order saturation and phase interaction through the nonlinear terms is neglected in this analysis. Using (2) and (3) in (1), equations for the modal evolution are found

6

$$\left[\frac{d^2}{dt^2} + c^2 k_j^2\right]\tilde{a}_j + \omega_j \sum_{j'} \left[\frac{(1+i) k_j}{k_{j'} Q_o^{jj'}} + \frac{1}{Q_e^{jj'}}\right]\frac{d}{dt}\tilde{a}_{j'} + 2 i\left(\alpha_j + 4 \beta_j |\tilde{a}_j|^2\right)\frac{d}{dt}\tilde{a}_j = -i \sum_{\sigma \neq j} \alpha_{j\sigma}\frac{d}{dt}\tilde{a}_\sigma$$

(4)

where α_j is the linear growth rate of the jth mode.

The modal rate equations are obtained from (4) by using the method of slowly varying amplitude and phase [4], [7], [8]. These equations are

$$\frac{1}{\omega_j}\dot{P}_j = P_j\left(\alpha_j'' - \sigma_{jj}\right) + (P_j P_k)^{\frac{1}{2}}\left[-(-1)^j\left(\alpha_{jk}' + \sigma_{jk}'\right)\sin \Phi + \left(\alpha_{jk}'' - \sigma_{jk}''\right)\cos \Phi\right] + \beta_j'' P_j^2$$

(5)

$$2\dot{\Phi} = \omega_1 \rho_0 + \omega_1 \alpha_1' - \omega_2 \alpha_2' + \omega_1\left(P_2/P_1\right)^{\frac{1}{2}}\left[\left(\rho_{12} + \alpha_{12}'\right)\cos \Phi + \left(\sigma_{12}'' - \alpha_{12}''\right)\sin \Phi\right] +$$

$$\omega_2\left(P_1/P_2\right)^{\frac{1}{2}}\left[\left(\sigma_{21}'' - \alpha_{21}''\right)\sin \Phi - \left(\rho_{21} + \alpha_{21}'\right)\cos \Phi\right] \quad .$$

Here the over dot indicates differentiation with respect to time. The second order (in power) cross-coupling has been neglected as well as frequency pulling or pushing due to the second order interaction. In (5) P_j is the power in the jth mode (proportional to A_j^2) and primes used on the complex coefficients indicate the real and imaginary parts: $x = x_r' + i x_i''$. The actual frequency of oscillation of mode j is ω_j and $\Phi = \psi_2 - \psi_1 + (\omega_2 - \omega_1) t$. The cavity effects are taken into account through:

$$\rho_o = \frac{1}{\omega_1}\left[2\left(\omega_2^o - \omega_1^o\right) + \left(\frac{\omega_1}{Q_o^{11}} - \frac{\omega_2}{Q_o^{22}}\right)\right] \quad , \qquad \rho_{2i} = \frac{\omega_1}{\omega_2 Q_o^{21}} \quad , \qquad \rho_{21} = \frac{\omega_2}{\omega_1 Q_o^{12}} \quad ,$$

$$\sigma_{jj} = \frac{1}{Q_o^{jj}} + \frac{1}{Q_e^{jj}} \quad \text{and} \qquad \sigma_{jk} = \frac{\omega_k}{\omega_j}\left[\frac{k_j(1 + i)}{k_k Q_o^{jk}} + \frac{1}{Q_e^{jk}}\right] \qquad j \neq k \quad .$$

Here ω^o is the cold (beam-free) cavity resonant frequency and Q_o^{jk} and Q_e^{jk} indicate the quality factors due to Ohmic losses and external losses, respectively. The superscripts indicate that these losses can be a source of mode coupling (these factors can be derived using the formalism of Slater [9]).

7

In order to make these equations as mathematically tractable as possible, we assume that the cross-coupling due to the cavity walls and external load is small. Thus Q_o^{jk} and $Q_e^{jk} >> Q_o^{jj}$ and Q_e^{jj}. This allows the coefficients ρ_{jk} and σ_{jk} to be neglected in (5).

Because of the neglect of terms which are higher powers of P_j in these rate equations it is clear that this representation will have validity only in the small signal regime. Thus the phenomena described here will have applicability to the growth stage of high power oscillators. However, in a nonlinear oscillator, the final steady state is intimately dependent on the characteristics of oscillation growth. Thus it is expected that many of the features found here will persist into the steady state.

B. Coefficients of the Rate Equation Expansion

In order to calculate the electron beam dependent coefficients of the rate equations, an averaging is done over the electron motion through the oscillator cavity. The beam contribution to the jth mode is obtained from the electronic susceptibility of that mode (as defined in [7]) which is

$$\chi_j = -\frac{i\,J_j}{\omega_j\,\varepsilon_o\,A_j} \qquad .$$

In the case of a closed cavity gyrotron with a circular cross-section, the susceptibility can be written in terms of the electron momentum as [10]:

$$\chi_j = -\frac{i\,R_j\,e^{i\psi_j}}{\omega_j^o\,\varepsilon_o\,A_j}\int_{z=0}^{L} f_{q_j}^*(z)\left\langle p_\perp e^{-i\Lambda_j}e^{i(m_j-1)\theta_o}\right\rangle_{\phi_o,\,\theta_o,\,t_o}dz \qquad (6)$$

$$R_j = \frac{1}{\gamma_o}\left(1-\beta_{\perp o}^2\right)\frac{I_o\,C_{m_j\,\ell_j}\,k_{m_j\,\ell_j}\,J_{m_j-1}\left(k_{m_j\,\ell_j}\,R_0\right)}{2\,m_e\,v_{z_0}}$$

where m_j, ℓ_j, and q_j are the azimuthal, radial, and axial mode indices for mode j, f_q is the axial electric field profile (the asterisk indicates complex conjugate and z is the axial coordinate), L is the cavity length, and $p_\perp$ and Λ are the slowly varying components of the electron perpendicular momentum familiar from gyrotron theory [11]. The electron mass is m_e, initial electron velocity perpendicular and parallel to the axial direction are $v_{\perp 0}$ and v_{z0} ($\beta_{\perp 0} = v_{\perp 0}/c$). I_o is the dc beam current, R_0 is the guiding center position, and the perpendicular wavenumber is $k_{m\ell}$. $C_{m\ell}$ is a normalization constant which is given in

8

[11]. The brackets indicate an average over initial conditions of the electron beam: ϕ_0 is the phase angle on the electron gyro-orbit, θ_0 is the guiding center phase angle, and t_0 is the entrance time of the electron into the cavity. From the electron equations of motion the momentum can be expanded in powers of the electric field amplitude:

$$p_\perp e^{-i\Lambda_j} = p_{\perp_0} e^{-i\Delta_j z} e^{-i(\omega_j t_o - \phi_o)} \left[1 + \sum_{n=1}^{\infty} \sum_{p=0}^{\infty} a_{np}(z) x^p \left(x^*\right)^{n-p} \right]$$

where the a_{np} are z dependent expansion coefficients and

$$x = e^{-i\Lambda_j} e^{i\Delta_j z} e^{i(\omega_j t_o - \phi_o)} \sum_{j'} A_{j'} e^{i\psi_{j'}} f_{q_{j'}}(z) e^{i\Lambda_{j'}} e^{-i(m_{j'} - 1)\theta_o}$$

$$= e^{-i\Lambda_j} e^{i\Delta_j z} e^{i(\omega_j t_o - \phi_o)} \sum_{j'} y_{j'} e^{i\Lambda_{j'}} \qquad .$$

For two modes the averaged momentum expansion can be written:

$$\left\langle p_\perp e^{-i\Lambda_j} \right\rangle_{\phi_o, t_o} = p_{\perp_0} e^{-i\Lambda_j} \sum_{s=1}^{2} e^{i\Lambda_s} y_s(z) \sum_{n=0}^{\infty} b_{nj}(z) \left| \sum_{k=1}^{2} y_k(z) e^{i\Lambda_k} \right|^{2n} \qquad (7)$$

where the b_{nj} are expansion coefficients. Keeping only the n = 0 and 1 terms in (7), (this includes the third order terms in the momentum expansion), averaging over guiding center angle, and substituting into (6), the following expression is obtained for the susceptibility

$$\chi_j = \alpha_j + \alpha_{jk} \frac{A_k}{A_j} e^{-i(-1)^j \Phi} + \beta_j A_j^2$$

where the definitions for the (complex) linear growth, linear coupling and self-saturation terms are

$$\alpha_j = h_j \, C_{m_j} \, 4_j \int_{x=0}^{L} \left| f_{q_j}(z) \right|^2 b_{0_j}(z) \, dz \quad , \quad \alpha_{jk} = h_j \, C_{m_k} \, 4_k \, \delta_{m_j, m_k} \int_{x=0}^{L} f_{q_j}^*(z) \, f_{q_k}(z) \, b_{0_j}(z) \, dz$$

(8)

$$\text{and} \qquad \beta_j = h_j \, C_{m_j}^3 \, 4_j \int_{x=0}^{L} \left| f_{q_j}(z) \right|^4 b_{1_j}(z) \, dz \quad .$$

Here $h_j = i \, R_j \, p_{\perp_0} / (\varepsilon_0 \, \omega_j)$. The coefficients α_j and β_j have been given elsewhere [4, 7]. The coefficients α_{jk} are found by using

$$b_{0_j}(z) = \frac{e^{-i \Delta_j z}}{f_q} \left\{ \int_0^z f_q \, e^{i \Delta_j z'} \, dz' - i \int_0^z \int_0^{z'} f_q \, e^{i \Delta_j z''} \, dz'' \right\}$$

in (8). Note that there is no phase coupling through the linear terms if the modes have different azimuthal indices m_j. Numerical examples of α_{jk}, calculated for TE_{111} and TE_{112} modes in a circular cylindrical gyrotron cavity are shown in Figs. 1 and 2. The electron beam parameters are 20 kV, 1 A, perpendicular-to-parallel velocity ratio of 1.4, and $R_0 = .9$ cm. The cavity parameters are L = 60 cm, wall radius of 1.79 cm and quality factor of 120. Figure 1 shows the real and imaginary parts of the TE_{111} linear growth rate α_1 and linear cross-coupling α_{12}. The coefficients are shown as a function of normalized detuning of the wave frequency from the cyclotron frequency, $\Delta_{c_j} = \frac{2}{\omega_0 \, \beta_{\perp_0}} (\omega_j - \Omega)$. Here Ω is the electron cyclotron frequency and ω_0 is a normalization frequency ($\omega_0 / 2\pi = 5.0$ GHz in the example shown). It can be seen in Fig. 1 that the cross-coupling coefficients are generally an order of magnitude smaller than the linear growth rates. That the cross-coupling acts to oppose the linear growth can be seen from Fig. 1 where the α_{12} (both real and imaginary parts) are 180° out of phase with α_1. The TE_{112} results show similar features with respect to phase and relative size. A comparison of Fig. 2(a) with Fig. 1(a) shows that $\alpha_{21} = -\alpha_{12}$. This relationship holds between any modes with adjacent axial mode indices. It can further be shown, for modes spaced more than one index apart:

$$\omega_k \, \alpha_{kj} = \omega_j \, \alpha_{jk} \quad \text{if } j \text{ and } k \text{ are both even or both odd,}$$

$$\omega_k \, \alpha_{kj} = -\omega_j \, \alpha_{jk} \quad \text{if either } j \text{ or } k \text{ (but not both) is odd.}$$

(9)

These symmetry relations only hold when $\Delta_{c\,j} = \Delta_{c\,k}$. For most values of the magnetic field, the cyclotron detuning of the two modes is not the same. The cross-coupling coefficients are given as a function of magnetic field in Fig. 3 for the TE_{111} and TE_{112} modes. It can be seen that there is a slight offset between each set of curves. Hence, when solving (5) for a typical set of gyrotron parameters, the coupling coefficients will not obey (9).

Figure 4 shows the coupling coefficient between TE_{111} and the TE_{113} and TE_{114} modes. The result here is similar to that of coupling with the TE_{112} mode, except that the strength is somewhat weaker and the coupling coefficient changes sign more rapidly with a change in Δ. The degree of coupling of the TE_{111} with higher order modes is shown in Fig. 5. The coupling strength falls off as q^{-1}, where q is the axial mode index. The effect of higher order modes on the TE_{111} is expected to be small since the frequency spacing between modes increases with q. Hence these modes make a small, rapidly varying contribution to the power of the TE_{111}.

Equations (5) are first studied in the case where the $\beta_j = 0$. In this case the mode coupling occurs only through the terms which are first order in the power. It will be seen that the overwhelming tendency is for the modes to phase lock (that is reach a situation where $d\Phi/dt = 0$). Since only two modes are considered here, we note that $d\Phi/dt = 0$ implies that the two modes have the same final frequency, thus they are also frequency locked (or synchronized). This phase locking occurs whether or not the powers P_j reach a saturated level. Application is made to the TE_{111} - TE_{112} competition in the closed cavity gyrotron.

III. SMALL SIGNAL ANALYSIS

One interesting feature of this problem is the fact that coupling can occur between the modes due to terms directly proportional to the mode power. These terms can thus cause a "linear" mode interaction of the same size as the linear growth rate. Since most oscillations start from a small noise level, thus spending a fair amount of time in the linear regime, it is of interest to examine the linear mode coupling predictions.

A. Solution of the Linearized Rate Equations

Equations (5), with $\beta_j = 0$ and in normalized form, become

11

$$\frac{d\overline{P}_1}{d\tau} = \overline{P}_1 + \left(\overline{P}_1\,\overline{P}_2\right)^{\frac{1}{2}}\left(C_1\,\sin\Phi + C_2\,\cos\Phi\right) \qquad\text{(a)}$$

$$\frac{d\overline{P}_2}{d\tau} = \Gamma\,\overline{P}_2 + \left(\overline{P}_1\,\overline{P}_2\right)^{\frac{1}{2}}\left(C_1\,\sin\Phi - C_2\,\cos\Phi\right) \qquad\text{(b)} \qquad\text{(10)}$$

$$\frac{d\Phi}{d\tau} = \Delta + \frac{1}{2}\left(\overline{P}_2/\overline{P}_1\right)^{\frac{1}{2}}\left(C_1\,\cos\Phi - C_2\,\sin\Phi\right) + \frac{1}{2}\left(\overline{P}_1/\overline{P}_2\right)^{\frac{1}{2}}\left(C_1\,\cos\Phi + C_2\,\sin\Phi\right) \qquad\text{(c)}$$

where $\tau = \Gamma_1\, t$, $\Delta = \omega_1\,(\rho_0 + \alpha_{11}' - \alpha_{22}'\,\omega_2/\omega_1)/(2\,\Gamma_1)$, $\overline{P} = P/\Gamma_1$, $\Gamma = \Gamma_2/\Gamma_1$, and $C_1 = \alpha_r /\Gamma_1$, $C_2 = \alpha_i /\Gamma_1$ where $\Gamma_j = \omega_j\,(\alpha_{j}'' - \sigma_j)$ and $\omega_1\,\alpha_{12} = \alpha_r + i\,\alpha_i$. It is assumed that the cross-coupling coefficients have the symmetry of the $TE_{111} - TE_{112}$ gyrotron modes given in (9). The variation in α_{jk} due to the unequal cyclotron detunings of the two modes is neglected (this correction can be included at the cost of complicating the following analysis). Δ is the difference between the free-running beam and cavity loaded resonant frequencies of the two modes (normalized to the growth rate of mode 1).

It is to be noted that when $\beta_j = 0$, (4) represent a linear system of equations which can be solved exactly. For two modes, the solutions are of the form

$$\tilde{a}_j\,(t) = \sum_{k=1}^{4} p_{kj}\, e^{\lambda_k t} \qquad\text{(11)}$$

where the coefficients p_{kj} are found from the initial conditions and the λ_k are the eigenvalues. The eigenvalues are found from a fourth order characteristic equation (with complex coefficients), which can be derived from (4) using standard techniques. Instead of solving the characteristic equation exactly, we focus on some qualitative features of the solutions. In particular, from (11) it is clear that the ratio of power levels in the two modes generally approaches p_{n1}/p_{n2}, where λ_n is the eigenvalue with the largest real part. If $\mathrm{Re}\{\lambda_n\} < 0$ then the power in both modes approaches zero (mode suppression), and if $\mathrm{Re}\{\lambda_n\} = 0$ and $\mathrm{Im}\{\lambda_n\} \neq 0$ then the modal power levels oscillate in time.

Equation (10c) yields a phase locking bandwidth if the power level ratio of the two modes is fixed. This stationary phase result ($d\Phi/d\tau = 0$) is possible when the following criterion is met

$$\left| \frac{2\,\Delta}{\sqrt{\left(\overline{P}_2/\overline{P}_1 + \overline{P}_1/\overline{P}_2\right)\left(C_1{}^2 + C_2{}^2\right) + 2\left(C_1{}^2 - C_2{}^2\right)}} \right| < 1 \; . \qquad\text{(12)}$$

In the case where the cavity and load cross-coupling have not been neglected, the locking criterion is:

12

$$\left| \frac{2\Delta}{\sqrt{a^2 + b^2}} \right| < 1$$

where
$$a = \left(\overline{P}_2 \big/ \overline{P}_1 \right)^{\frac{1}{2}} \left(\rho_{12} + \dot{\alpha}_{12} \right) - \left(\overline{P}_1 \big/ \overline{P}_2 \right)^{\frac{1}{2}} \left(\rho_{21} + \dot{\alpha}_{21} \right)$$

and
$$b = \left(\overline{P}_2 \big/ \overline{P}_1 \right)^{\frac{1}{2}} \left(\sigma''_{12} - \alpha''_{12} \right) + \left(\overline{P}_1 \big/ \overline{P}_2 \right)^{\frac{1}{2}} \left(\sigma''_{21} - \alpha''_{21} \right) \quad .$$

This criterion is an extended version of that obtained in single mode injection locked oscillators [12]. This equation differs from that of [12] in that the two power levels can be of comparable size and beam coupling effects (as well as coupling through the external load) are included in the coefficients a and b. Equations (11) and (12) indicate that the two modes will generally phase lock together through the linear interaction. To evaluate the locking bandwidth, one requires knowledge of the steady state modal power ratio. This information must come from a solution of (10).

To examine the phase locking phenomenon it is convenient to make the transformation $(\overline{P}_1 , \overline{P}_2)$ $\rightarrow (x, y)$ where $x = (\overline{P}_1 / \overline{P}_2)^{1/2}$ and $y = (\overline{P}_1 \overline{P}_2)^{1/2}$. Equations (10) result in

$$\frac{dx}{d\tau} = \frac{x}{2} \left[1 - \Gamma + \left(\frac{1}{x} - x \right) C_1 \sin \Phi + \left(\frac{1}{x} + x \right) C_2 \cos \Phi \right] \tag{a}$$

$$\frac{dy}{d\tau} = \frac{y}{2} \left[1 + \Gamma + \left(\frac{1}{x} - x \right) C_2 \cos \Phi + \left(\frac{1}{x} + x \right) C_1 \sin \Phi \right] \tag{b}$$

$$\tag{13}$$

$$\frac{d\Phi}{d\tau} = \Delta - \frac{1}{2} \left(\frac{1}{x} - x \right) C_2 \sin \Phi + \frac{1}{2} \left(\frac{1}{x} + x \right) C_1 \cos \Phi \quad . \tag{c}$$

The advantage of this transformation is that a decoupling is achieved between y and the other two variables. Thus the variable y has no effect on the dynamics of x and Φ. In addition the instabilities, inherent in a system with no high order saturation, are confined to the variable y. The phase locking predictions of this system of equations will now be discussed.

B. Linear Phase Locking

13

The two-mode system reaches a phase locked equilibrium when both $\dfrac{dx}{d\tau}$ and $\dfrac{d\Phi}{d\tau}$ are zero. From (13a) and (13c) this happens for an angle Φ^0

$$\sin \Phi^0 = \frac{C_1\left(\Gamma - 1\right) + 2 \Delta C_2}{\left(\frac{1}{x^0} - x^0\right)\left(C_1{}^2 + C_2{}^2\right)} \quad , \qquad \cos \Phi^0 = \frac{C_2\left(\Gamma - 1\right) - 2 \Delta C_1}{\left(\frac{1}{x^0} + x^0\right)\left(C_1{}^2 + C_2{}^2\right)} \tag{14}$$

where x^0 is a real (positive) solution to the *real* quartic equation

$$p^4 - a_0 p^3 + a_1 p^2 - a_0 p + 1 = 0 \quad \text{where } p = \left(x^0\right)^2 \text{ and} \tag{15}$$

$$a_0 = \frac{1}{\left(C_1{}^2 + C_2{}^2\right)^2}\left\{\left[C_1\left(\Gamma - 1\right) + 2 \Delta C_2\right]^2 + \left[C_2\left(\Gamma - 1\right) - 2 \Delta C_1\right]^2\right\} \quad ,$$

$$a_1 = \frac{2}{\left(C_1{}^2 + C_2{}^2\right)^2}\left\{\left[C_2\left(\Gamma - 1\right) - 2 \Delta C_1\right]^2 - \left[C_1\left(\Gamma - 1\right) + 2 \Delta C_1\right]^2\right\} - 2 \quad .$$

The stability of these equilibria can be found by a perturbation analysis of (13a) and (13c). It is found that the growth (or decay) rate of perturbations is given by

$$\Gamma_p = \frac{\left(1 - \Gamma\right)}{2} + x^0\left[C_2 \cos \Phi^0 - C_1 \sin \Phi^0\right] \quad . \tag{16}$$

Stable equilibria ($\Gamma_p < 0$) correspond to phase locked solutions of (10). Note that this locking takes place in the absence of any nonlinearity. It is of interest to determine the time required for the modes to achieve the phase locked state. An estimate of this lock-in time can be made from (16). The real part of the eigenvalue resulting from the perturbation analysis gives the rate of approach to the phase locked equilibrium point (in the immediate vicinity of that point). However this rate is found to be quite accurate even at points far from equilibrium. The lock-in time τ_{LOCK} is defined as the time required for the oscillator to decrease its distance from the equilibrium point in the $x - \Phi$ plane by a factor of $e = 2.718$ and, according to (16) is:

$$\tau_{LOCK} = \frac{1}{-\Gamma_p}$$

(17)

If the phase plane distance is measured as

$$\varepsilon = \left\{ \frac{\left(\Phi - \Phi^o\right)^2}{\left(\Phi^o\right)^2} + \frac{\left(x - x^o\right)^2}{\left(x^o\right)^2} \right\}^{\frac{1}{2}}$$

then a comparison can be made between the predicted rate of approach to equilibrium and that found numerically from (10). This comparison is shown in Fig. (6) for parameters corresponding to gyrotron operation at a magnetic field of 1.838 kG ($\Gamma_1 = 0.756$, $\Gamma = 1.8$, $C_1 = 0.0574$, $C_2 = -0.0249$, $\Delta = -0.978$). The lock-in time in this case is 3.29 ns, which is ~ 16 radiation periods. It can be seen that the value of τ_{LOCK} from (17) provides an excellent approximation to the actual lock-in time. The actual approach to the phase locked state involves a slight oscillation which is not found from the approximate method. Thus the time required to reach the phase locked state can be accurately predicted even though the modal power levels are far from stationary. This is an important result since high power oscillators are operated in the short pulse regime (the power changes rapidly in time) and the time available for the locking process is restricted.

Phase locking properties are calculated for gyrotron operation when the TE_{111} mode is linearly unstable. This unstable region (Fig. 7) is between 1.83 and 1.86 kG, using the operating parameters of Fig. 1. It can be seen that the TE_{112} mode is linearly unstable at low magnetic field and is not normally excited above 1.845 kG (in the region $\alpha_1'' > 0$). The stationary amplitude ratio and phase locking angles are shown in Fig. 8 for the gyrotron through this magnetic field range. This figure shows that there is a discontinuity in the stationary equilibrium (x^0, Φ^0) at 1.841 kG. At this value of the magnetic field $\Gamma = 1$ and a periodic solution results (infinite lock-in time). The values of x^0 on either side of the discontinuity are approximately reciprocals of one another. Above 1.841 kG the TE_{112} mode is excited (though it has a negative growth rate) by energy influx from the TE_{111} mode. For lower magnetic fields, the TE_{112} mode dominates, and linearly suppresses the TE_{111} mode (the amplitude ratio in this region is about x^0 = .03).

It is of interest to find the dependence of τ_{LOCK} on the parameters Δ, Γ, C_1 and C_2. This information is given in Fig. 9. Here the parameters are varied about the gyrotron coefficients given in

15

connection with Fig. 6. In Fig. 9, the four curves show the result of varying one parameter at a time. The detuning is varied in Fig. 9(a). Unlike the injection locked oscillator, the minimum locking time is slightly offset from $\Delta = 0$, and the modes do not break out of the phase locked condition at large detuning. Instead, τ_{LOCK} asymptotes to $\tau_{\infty} = 2/(\Gamma-1)$. This is due to the dependence of the steady-state amplitude ratio on Δ. Since $1/(x^0)^2 + (x^0)^2$ continually increases with Δ, the locking limits given by (12) are never met (for $\Gamma \neq 1$). The results in Figs. 9(a) and 9(c) thus show lock-in times relative to τ_{∞}. These results will not be accurate when Δ becomes very large with Γ, C_1 and C_2 fixed. This is because, from (12), in order to have a phase locked solution with large Δ either $x^0 >> 1$ or $x^0 << 1$. In either case, the power in one of the modes is very large, thus violating the linear assumption made in (10). The asymmetry of the locking results in Fig. 9(a) is due to the presence of both $\sin\Phi$ and $\cos\Phi$ components in (13c). This equation does not have even parity in Δ, and (13a) and (13b) do not have even parity in Φ.

From (14), (15), and (16) it can be shown that τ_{LOCK} depends on Γ in the form $(\Gamma-1)$, thus, the relevant physical quantity involving growth rate is the difference in growth rates of the two modes. Figure 9(b) shows that for small cross-coupling, the lock-in time depends on $|\Gamma - 1|$. The time required for phase locking becomes very large at $\Gamma = 1$ since τ_{∞} becomes infinite at that point. When $\Gamma = 1$, the lock-in time becomes

$$\tau_{LOCK} = \frac{(C_1{}^2 + C_2{}^2)\left[1 - (x^0)^4\right]}{4\,\Delta\,C_1\,C_2\,(x^0)^2} \quad . \tag{18}$$

It is found that when $\Delta\,C_1\,C_2 > 0$ then $x^0 < 1$, and when $\Delta\,C_1\,C_2 < 0$, then $x^0 > 1$. In this way, τ_{LOCK} is always positive. However, when $\Delta\,C_1\,C_2 = 0$, then a periodic solution may be obtained. This solution, depending on the initial conditions, may be either bounded or unbounded in Φ. The former corresponds to periodic mode pulling, while the latter is mode beating. Another possibility, when $\Delta\,C_1$ $C_2 = 0$, is that $x^0 = 1$, thus yielding a finite ratio in (18) and a phase locked solution.

Generally, the more disparate the growth rates, then the shorter the lock-in time. This result is interpreted as a domination of the mode interaction by the more rapidly growing mode, hence causing more rapid phase locking.

The dependence of τ_{LOCK} on C_1 and C_2 is shown in Fig. 9(c). The figure shows that an increase in the size of the cross-coupling coefficient $|C_1|$ causes the modes to phase lock more rapidly. The opposite is true for $|C_2|$. Thus, the larger $|Re\{\alpha_{12}\}|$ and the smaller $|Im\{\alpha_{12}\}|$ the more rapidly will phase locking be obtained.

IV. NONLINEAR SATURATION ($\beta \neq 0$)

16

The inclusion of self- saturation effects in (13) causes a considerable analytic complication. When $\beta \neq 0$ the dependent variable y appears in (13a) thus modifying the $x - \Phi$ dynamics. Thus the problem is fully three dimensional and the phase space is more difficult to visualize than in the linear case. A general overview is given of the numerical results and application is made to the $TE_{111} - TE_{112}$ competition in the gyrotron. Only the case $\beta_1, \beta_2 < 0$ is considered since it is that case which provides a stable steady state for the two modes.

It is found numerically that, even with very small self-saturation coefficients β, the phase locking between modes can be broken by an increase in the detuning when $\Gamma > 0$. This is so because β prevents either modal power from becoming extremely large, and the linear growth rates and cross-coupling prevent the powers from becoming extremely small. Thus the allowable range of x^o values is restricted. From (12), it is seen that the phase locking frequency band depends on $1/(x^o)^2 + (x^o)^2$. Because of the restriction on x^o, the denominator of (12) cannot increase without limit to balance a large numerator (as in the linear case). It is found that the steady state values x^o and Φ^o depend of the ratio β_1/β_2 and are thus virtually independent of β in the case $\beta_1 = \beta_2$. The actual values of the steady state modal power levels are sensitive to the value of β, however this information is confined to the variable y.

When $\beta \neq 0$ and $\Gamma > 0$ a progression of three oscillator behaviors is seen as Δ is increased through the locking limits. When Δ is small the oscillator is locked. Periodic pulling occurs just beyond the locking band (here the relative phase between the modes oscillates in time). Finally, for larger Δ, mode beating occurs with a continual increase in relative phase.

When $\Gamma < 0$, the locking band can become very large since x^0 becomes large due to the subservient nature of mode 2. As the detuning is increased (at a fixed value of Γ), the amplitude of the damped mode decreases, and remains phase locked to the growing mode. This is understandable since the damped mode has no source of excitation but the one driving it. Hence the two modes have related phases. In this case the predictions of the linear theory are relevant.

The linear theory adequately predicts the values of x and Φ in the locked state for parameters well within the phase locking band. A comparison between the predictions of x^o and Φ^o with and without self-saturation is shown in Fig. 10. This figure again is based on gyrotron parameters chosen in the region where the TE_{111} mode has positive growth. The linear results are reproduced from Fig. 8 for convenience. The self-saturation coefficients are chosen to both equal $- 1.0 \times 10^{-4}$. As indicated previously, these locking results are not sensitive to the precise value of β. The shading in the figure shows the region of unlocked oscillator operation. In the gyrotron case considered, the values of the linear cross-coupling coefficients are so small that the modes unlock almost as soon as $\Gamma > 0$ (this happens at a magnetic field of 1.847 kG). It is clear that the predictions of linear theory are inadequate in this region of parameter space. However, for $\Gamma < 0$, the linear theory is adequate. Both the predictions of

17

amplitude ratio and locked phase become more accurate at high magnetic field strengths (larger values of $|\Gamma|$).

An example of the temporal evolution of the amplitude ratio and relative phase is given in Fig. 11. The parameters in this case correspond to gyrotron operation at 1.853 kG ($\Gamma_1 = 1.49$, $\Gamma = -1.32$, $C_1 = -0.0213$, $C_2 = -0.0532$, $\Delta = -0.188$); a magnetic field for which Fig. 10 indicates that the linear prediction of the steady state is not a good one. The β's are chosen to be -1.0×10^{-5}. An interesting feature of this figure is that there are two plateaus in both the x and Φ curves. One corresponds to the true nonlinear phase locked state (for $\tau > 25$), while the other ($5 < \tau < 15$) is a "metastable" equilibrium which is due to the linear locking (and occurs at the values of x^0 and Φ^0 given by the linear theory in Fig 10). In this instance the self-saturation is small enough that the modes achieve the linear locked state but are disrupted as the modal powers increase to such a point that the self-saturation becomes important. The linear locking result has validity if the oscillator pulse terminates before the metastable equilibrium is destabilized. In this case, the upper limit on pulse length is about 20 e-folding times for the TE_{111} mode or 13.5 ns.

When $\Gamma > 0$, the locking bandwidth generally increases with an increase in $|\Gamma - 1|$. This result is shown in Fig. 12 for the parameter set ($C_1 = 0.8$, $C_2 = 0.5$, $\beta_1 = \beta_2 = -0.001$). The gyrotron example does not clearly exhibit this effect since the C's are so small that the locking band becomes extremely small for $\Gamma > 0$ and is difficult to compute. The shading in the figure indicates the region over which the two modes are phase locked. The locking band is asymmetric about $\Delta = 0$ for the same reasons given in the linear case, Fig. 9(a). The numerically computed locking limits can be checked by a comparison with (12), using the associated values of x^0. Good agreement is found.

Minima in the locking band edges are seen in Fig. 12 at $\Gamma = 0$ ($\Delta > 0$) and $\Gamma = 2$ ($\Delta < 0$). These minima occur when x^0 reaches such a value that the denominator in (12) is minimized. In such a case the detuning can be varied over only a small range before the inequality in (12) is violated. It can easily be shown that x^0 should equal one for a minimum to occur. At this amplitude ratio, (12) indicates that $|\Delta/C_1| = 1$, at the locking limit. It is interesting that only the coefficient C_1 plays a role here. Equation (13c) reveals that at a minimum of the locking edge: $\cos\Phi^0 = -\Delta/C_1$. Using this, it is found that a phase locked equilibrium of (10), (with β's included), satisfies:

$$\overline{P}_{MIN} = \frac{\Gamma - 1 \pm 2\,C_2}{\beta_1 - \beta_2} \, , \qquad \beta_1 \neq \beta_2 \quad .$$

(19)

at the locking edge minimum. Here $\overline{P}_{MIN}$ is the normalized power in each mode. The two different signs correspond to the locking edge with $\Delta > 0$ (plus sign) or $\Delta < 0$ (minus sign). When the self-

18

saturation coefficients are equal, then a condition is obtained for Γ at which the locking minimum will occur:

$$\Gamma_{MIN} = -\left(-1 \pm 2\,C_2\right), \qquad \beta_1 = \beta_2 \quad .$$

(20)

The two signs have the same meaning as in (19). Note that both (19) and (20) depend only on the coefficient C_2. Equation (20) accurately predicts the minima in Fig. 12 with $C_2 = 0.5$. The points at which it is most difficult to phase lock (these minima) occur very near $\Gamma = 1$, when the cross coupling is small. This is just the point at which linear theory predicts an infinite lock-in time.

From the previous analysis, it is expected that the locking width increases with an increase in $|C_1|$. A change in C_1 does not affect the size of the locking minima, but does change the values of Γ for which the minima occur. Hence, for a fixed ratio of growth rates Γ_0, the locking band could either decrease or increase with a change in C_1 depending on whether Γ_{MIN} approaches or departs from Γ_0. An increase in the absolute size of the self-saturation has no effect on the phase locking band in the case $\beta_1 = \beta_2$. This is because x^0 depends on the ratio of β_1 to β_2. Unequal saturation coefficients may cause a substantial change in the locking bandwidth. For example, if $x^0 < 1$, then an increase of β_1 causes mode 1 to saturate more quickly (and at a lower power level) so that x^0 decreases even further. This increases the denominator of (12) allowing a wider locking bandwidth (on the edge where $x^0 < 1$). Since it may not be true that $x^0 < 1$ on both locking edges ($\Delta < 0$ and $\Delta > 0$) the overall locking bandwidth measured at constant Γ may either increase or decrease. An increase of β_2 causes the opposite effect. The same changes in β_1, and β_2 have the opposite effect on the edge of the locking band where $x^0 > 1$.

It can be shown that when the steady state amplitude ratio becomes either very large or very small the locking limits become infinite. When $x^0 >> 1$, (10) yields approximate results for the modal power levels:

$$\overline{P}_1 = -\frac{1}{\beta_1} \quad \text{and} \quad \overline{P}_2 = -\frac{C_1{}^2}{4\,\Delta^2\,\beta_1}$$

and the locking criterion (12) becomes

$$\left| \frac{C_1}{\sqrt{C_1{}^2 + C_2{}^2}} \right| < 1$$

(21)

which is clearly always satisfied. For $x^0 \ll 1$, the power levels are

$$\overline{P}_2 = -\frac{\Gamma}{\beta_2} \quad \text{and} \quad \overline{P}_1 = -\frac{\Gamma C_1^2}{4\Delta^2 \beta_2}$$

which result in the same locking criterion as (21). An example of this phenomenon is shown in Fig. 12 near $\Gamma = 0$. It can be seen that the locking edge for $\Delta < 0$ approaches negative infinity. It is obvious from the figure that the locking edges for positive and negative Δ need not $\rightarrow \infty$ for the same value of Γ. Figure 12 shows an increase in the locking band at large Γ. This is due to a decrease in x^0 with increasing Γ at both edges of the locking band. The same result is obtained for $\Gamma \ll 1$.

V. CONCLUSION

The system of two electromagnetic modes interacting through amplitudes and phases in the first order approximation has been analyzed. Regimes of phase locking, periodic oscillation of power and phase, and mode excitation have been identified. The approximate time for the phase locking process has been found. In the case of small nonzero (negative) self-saturation, it is found that the phase locking bandwidth is limited in size. The ratio of the equilibrium power levels, the lock-in time, and the lock-in phase are fairly well approximated by the linear theory near the center of the locking band. Qualitative features of the phase locking band can be analytically computed and have been numerically verified. Further work is proceeding to further study the case of unequal degrees of modal self-saturation ($\beta_1 \neq \beta_2$).

REFERENCES

[1] D. Price and H. M. Sze, "Phase-stability analysis of the magnetron-driven vircator experiment," IEEE Trans. Plasma Science vol. 18, p. 580 - 585, 1990.

[2] B. Levush and T. M. Antonsen, "Mode competition and control in high-power gyrotron oscillators," IEEE Trans. Plasma Science vol. 18, pp. 260 - 271, 1990.

[3] W. Woo et al., "Phase locking of high-power microwave oscillators," J. Appl. Phys. vol. 65, pp. 861 - 866, 1989.

[4] G. S. Nusinovich, "Mode interaction in gyrotrons," Int. J. Electron. vol. 51, pp. 457- 474, 1981.

[5] A.W. Fliflet, R.C. Lee, S.H. Gold, W.M. Manheimer, and E. Ott, "Time-dependent multimode simulation of gyrotron oscillators," Phys. Rev. A vol. 43, pp. 6166 - 6176, 1991.

[6] A. Bondeson, B. Levush, W.M. Manheimer, and E. Ott, "Multimode theory and simulation of quasioptical gyrotrons and gyroklystrons," Int. J. Electron. vol. 3, pp. 547- 553, 1982.

[7] A. H. McCurdy and C. M. Armstrong, "Mode selection by priming in an overmoded electron cyclotron maser," Phys. Fluids B vol. 3, pp. 212 - 227, 1991.

[8] S. Riyopoulos, "Multimode simulations without particles in the quasi-optical gyrotron," IEEE Trans. Plasma Science vol. 18, pp. 369 - 386, 1990.

[9] J.C. Slater, *Microwave Electronics* . New York: Van Nostrand, 1950.

[10] A. H. McCurdy, A. K. Ganguly, and C. M. Armstrong, "Operation and theory of a driven single-mode electron cyclotron maser," Phys. Rev. A vol. 40, pp. 1402 - 1421, 1989.

[11] A. W. Fliflet, M. E. Read, K. R. Chu, and R. Seeley, "A self-consistent field theory for gyrotron oscillators: application to a low Q gyromonotron," Int. J. Electron. vol. 53, pp. 505 - 521, 1982.

[12] R. Adler, "A study of locking phenomena in oscillators," Proc. IRE vol. 34, 351- 357 (1946).

Figure Captions

1: Real part (dash) and imaginary part (solid) of (a) Linear cross-coupling and (b) linear growth coefficients for TE_{111} mode in competition with TE_{112}. Δ_{c1} is the detuning of the TE_{111} frequency from the cyclotron frequency.

2: Real part (dash) and imaginary part (solid) of (a) Linear cross-coupling and (b) linear growth coefficients for TE_{112} mode in competition with TE_{111}. Δ_{c2} is the detuning of the TE_{112} frequency from the cyclotron frequency.

3: (a) Imaginary and (b) real parts of cross-coupling coefficients of TE_{111} (solid) and TE_{112} (dash) modes as a function of the static magnetic field.

4: Cross-coupling between the TE_{111} mode and (a) TE_{113} and (b) TE_{114} modes. Real (dash) and imaginary (solid) parts are shown.

5: Degree of cross-coupling of TE_{111} with higher order modes.

6: Time required for phase locking to be achieved. Both numerical (solid) and exponential decay (dash) solutions are shown.

7: Imaginary part of linear growth rate of TE_{111} (solid) and TE_{112} (dash) modes as a function of magnetic field.

8: Stable phase locked amplitude ratio and locking angle for gyrotron with positive TE_{111} growth rate.

9: Dependence of time taken to phase lock on (a) mode frequency detuning, (b) relative growth rate, (c) linear cross-coupling.

10: Comparison between linear theory (solid and dash) and nonlinear theory (chaindot and dot) with $\beta_1 = \beta_2 = -.0001$.

11: Case of small self-saturation where a metastable equilibrium is found ($\beta_1 = \beta_2 = -.00001$).

12: Phase locking bandwidth in the nonlinear case as a function of relative growth rate ($\beta_1 = \beta_2 = -.001$).

FIG. 1

FIG. 2

24

(a)

$\mathrm{Im}\{\omega_j^0 \alpha_{jk}\}$

(b)

$\mathrm{Re}\{\omega_j^0 \alpha_{jk}\}$

Magnetic Field (kG)

FIG.3

25

FIG. 4

26

Maximum Value of Re { $\omega_1^0 \alpha_{1q}$ }

AXIAL MODE INDEX, q

FIG. 5

FIG. 6

GROWTH RATE (ns⁻¹)

MAGNETIC FIELD (kG)

FIG.7

FIG.8

FIG.9

31
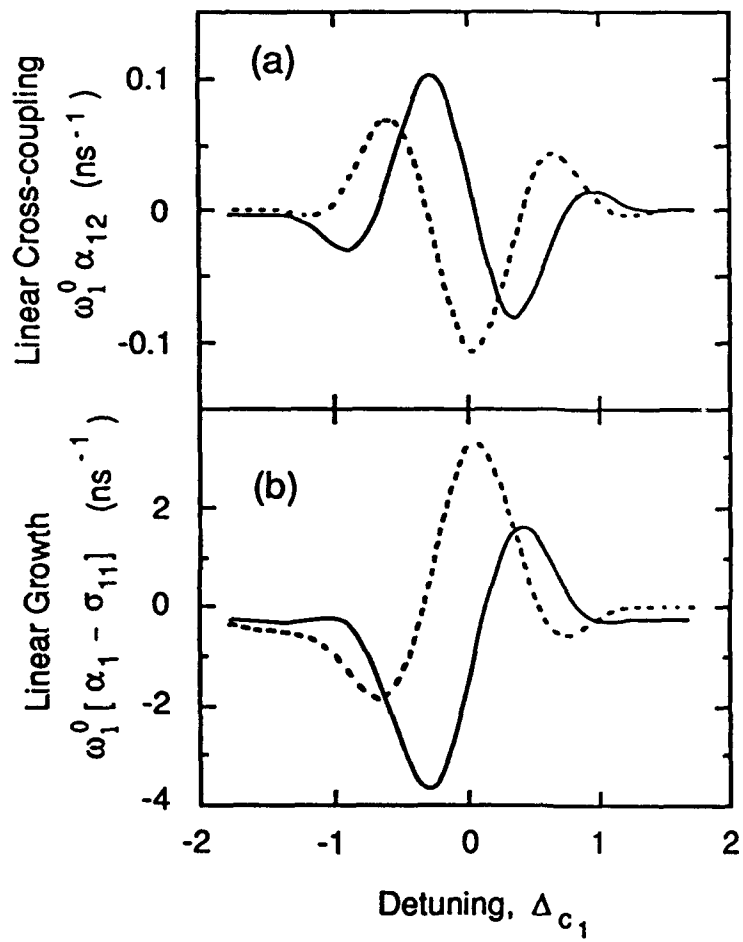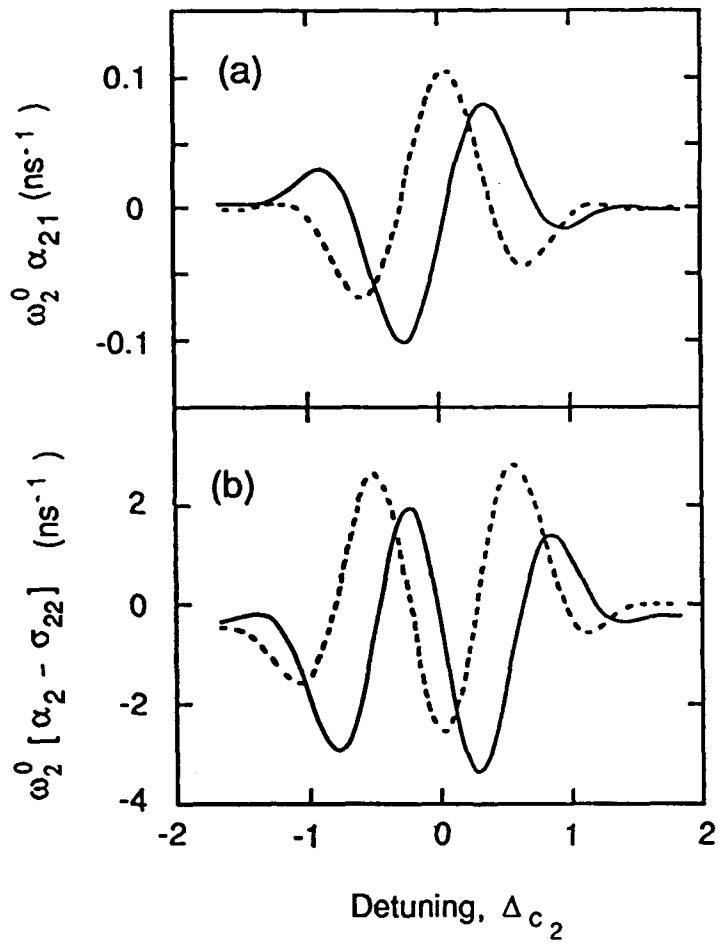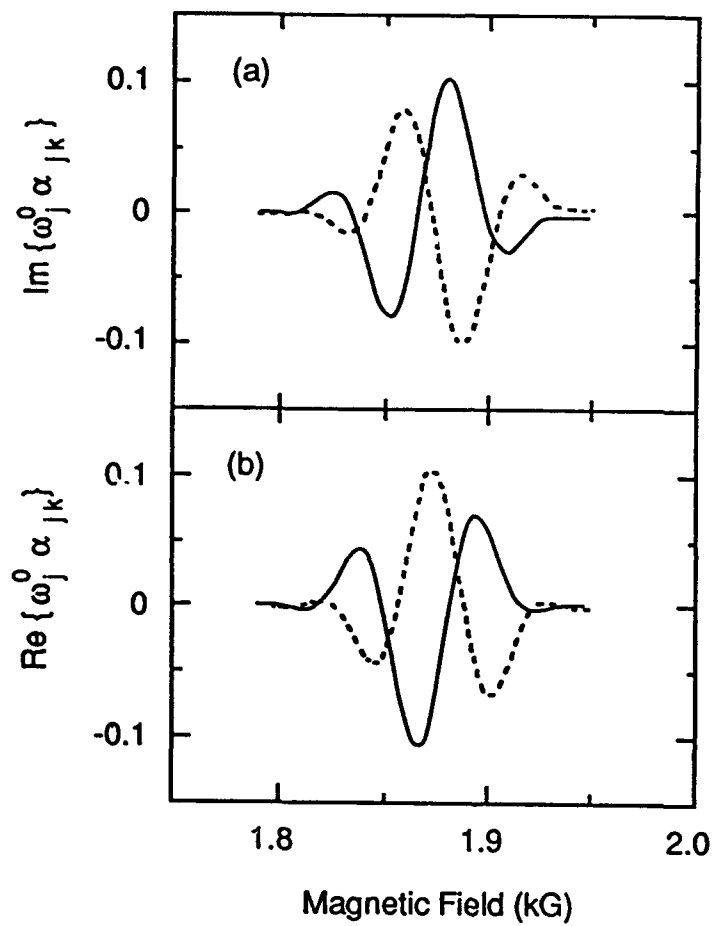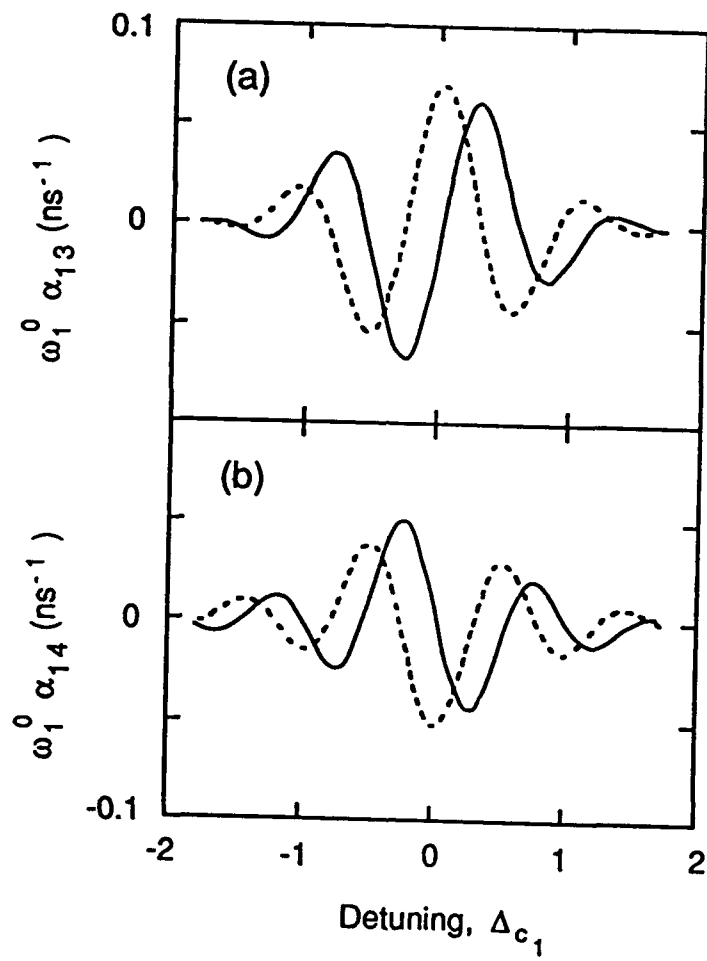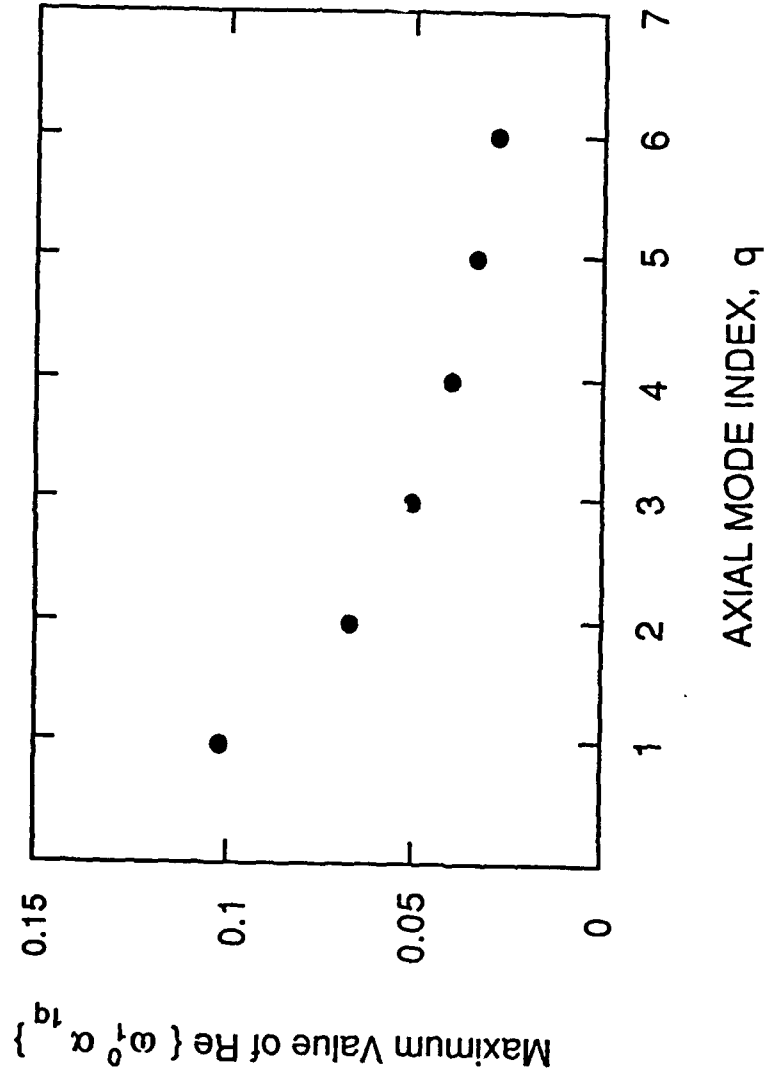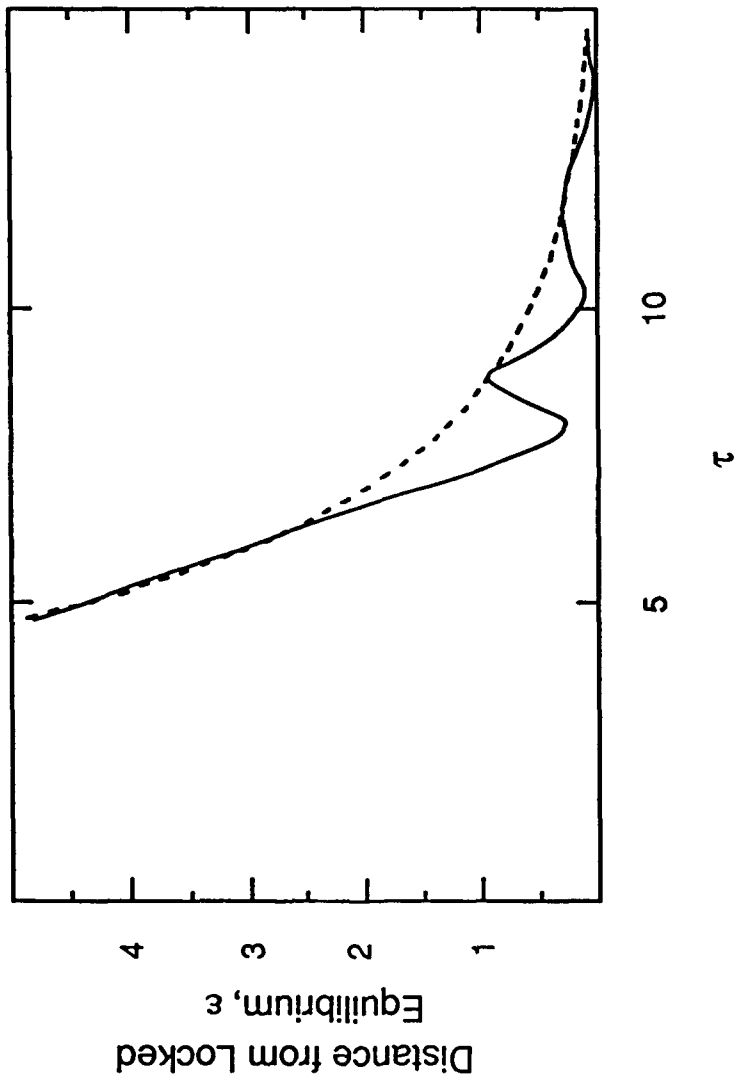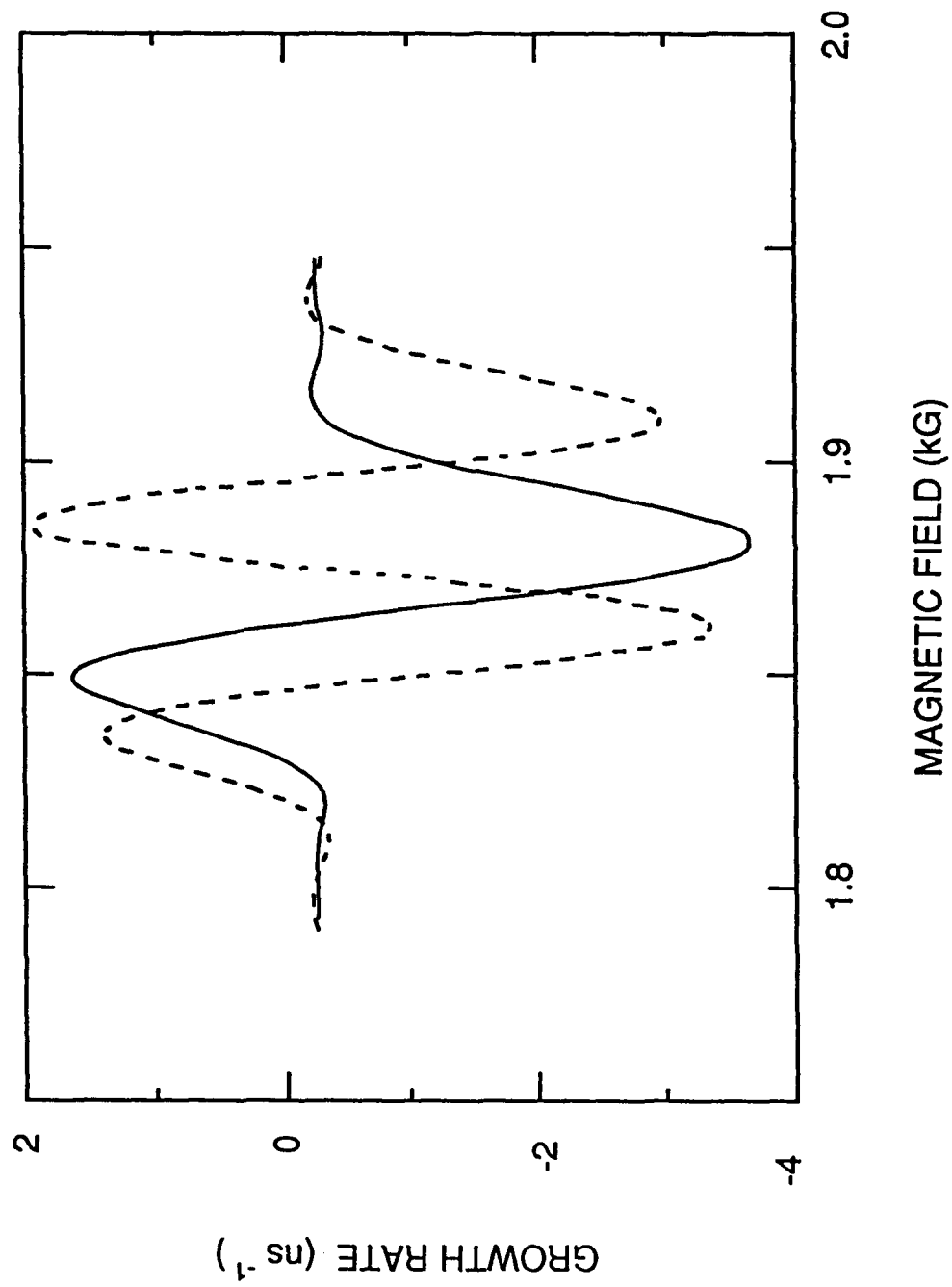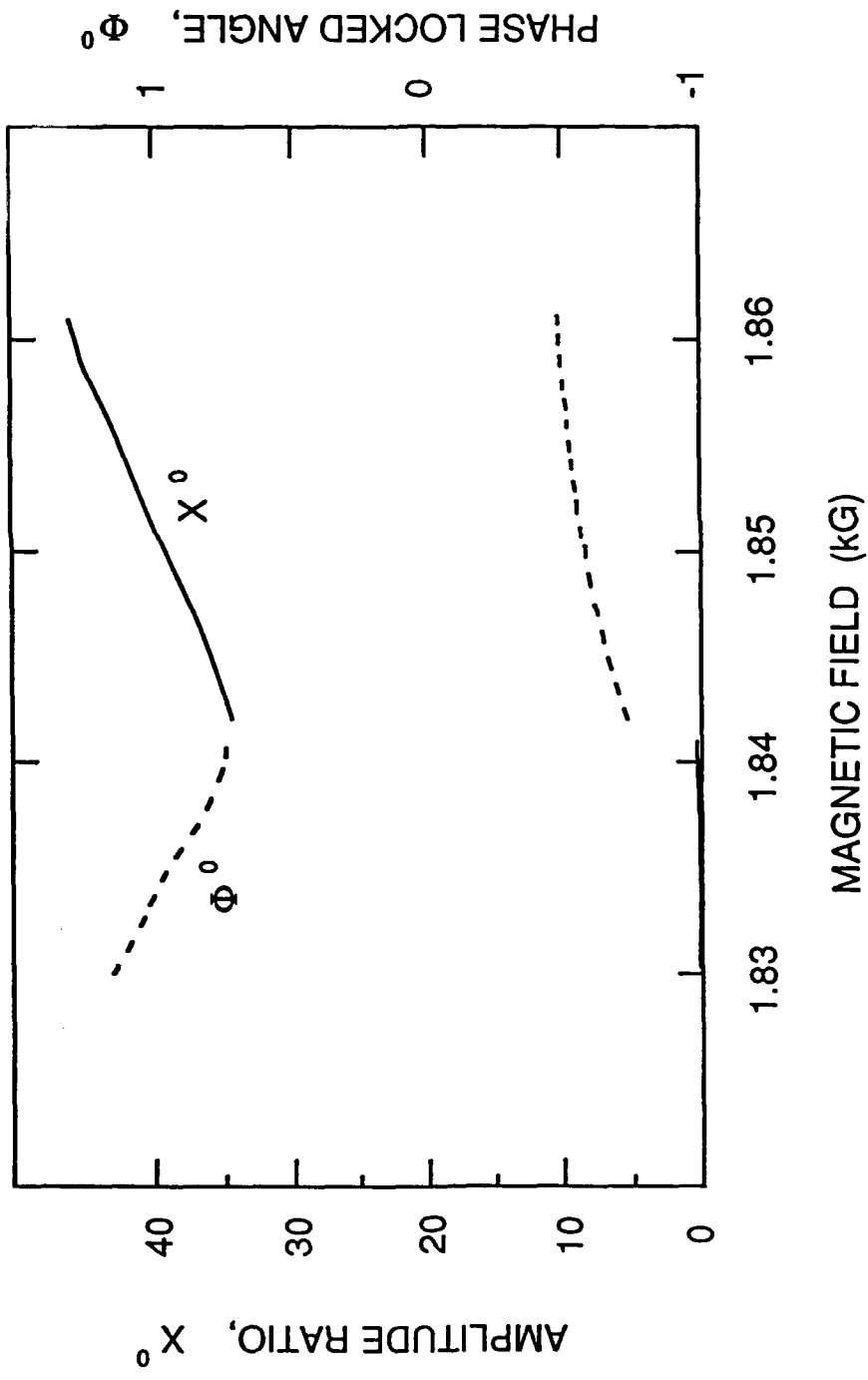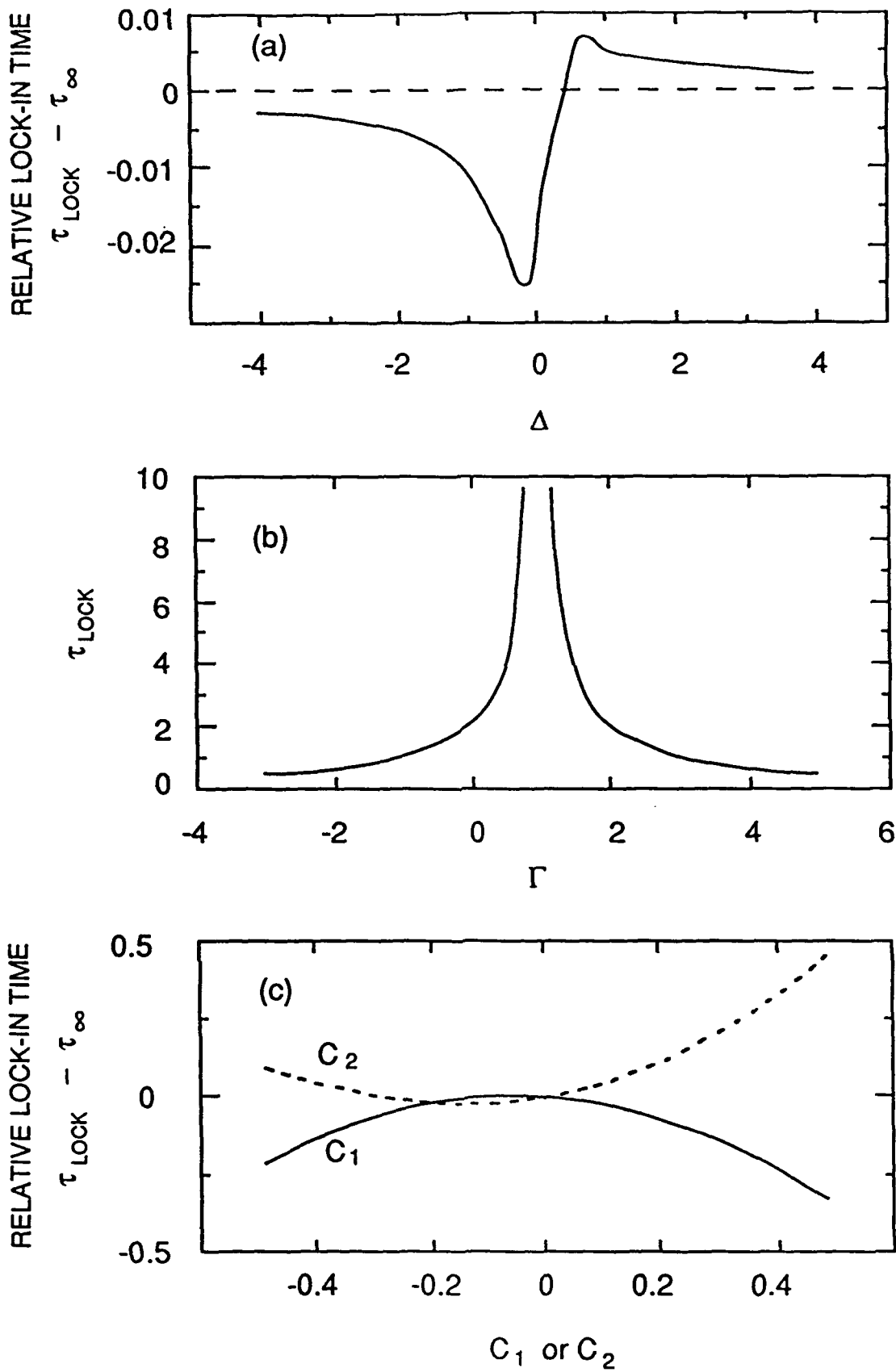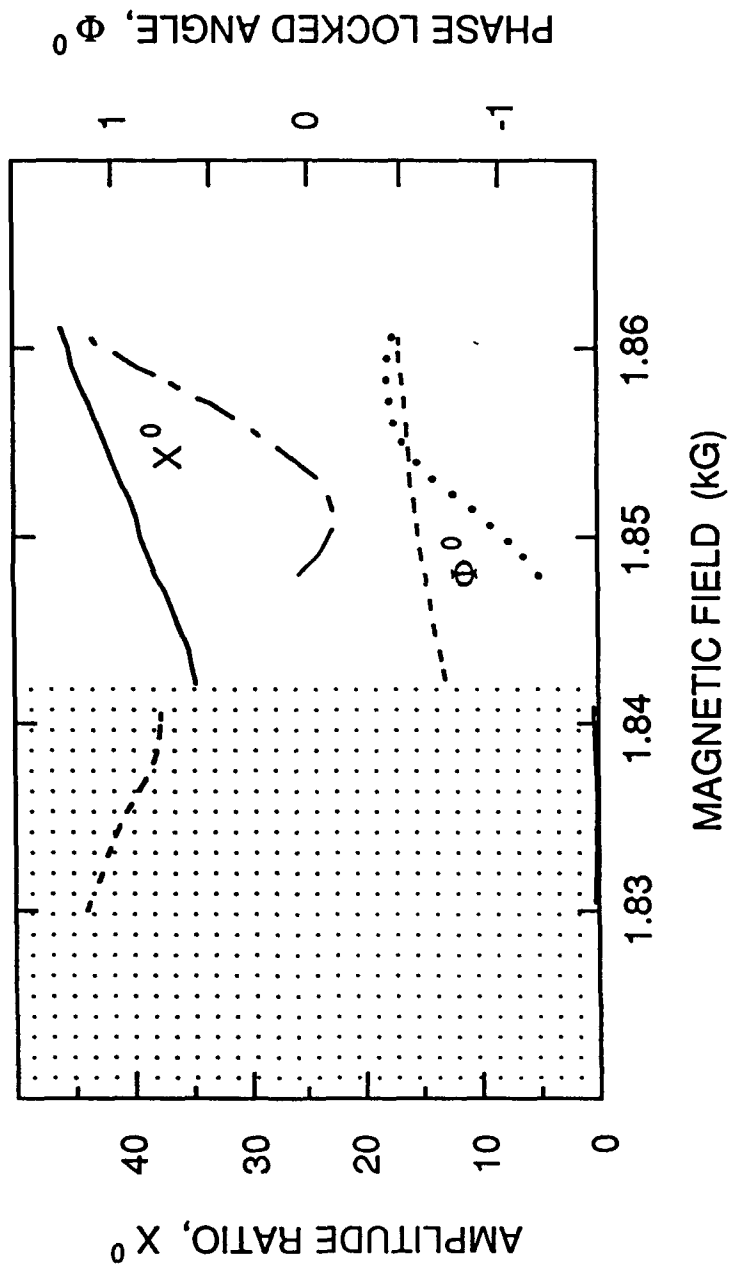
FIG. 16
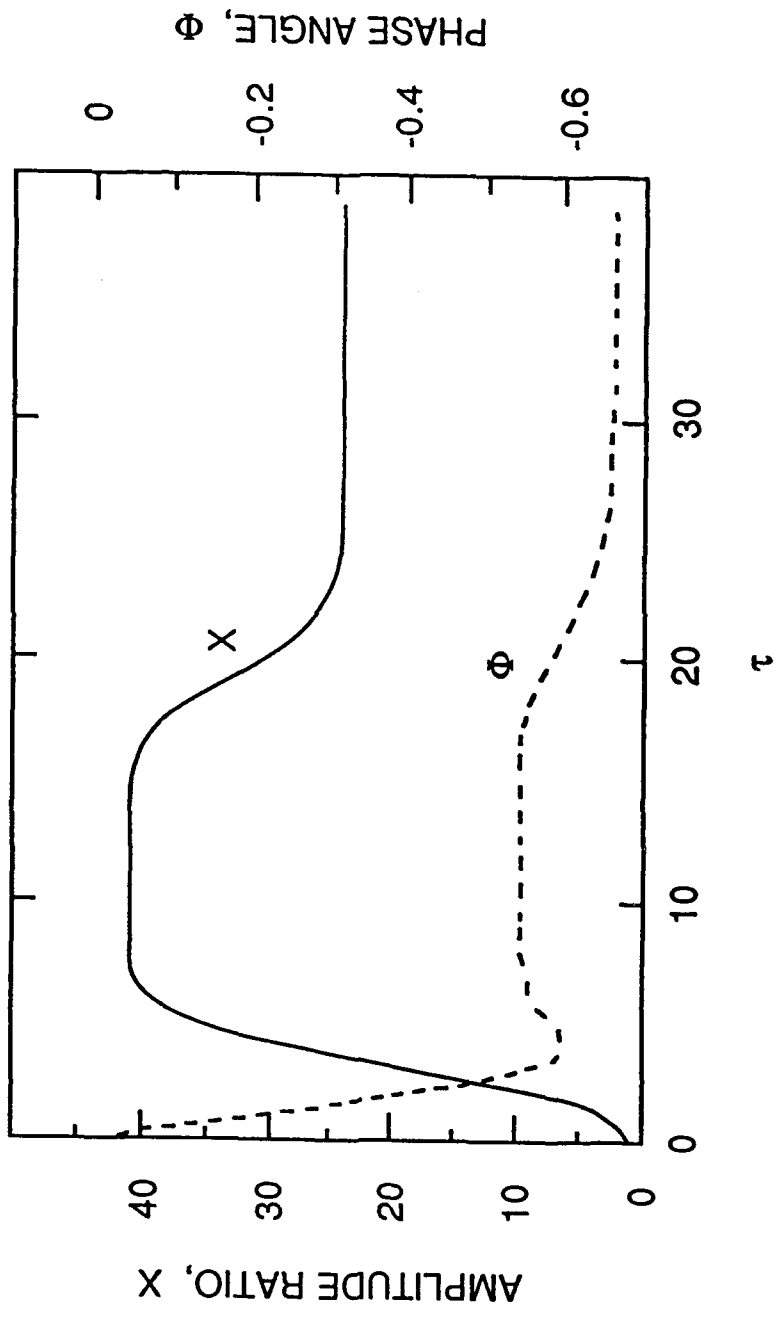
FIG. 11
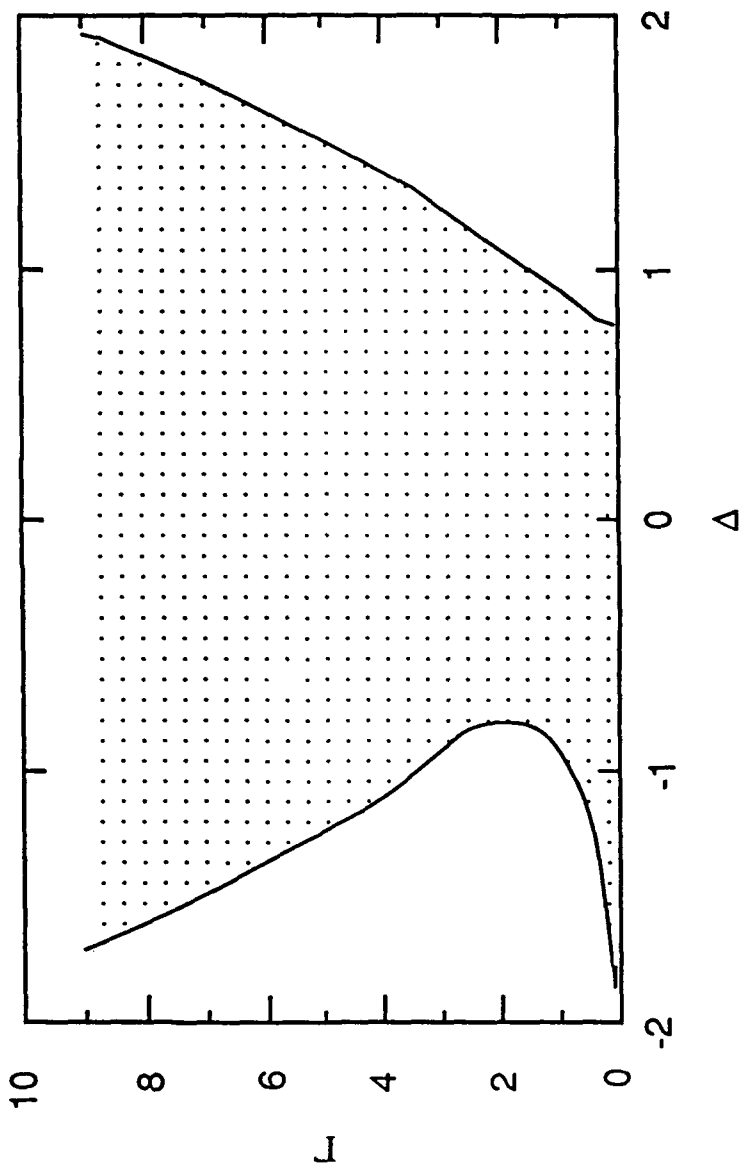
FIG. 12

PART II

Coupling Between Low Q Modes in a Beam-filled Resonator with Apertures

Abstract - Part II

Mode conversion and coupling are serious problems in low Q gyrotron operation, as they can result in efficiency reduction, spectral degradation, and undesirable thermal loading. The proper modeling of this phenomenon is thus an important goal in gyrotron theory. In this work, the electrodynamics of a low Q gyrotron cavity is described in terms of its short circuit eigenmodes. The correct set of eigenmodes in a simply connected gyrotron cavity are identified and computed. The oscillator equations describing the evolution in time of these eigenmodes are derived. Power generation and loss mechanisms in the cavity-waveguide structure are discussed. The electromagnetic solution is verified for the case of a rectangular waveguide coupling out of a cavity of rectangular cross-section. The case of a single frequency wave, propagating along the waveguide and exciting the cavity is discussed, and is compared with analytic theory in the limit of a short circuited waveguide. The theory of electromagnetic waves inside a cavity with Ohmic wall losses and external losses is investigated. Implementation of these developments into multimode gyrotron theory is discussed.

I. INTRODUCTION

In the ensuing work, the electromagnetic fields in a cavity are expanded in terms of the short circuit cavity eigenmodes. The short circuit modes correspond to the cavity completely enclosed by perfectly conducting walls. These short circuit cavity eigenmodes are orthonormal, and form a complete set with respect to the expansion of any arbitrary vector field in the cavity volume. Then the problem of representing the fields in the cavity reduces to determining the expansion coefficients multiplying the cavity eigenmodes.

The problem of electromagnetic field expansion in a cavity not completely enclosed by a perfect conductor has been tackled by many workers over the years. The case of a cavity completely enclosed by perfectly conducting walls was solved by Weyl.[1] Slater[2] gave a comprehensive theory covering this subject, but the set of vectors used by him are not correct in a cavity with open boundaries; he imposed the wrong set of boundary conditions on his irrotational functions, and as a result missed a capacitive term in his expression for input impedance. Moreover his set of vectors correspond to mixed boundary conditions and are difficult to compute. Teichmann and Wigner[3] showed for lossless cavities that an irrotational magnetic field is needed to completely expand the electromagnetic fields in the cavity excited through holes. This irrotational magnetic field vector is represented as the gradient of a scalar function u. The function u is determined by the value of the normal component of the magnetic field in the aperture, and by using the Neumann function of the cavity. The theory of Neumann functions and their properties is covered in some detail by Bergman and Schiffer,[4] and O.D.Kellogg.[5] As is the case with most Green's functions, the Neumann function for the cavity with a hole in the surface is difficult to evaluate, and is the main drawback of the theory presented by Teichmann and Wigner.

Schelkunoff[6] has demonstrated that Teichmann and Wigner's comments about the short circuit modes being incomplete with respect to the expansion of electromagnetic fields were not correct if use is made of a short circuit which conforms to the impressed field. Borgnis and Papas[7] wrote a very comprehensive review article on electromagnetic waveguides and resonators, in which they present the theory of cavity field expansions, and give a formula for computing the input admittance of the cavity resonator at the cavity-waveguide terminal plane. The expansion of cavity electromagnetic fields is also treated by Kurokawa,[8] and indeed this paper gives the most correct set of expansion vectors.

36

II. BACKGROUND

In this section some of the main ideas in the theory of cavity field expansion are discussed. First, the complete set of vector fields required to expand the electric and magnetic fields in a cavity with apertures on its surface is discussed. Using Maxwell's equations and the field expansions, coupled expressions for the field expansion coefficients are derived. Next, the oscillator equations which describe the time evolution of each of the cavity modes are derived.

A. *Complete Sets of Orthonorma. Vectors*

Kurokawa has shown that any arbitrary scalar function can be expanded in terms of an appropriate set of complete and orthonormal eigenfunctions in a volume V, enclosed by a surface S, if the set of eigenfunctions is composed of the solutions of the wave equation with the Dirichlet boundary condition:

$$\nabla^2 \psi_\alpha + k_\alpha^2 = 0 \text{ in volume V, } \psi_\alpha = 0 \text{ on surface S.}$$

The set ψ_α is a complete set of orthonormal functions (α=1,2,3...), and can be used in expanding an arbitrary piecewise continuous scalar function in V. Another complete set of orthonormal functions of equal generality of application is given by the solutions of

$$\nabla^2 \phi_\beta + k_\beta^2 = 0 \text{ in V, } \frac{\partial \phi_\beta}{\partial n} = 0 \text{ on S}$$

where the derivative is taken in a direction normal to the surface S.

An arbitrary piecewise continuous vector function in the volume V, can be expanded in a similar manner. One set of complete orthonormal vector functions is obtained as solutions of

$$\nabla^2 \vec{\Psi}_p + k_p^2 \vec{\Psi}_p = 0 \text{ in V, } \vec{n} \times \vec{\Psi}_p = 0, \nabla \cdot \vec{\Psi}_p = 0 \text{ on S } (p=0,1,2,...). \tag{1}$$

Here $\vec{n}$ is a unit outward normal from the cavity surface. Another complete set of eigenvectors is obtained as solutions of

$$\nabla^2 \vec{\Phi}_q + k_q^2 \vec{\Phi}_q = 0 \text{ in V, } \vec{n} \times \nabla \times \vec{\Phi}_q = 0, \vec{n} \cdot \vec{\Phi}_q = 0 \text{ on S } (q=0,1,2,..). \tag{2}$$

37

Some of the $\vec{\Psi}_p$ and $\vec{\Phi}_q$ have the same eigenvalues k_α; these are related to each other through the curl operation as

$$\nabla\times\vec{\Psi}_\alpha=k_\alpha\vec{\Phi}_\alpha \text{ and } \nabla\times\vec{\Phi}_\alpha=k_\alpha\vec{\Psi}_\alpha .$$

All the other $\vec{\Psi}_p$ and $\vec{\Phi}_q$ that do not have common eigenvalues are irrotational; if they are denoted as $\vec{F}_\alpha$ and $\vec{G}_\lambda$ ($\alpha=0,1,2..$) and ($\lambda=0,1,2...$), then

$$\nabla\times\vec{F}_\alpha=0 \text{ and } \nabla\times\vec{G}_\lambda=0.$$

If $\vec{F}_\alpha$ and $\vec{G}_\lambda$ have nonzero eigenvalues, then they can be represented through the gradient operation as

$$k_\alpha\vec{F}_\alpha=\nabla\psi_\alpha \text{ and } k_\lambda\vec{G}_\lambda=\nabla\phi_\lambda$$

where

$$\nabla^2\psi_\alpha+k_\alpha^2 = 0 \text{ in } V, \psi_\alpha = 0 \text{ on } S$$

and

$$\nabla^2\phi_\lambda+k_\lambda^2\phi_\lambda=0 \text{ in } V \text{ and } \frac{\partial\phi_\lambda}{\partial n}=0 \text{ on } S .$$

The vector electric and magnetic fields in the cavity are expanded in a manner analogous to the above expansions. The solenoidal vectors required in the electric field expansion are denoted as $\vec{E}_\alpha$ and the irrotational vectors in the electric field expansion are denoted as $\vec{F}_\alpha$. In a simply connected cavity however, no $\vec{F}_\alpha$ are required to expand the electric field since all the $\vec{F}_\alpha$ are orthogonal to the real electric field. That this is so can be quickly seen by integrating the scalar product of total electric field $\vec{E}$ with a particular modal vector $\vec{F}_\alpha$ over the cavity volume. Assuming that the actual electromagnetic field is periodic with a finite period ω, this leads to the surface integral of $\vec{n}\times\vec{F}_\alpha\cdot\vec{H}$, and this vanishes because from eqn.(1), it can be seen that $\vec{n}\times\vec{F}_\alpha$ is equal to zero on the surface of the cavity.

In a similar fashion, the magnetic field is expanded in terms of the solenoidal vectors $\vec{H}_\alpha$ and the irrotational vectors $\vec{G}_\lambda$. That the *irrotational* vectors $\vec{G}_\lambda$ are required to expand the magnetic field may look strange, but that this is the case can be seen from the Helmholtz theorem, which states that a given vector field in a region V enclosed by a surface S can be expressed as the sum of the gradient of a scalar

38

field and the curl of a vector field. Only when the divergence of the given vector field is zero in V, and its normal component zero on S, can it be set equal to the rotation of another vector field. Similarly, only when the curl of the given vector field is zero in volume V, and its tangential component equals zero on the surface, can it be set equal to the gradient of a scalar field. In the first case, the vector field is purely solenoidal, and in the second case it is purely irrotational. The boundary condition. on the surface are important to distinguish the purely solenoidal or purely irrotational vector fields, and if a vector field is not purely irrotational, then even if its curl is zero in the volume V, it can not be generally written as the gradient of a scalar field. In the same way, even if the divergence of a vector field is zero in the volume V, if it is not purely solenoidal, then it can not generally be written as the curl of a vector field. Thus we can write

$$\vec{E} = \sum_{\alpha} \vec{E}_{\alpha} \int_{V} \vec{E} \cdot \vec{E}_{\alpha} dv \tag{3}$$

$$\vec{H} = \sum_{\alpha} \vec{H}_{\alpha} \int_{V} \vec{H} \cdot \vec{H}_{\alpha} dv + \sum_{\lambda} \vec{G}_{\lambda} \int_{V} \vec{H} \cdot \vec{G}_{\lambda} dv \tag{4}$$

$$\vec{J} = \sum_{\alpha} \vec{F}_{\alpha} \int_{V} \vec{J} \cdot \vec{E}_{\alpha} dv \tag{5}$$

$$\rho = \sum_{\alpha} \psi_{\alpha} \int_{V} \rho \psi_{\alpha} dv \tag{6}$$

where $\vec{J}$ and ρ are the volume current and charge densities respectively. All the integrations in eqs.(3)-(6) are done over the volume of the cavity. The eigenmodes satisfy the relations

$$\nabla^2 \vec{E}_{\alpha} + k_{\alpha}^2 \vec{E}_{\alpha} = 0 \text{ in } V, \vec{n} \times \vec{E}_{\alpha} = 0, \nabla \cdot \vec{E}_{\alpha} = 0 \text{ on } S+S' \tag{7}$$

$$\nabla^2 \vec{H}_{\alpha} + k_{\alpha}^2 \vec{H}_{\alpha} = 0 \text{ in } V, \vec{n} \times \nabla \times \vec{H}_{\alpha} = 0, \vec{n} \cdot \vec{H}_{\alpha} = 0 \text{ on } S+S \tag{8}$$

$$\nabla^2 \vec{G}_{\lambda} + k_{\lambda}^2 \vec{G}_{\lambda} = 0 \text{ in } V, \vec{n} \times \nabla \times \vec{G}_{\lambda} = 0, \vec{n} \cdot \vec{G}_{\lambda} = 0 \text{ on } S+S' \tag{9}$$

$$\nabla \times \vec{E}_{\alpha} = k_{\alpha} \vec{H}_{\alpha} \text{ and } \nabla \times \vec{H}_{\alpha} = k_{\alpha} \vec{E}_{\alpha} \text{ and } \nabla \times \vec{G}_{\lambda} = 0 \tag{10}$$

and the orthonormality relations

$$\int_V \vec{E}_\alpha \cdot \vec{E}_\beta dv = \delta_{\alpha\beta}, \quad \int_V \vec{H}_\alpha \cdot \vec{H}_\beta dv = \delta_{\alpha\beta}, \quad \int_V \vec{G}_\alpha \cdot \vec{G}_\beta dv = \delta_{\alpha\beta} \tag{11}$$

where $\delta_{\alpha\beta}$ is the Kronecker delta function ($\delta_{\alpha\beta}=1$ if $\alpha = \beta$ and $\delta_{\alpha\beta}=0$ if $\alpha \neq \beta$). Here S denotes the portion of the cavity surface which is a conducting material, and S' denotes the portion that is an aperture.

From Maxwell's equations it is seen that $\nabla \times \vec{E}$ has the properties of a magnetic field, hence $\vec{H}_\alpha$ and $\vec{G}_\lambda$ are used in the expansion of $\nabla \times \vec{E}$. Similarly, since $\nabla \times \vec{H}$ has the properties of an electric field, $\vec{E}_\alpha$ are used in its expansion. Thus

$$\nabla \times \vec{E} = \sum_\alpha \vec{H}_\alpha \int_V \nabla \times \vec{E} \cdot \vec{H}_\alpha dv + \sum_\lambda \vec{G}_\lambda \int_V \nabla \times \vec{E} \cdot \vec{G}_\lambda dv$$

and

$$\nabla \times \vec{H} = \sum_\alpha \vec{E}_\alpha \int_V \nabla \times \vec{H} \cdot \vec{E}_\alpha dv.$$

B. *Oscillator Equations*

From vector identities and using the properties of the eigenvectors, the following relations are obtained

$$\nabla \times \vec{E} \cdot \vec{H}_\alpha = \nabla \cdot \vec{E} \times \vec{H}_\alpha + k_\alpha \vec{E} \cdot \vec{E}_\alpha$$

$$\nabla \times \vec{E} \cdot \vec{G}_\lambda = \nabla \cdot \vec{E} \times \vec{G}_\lambda$$

$$\nabla \times \vec{H} \cdot \vec{E}_\alpha = \nabla \cdot \vec{H} \times \vec{E}_\alpha + k_\alpha \vec{H} \cdot \vec{H}_\alpha .$$

Substituting these relations in eqs. (3) & (4), using the divergence theorem, eqn.(11), and using the boundary conditions

$$\vec{n} \times \vec{E}_\alpha = 0 \text{ on } S+S' \text{ and } \vec{n} \cdot \vec{H}_\alpha = 0 \text{ on } S+S'$$

the following equations are obtained

$$k_\alpha \int_V \vec{H} \cdot \vec{H}_\alpha dv - \varepsilon \frac{\partial}{\partial t} \int_V \vec{E} \cdot \vec{E}_\alpha dv = \int_V \vec{J} \cdot \vec{E}_\alpha dv \tag{12}$$

40

$$k_\alpha \int_V \vec{E} \cdot \vec{E}_\alpha dv + \mu \frac{\partial}{\partial t} \int_V \vec{H} \cdot \vec{H}_\alpha dv = - \int_{S+S'} \vec{n} \times \vec{E} \cdot \vec{H}_\alpha ds \qquad (13)$$

$$\mu \frac{\partial}{\partial t} \int_V \vec{H} \cdot \vec{G}_\lambda dv + \int_{S+S'} \vec{n} \times \vec{E} \cdot \vec{G}_\lambda ds = 0. \qquad (14)$$

The following two oscillator equations are obtained by eliminating the expansion coefficients from the coupled eqs. (12)-(14)

$$\frac{1}{c^2} \frac{\partial^2}{\partial t^2} \int_V \vec{E} \cdot \vec{E}_\alpha dv + k_\alpha^2 \int_V \vec{E} \cdot \vec{E}_\alpha dv = -k_\alpha \int_{S+S'} \vec{n} \times \vec{E} \cdot \vec{H}_\alpha dS - \mu \frac{\partial}{\partial t} \int_V \vec{J} \cdot \vec{E}_\alpha dv \qquad (15)$$

$$\frac{1}{c^2} \frac{\partial^2}{\partial t^2} \int_V \vec{H} \cdot \vec{H}_\alpha dv + k_\alpha^2 \int_V \vec{H} \cdot \vec{H}_\alpha dv = k_\alpha \int_V \vec{J} \cdot \vec{E}_\alpha dV - \varepsilon \frac{\partial}{\partial t} \int_{S+S'} \vec{n} \times \vec{H} \cdot \vec{H}_\alpha ds \qquad (16)$$

These oscillator equations form the basis of the subsequent gyrotron cavity theory. They will now be solved subject to different boundary conditions.

III. EXCITATION OF CAVITY FIELDS

In this section, the oscillator eqs.(15) and (16) are solved, keeping different source terms on the right hand side in each problem. This is a useful exercise because it enables us to check the results of the field expansion theory in cases with relatively simple geometry. By including more and more terms on the right hand side, we make an orderly progress toward the gyrotron problem, which is solved using a circular-cylindrical geometry and a convection current in the interior of the cavity.

A. Cavity Excited by a Waveguide

The oscillator eqs.(15) and (16) together with eqs.(3) and (4) describe completely the time evolution of electromagnetic fields in a cavity. Here as a first step, these equations are solved in a cavity excited by a waveguide (Fig.1) when a single frequency wave propagates down the waveguide. This steady state problem is solved in the frequency domain by performing the Fourier transformation of the oscillator equations . Writing

41

$$f_\alpha = \int_V \vec{E} \cdot \vec{E}_\alpha dv \text{ and } h_\alpha = \int_V \vec{H} \cdot \vec{H}_\alpha dv \text{ and } g_\lambda = \int_V \vec{H} \cdot \vec{G}_\lambda dv$$

and Fourier transforming eqs.(12), (14) and (15), one can write

$$h_\alpha(\omega) = \frac{j\omega\epsilon}{k_\alpha} f_\alpha(\omega) \text{ and } g_\lambda(\omega) = \frac{-1}{j\omega\mu} \int_{S+S'} \vec{n}\times\vec{E}(\vec{r},\omega)\cdot \vec{G}_\lambda ds \qquad (17)$$

$$\left(k_\alpha^2 - \frac{\omega^2}{c^2}\right)f_\alpha(\omega) = -k_\alpha \int_{S+S'} \vec{n}\times\vec{E}(\vec{r},\omega)\cdot\vec{H}_\alpha(\vec{r})ds + j\omega\mu \int_V \vec{J}(\vec{r},\omega)\cdot \vec{E}_\alpha(\vec{r})dv \qquad (18)$$

When it is assumed that there is no beam in the cavity, then the second term on the right hand side vanishes. If it is also assumed that the walls of the cavity are made of a perfect conductor, then the tangential component of the electric field is equal to zero on S, and eqn.(18) becomes

$$\left(k_\alpha^2 - \frac{\omega^2}{c^2}\right)f_\alpha(\omega) = -k_\alpha \int_{S'} \vec{n}\times\vec{E}(\vec{r},\omega)\cdot \vec{H}_\alpha(\vec{r})ds \qquad (19)$$

To solve for $f_\alpha(\omega)$ we need a knowledge of $\vec{n}\times\vec{E}$ at the waveguide-cavity interface (aperture). This field may be found by matching the field in the waveguide with that of the cavity across the aperture. The waveguide fields expressed as summation of waveguide eigenmodes are

$$\vec{E} = \sum_s v_s\vec{F}_{t,s} + i_s Z_s \vec{F}_{z,s} \qquad (20)$$

$$\vec{H} = \sum_s i_s\vec{G}_{t,s} + \frac{v_s}{Z_s}\vec{G}_{z,s} \qquad (21)$$

where s represents the s'th waveguide mode, and t and z denote the transverse and the longitudinal (in the increasing direction along z-axis) directions. $\vec{F}_{ts}$ and $\vec{G}_{ts}$ satisfy the orthonormality relations given by

$$\int_{S'} \vec{F}_{tr}\cdot \vec{F}_{ts}ds = \int_{S'} \vec{G}_{tr}\cdot \vec{G}_{ts}ds = \int_{S'} \vec{F}_{tr}\times\vec{G}_{ts}\cdot\vec{z}\,ds = \delta_{rs} \qquad (22)$$

where δ_{rs} is the Kronecker delta function as defined earlier, and $\vec{z}$ is a unit vector in the z-direction. Substituting eqs. (20) and (21) into eqn.(19) results in

42

$$f_\alpha(\omega) = \frac{k_\alpha}{\left(k_\alpha^2 - \frac{\omega^2}{c^2}\right)} \sum_s \gamma_{\alpha s} v_s \qquad (23)$$

where

$$\gamma_{\alpha s} = \int_{S'} \vec{H}_\alpha \cdot \vec{G}_{t,s} ds .$$

For the rectangular cavity shown in fig.1, the TE(to z) cavity eigenmodes are as follows:

$$H_{\alpha_z} = \frac{\partial^2 \psi_\alpha}{\partial z^2} + k_\alpha^2 \psi_\alpha, \; H_{\alpha_x} = \frac{\partial^2 \psi_\alpha}{\partial x \partial z}, \; H_{\alpha_y} = \frac{\partial^2 \psi_\alpha}{\partial y \partial z}, \; E_{\alpha_x} = -j\omega_\alpha \mu \frac{\partial \psi_\alpha}{\partial y}, \; E_{\alpha_y} = j\omega_\alpha \mu \frac{\partial \psi_\alpha}{\partial x}$$

where

$$\psi_\alpha = \frac{1}{hk_\alpha} \sqrt{\frac{\epsilon_m \epsilon_n \epsilon_p}{abd}} \cos\left(\frac{m\pi x}{a}\right) \cos\left(\frac{n\pi y}{b}\right) \sin\left(\frac{p\pi z}{d}\right)$$

$$k_\alpha = \sqrt{\left(\frac{m\pi}{a}\right)^2 + \left(\frac{n\pi}{b}\right)^2 + \left(\frac{p\pi}{d}\right)^2}, \; h = \sqrt{\left(\frac{m\pi}{a}\right)^2 + \left(\frac{n\pi}{b}\right)^2}, \; \omega_\alpha = ck_\alpha$$

α denotes the triple indices (m,n,p) and ϵ_m, ϵ_n, and ϵ_p are the Neumann factors which take on a value of 2 if the subscript-index is not equal to zero, and have a value of 1 if the subscript-index equals zero. Similarly, the TM(to z) cavity eigenmodes are defined as:

$$E_{\alpha_z} = \frac{\partial^2 \psi_\alpha}{\partial z^2} + k_\alpha^2 \psi_\alpha, \; E_{\alpha_x} = \frac{\partial^2 \psi_\alpha}{\partial x \partial z}, \; E_{\alpha_y} = \frac{\partial^2 \psi_\alpha}{\partial y \partial z}, \; H_{\alpha_x} = j\omega_\alpha \epsilon \frac{\partial \psi_\alpha}{\partial y}, \; H_{\alpha_y} = -j\omega_\alpha \epsilon \frac{\partial \psi_\alpha}{\partial x}$$

where

$$\psi_\alpha = \frac{1}{hk_\alpha} \sqrt{\frac{\epsilon_m \epsilon_n \epsilon_p}{abd}} \sin\left(\frac{m\pi x}{a}\right) \sin\left(\frac{\pi}{b}\right) \cos\left(\frac{p\pi z}{d}\right)$$

with h, k_α, and ω_α defined as above. The $\vec{G}_\lambda$ are defined as

$$G_{\lambda_x} = \frac{1}{k_\lambda} \frac{\partial \phi_\lambda}{\partial x}, \; G_{\lambda_y} = \frac{1}{k_\lambda} \frac{\partial \phi_\lambda}{\partial y}, \; G_{\lambda_z} = \frac{1}{k_\lambda} \frac{\partial \phi_\lambda}{\partial z}$$

where

$$\phi_\lambda = \frac{1}{k_\lambda} \sqrt{\frac{\epsilon_m \epsilon_n \epsilon_p}{abd}} \cos\left(\frac{m\pi x}{a}\right) \cos\left(\frac{n\pi y}{b}\right) \cos\left(\frac{p\pi z}{d}\right)$$

43

and

$$k_\lambda = \sqrt{\left(\frac{m\pi}{a}\right)^2 + \left(\frac{n\pi}{b}\right)^2 + \left(\frac{p\pi}{d}\right)^2} \, .$$

The waveguide eigenmodes are defined in a similar way. The TE(to z) eigenmodes are defined

$$\vec{E}_s = -j\omega\mu\nabla\times\vec{\psi}_s, \text{ where } \vec{\psi}_s = -\vec{z}\frac{1}{j\omega\mu h}\sqrt{\frac{\epsilon_m\epsilon_l}{ac}}\cos\left(\frac{m\pi x}{a}\right)\cos\left(\frac{l\pi y}{c}\right)e^{-j\beta z}$$

$$\vec{H}_s = \nabla\times\nabla\times\vec{\psi}_s, \text{ where } \vec{\psi}_s = -\vec{z}\frac{1}{j\beta h}\sqrt{\frac{\epsilon_m\epsilon_l}{ac}}\cos\left(\frac{m\pi x}{a}\right)\cos\left(\frac{l\pi y}{c}\right)e^{-j\beta z}$$

where s denotes the double waveguide indices (m,l), ϵ_m, ϵ_l are the Neumann factors as defined earlier, h and β are defined

$$h = \sqrt{\left(\frac{m\pi}{a}\right)^2 + \left(\frac{l\pi}{c}\right)^2} \text{ and } \beta = \sqrt{\frac{\omega^2}{c^2} - \frac{\pi^2}{a^2}} \, .$$

The TM(to z) eigenmodes are defined

$$\vec{E} = \nabla\times\nabla\times\vec{\psi}, \text{ where } \vec{\psi} = -\vec{z}\frac{1}{j\beta h}\sqrt{\frac{\epsilon_m\epsilon_l}{ac}}\sin\left(\frac{m\pi x}{a}\right)\sin\left(\frac{l\pi y}{c}\right)e^{-j\beta z}$$

$$\vec{H} = j\omega\epsilon\nabla\times\vec{\psi}, \text{ where } \vec{\psi} = -\vec{z}\frac{1}{j\omega\epsilon h}\sqrt{\frac{\epsilon_m\epsilon_l}{ac}}\sin\left(\frac{m\pi x}{a}\right)\sin\left(\frac{l\pi y}{c}\right)e^{-j\beta z}.$$

The v_s are the amplitude coefficients of waveguide electric field modes at the aperture; they need to be computed before $f_\alpha(\omega)$ can be evaluated. From eqs.(20) and (21) it can be seen that

$$i_r = \int_{S'} \vec{H}\cdot\vec{G}_{t,r}ds. \tag{24}$$

By substitution of eqn.(5) into eqn.(24)

$$i_r = \sum_s Y_{rs}v_s \tag{25}$$

where

$$Y_{rs} = \frac{j\omega}{\mu}\sum_\alpha \frac{\gamma_{\alpha s}\gamma_{\alpha r}}{\omega_\alpha^2 - \omega^2} + \frac{1}{j\omega\mu}\sum_\lambda \beta_{\lambda r}\beta_{\lambda s} \tag{26}$$

44

with

$$\beta_{\lambda r} = \int_{S'} \vec{G}_\lambda \cdot \vec{G}_{tr} ds .$$

The Y_{rs} are admittance coefficients, and describe how the current in the r'th mode of the waveguide couples into various cavity modes, and how each of them in turn couple back into the s'th waveguide mode. The above equation for i_r actually describes a system of linear equations which are solved to compute the v_s. The solution is given in the following.

A small distance away from the aperture, there are a great number of waveguide modes propagating in both forward and backward directions, because of the impedance mismatch at the aperture. While the amplitude of most of these modes will fall off rapidly away from the aperture (because the waveguide is designed for dominant mode propagation), their amplitudes right at the aperture are not necessarily negligible. Thus the v_s at a point in the waveguide is composed of v_s^+ and v_s^-, with the superscripts indicating waves propagating in the +z and -z directions.

$$v_s = v_s^+ - v_s^- \text{ and } i_s = i_s^+ + i_s^- \qquad \text{for TE modes} \qquad (27)$$

and

$$v_s = v_s^+ + v_s^- \text{ and } i_s = i_s^+ - i_s^- \qquad \text{for TM modes} \qquad (28)$$

with $i_s^- = Y_{\omega_s} v_s^-$ and $i_s^+ = Y_{\omega_s} v_s^+$, where Y_{ω_s} is the admittance of the s'th mode .

Using matrix notation, eqn.(25) can be written as

$$\left(v_{TE}^+\right) + \left(v_{TE}^-\right) = \left(Y_{\omega_{TE}}\right)^{-1}\left[\left(Y_{TE\text{-}TE}\right)\left(\left(v_{TE}^+\right) - \left(v_{TE}^-\right)\right) + \left(Y_{TE\text{-}TM}\right)\left(\left(v_{TM}^+\right) + \left(v_{TM}^-\right)\right)\right].$$

and

$$\left(v_{TM}^+\right) - \left(v_{TM}^-\right) = \left(Y_{\omega_{TM}}\right)^{-1}\left[\left(Y_{TM\text{-}TE}\right)\left(\left(v_{TE}^+\right) - \left(v_{TE}^-\right)\right) + \left(Y_{TM\text{-}TM}\right)\left(\left(v_{TM}^+\right) + \left(v_{TM}^-\right)\right)\right].$$

Upon rearrangement, these equations yield

$$\left(v_{TE}^-\right) = (A_1)\left(v_{TE}^+\right) + (A_2)\left(v_{TM}^+\right) \text{ and } \left(v_{TM}^-\right) = (B_1)\left(v_{TE}^+\right) + (B_2)\left(v_{TM}^+\right) .$$

Thus v_{TE}^- and v_{TM}^- are solved in terms of the known quantities v_{TE}^+ and v_{TM}^+. From eqn.(23), it can be seen that all the f_α can be determined when the v_s are known.

45

The results obtained by solving the above system of equations may be best checked in the case of a short-circuited waveguide (Fig. 2) by making the height of the cavity and height of the waveguide equal. It is assumed that the waveguide is designed for the dominant TE_{10} mode propagation, and that the amplitude $v^+_{s=TE_{10}} = 1$. Figure 3 shows the normalized admittance at the aperture as a function of the frequency. The result obtained from the cavity field expansion theory is compared with an analytic expression for admittance at the aperture plane in the short-circuited waveguide. As can be seen, the results are in very good agreement. This can also be seen by comparing the expressions for aperture admittance from the cavity eigenmode expansion theory and the short circuited waveguide.

For a short circuited waveguide, the modal admittance for the dominant TE_{10} mode at a distance d from the shorted end of the waveguide is given as

$$Y(\omega) = -j\frac{\beta}{\mu\omega}\cot(\beta d) \quad \text{where } \beta = \sqrt{\frac{\omega^2}{c^2} - \frac{\pi^2}{a^2}} \tag{29}$$

Expanding this function $Y(\omega)$ as a Mittag-Leffler series of partial fractions using the theory of residues, we obtain

$$Y(\omega) = \sum_{p=1}^{\infty} \left(\frac{p\pi}{d}\right)^2 \frac{1}{k_\alpha^2 \mu d} \frac{j2\omega}{\omega_\alpha^2 - \omega^2} + \frac{\pi}{j\omega\mu a}\coth\frac{\pi d}{a}. \tag{30}$$

Equation 30 is the same as eqn.(26), when eqn.(26) is expanded over the TE_{10p} type modes (since in the shorted waveguide only the TE_{10p} cavity eigenmodes are needed in the expansion for the dominant TE_{10} waveguide mode propagation). The first summation on the right hand side in eqn.(30) is the contribution of the solenoidal modes to the admittance function, and the second term is the contribution of the irrotational modes to the admittance. (The aperture admittance exhibits resonance behavior at the cavity (10p modes) resonant frequencies. This can be readily seen from eqn.(29) and eqn.(30).

Figures 4 and 5 show the y-component of the electric field plotted vs z-axis along the center of the waveguide for the short-circuited waveguide case. Again, the results from the cavity field expansion theory are compared with the waveguide theory expression for electric field in the shorted waveguide. As can be seen, the results are in very good agreement except very near the aperture, where the field obtained from the cavity field expansion drops off to zero, unlike the waveguide field. This is to be expected, since all the eigenmodes used in the cavity field expansion have a zero tangential component on the cavity surface. This is a limitation imposed by the nature of the modes used in the expansion, and can not be corrected regardless of how many modes are used in the expansion. However, by increasing the number of eigenmodes used in the expansion of cavity fields, the expanded field can be made to

46

better agree with the true field. This result is somewhat analogous to the Fourier series expansion using sine terms only.

Figure 6 shows the normalized admittance of a cavity as a function of frequency when the cavity and the waveguide have different heights. The admittance function exhibits resonance behavior at all the ω_α ($\alpha = 1np$ modes). Since the width of the waveguide and cavity are equal, only ($\alpha = 1np$) modes need to be considered. Figure 7 shows the profile of the y-component of the electric field along the cavity axis, when the cavity and waveguide have different heights. As can be expected, the field drops to zero near the aperture.

Figure 8 shows the energy stored in the cavity as a function of the frequency. The stored electric energy in a cavity can be computed from

$$W_e = \frac{\varepsilon}{4} \int_V \vec{E} \cdot \vec{E}^* \, dv = \frac{\varepsilon}{4} \int_V \left(\sum_\alpha f_\alpha \vec{E}_\alpha \right) \cdot \left(\sum_\beta f_\beta \vec{E}_\beta \right)^* dv = \sum_\alpha \frac{|f_\alpha|^2}{4} \ .$$

The stored magnetic field energy is computed from

$$W_m = \frac{\mu}{4} \int_V \vec{H} \cdot \vec{H}^* \, dv = \frac{\mu}{4} \int_V \left(\sum_\alpha h_\alpha \vec{H}_\alpha + g_\alpha \vec{G}_\alpha \right) \cdot \left(\sum_\beta h_\beta \vec{H}_\beta + g_\beta \vec{G}_\beta \right)^* dv$$

or

$$W_m = \frac{\mu}{4} \sum_\alpha \left\{ |h_\alpha|^2 + |g_\alpha|^2 \right\}$$

and the total energy stored in the cavity is given as

$$W = W_e + W_m \ .$$

For the purpose of comparison, the electric stored energy, magnetic stored energy, and the total energy are computed for the short circuited waveguide fields. Figure 8 shows the total energy (computed from both the cavity expansion fields and the shorted waveguide fields) as a function of frequency. As can be seen from the figure, they are in very good agreement. The resonant frequencies for the shorted waveguide (equivalent of a cavity with one side completely removed) are shifted down from the completely enclosed cavity case, and this is as expected from theory. The short circuited waveguide is a very low Q cavity, and from Fig.8 it can be seen that all the Q factors have magnitudes of the order of 10.

B. *Cavity with Walls of Finite Conductivity*

In a cavity enclosed by walls of finite conductivity, the field profile in the cavity is a little different from the case of a cavity made of a perfect conductor, because different cavity modes are coupled through

47

the surface impedance of the cavity walls. In the analysis presented here, it is assumed that the cavity wall conductivity while finite, is still very large. Using this assumption, a perturbation analysis is done to solve the problem.

Writing $\vec{n} \times \vec{E}(\vec{r}, \omega) = \eta(\omega) \vec{H}(\vec{r}, \omega)$ on the conducting portion of the cavity, and defining the Q factors

$$\int_S \vec{H}_\alpha \cdot \vec{H}_\beta ds = \frac{1}{\delta^{\alpha\beta} Q_{o_{hh}}^{\alpha\beta}} \qquad \int_S \vec{H}_\alpha \cdot \vec{G}_\beta ds = \frac{1}{\delta^{\alpha\beta} Q_{o_{hg}}^{\alpha\beta}}$$

$$\int_S \vec{G}_\alpha \cdot \vec{H}_\beta ds = \frac{1}{\delta^{\alpha\beta} Q_{o_{gh}}^{\alpha\beta}} \qquad \int_S \vec{G}_\alpha \cdot \vec{G}_\beta ds = \frac{1}{\delta^{\alpha\beta} Q_{o_{gg}}^{\alpha\beta}}$$

where δ is the skin-depth of the conducting walls given by

$$\delta = \sqrt{\frac{2}{\omega^{\alpha\beta} \mu \sigma}} \quad \text{and} \quad \omega^{\alpha\beta} = \sqrt{\omega_\alpha \omega_\beta}.$$

The subscript "o" indicates an Ohmic-Quality factor. Thus we have

$$f_\alpha = \sum_\varphi \left(\frac{-\eta(\omega) k_\alpha}{k_\alpha^2 - \frac{\omega^2}{c^2}} \right) \left(\frac{j\omega\varepsilon}{k_\varphi} \right) \left(\frac{1}{Q_{o_{hh}}^{\alpha\varphi} \delta^{\alpha\varphi}} \right) f_\varphi +$$

$$\sum_s \left\{ \frac{jk_\alpha \gamma_{\alpha s}}{k_\alpha^2 - \frac{\omega^2}{c^2}} + \sum_\varphi \left[\left(\frac{-\eta k_\alpha}{k_\alpha^2 - \frac{\omega^2}{c^2}} \right) \frac{\beta_{\varphi s}}{\omega\mu Q_{o_{hg}}^{\alpha\varphi} \delta^{\alpha\varphi}} + \sum_\lambda \left(\frac{-\eta k_\alpha}{k_\alpha^2 - \frac{\omega^2}{c^2}} \right) \left(\frac{-\eta\beta_{\lambda s}}{j\omega\mu Q_{o_{hg}}^{\alpha\varphi} \delta^{\alpha\varphi} \omega\mu} \right) \right] \right\} v_s.$$

Using matrix notation, we can write

$$(f) = (A)(f) + (B)(v).$$

In the above expression, all the terms that have a $\frac{1}{Q}$ dependence are deemed to be 1st order terms (since $\frac{1}{Q} \ll 1$) and terms with $\frac{1}{Q^2}$ dependence are the second order terms and so on; otherwise they are of zeroth order (~ 1). Similarly,

48

$$i_r = \int_{S'} \vec{H} \cdot \vec{G}_{tr} ds = \sum_{\varphi} \left\{ j\gamma_{\varphi r} \frac{\omega}{\omega_{\varphi}} + \sum_{\alpha} \left[(j\beta_{\alpha r}) \left(\frac{\eta}{j\omega\mu} \right) \left(\frac{\omega}{\omega_{\varphi}} \frac{1}{Q_{ohg}^{\alpha\varphi} \delta\alpha\varphi} \right) \right] \right\} f_{\varphi} +$$

$$\sum_{s} \left\{ \sum_{\alpha} \frac{\beta_{\alpha s}}{\omega\mu} (-j\beta_{\alpha r}) + \sum_{\alpha} \sum_{\varphi} (j\beta_{\alpha r}) \left(\frac{\eta}{j\omega\mu} \right) \left(\frac{1}{Q_{ogg}^{\alpha\varphi} \delta\alpha\varphi} \right) \left(\frac{\beta_{\alpha s}}{\omega\mu} \right) \right\} v_s.$$

Using matrix notation, we can write

$$(i) = (C)(f) + (D)(v)$$

An ordering of the terms is used so that

$$f = f^0 + \delta f, \quad v = v^0 + \delta v, \quad i = i^0 + \delta i,$$
$$A = A^0 + A^1, \quad B = B^0 + B^1, \quad C = C^0 + C^1, \text{ and } \quad D = D^0 + D^1$$

and

$$\frac{\delta f}{f^0} \ll 1, \quad \frac{\delta v}{v^0} \ll 1, \quad \frac{\delta i}{i^0} \ll 1, \text{ etc.}$$

Then we can write

$$\left(f^0 \right) + (\delta f) = \left[\left(A^0 \right) + \left(A^1 \right) \right] \left[\left(f^0 \right) + (\delta f) \right] + \left[\left(B^0 \right) + \left(B^1 \right) \right] \left[\left(v^0 \right) + (\delta v) \right] \qquad (31)$$

and

$$\left(i^0 \right) + (\delta i) = \left[\left(C^0 \right) + \left(C^1 \right) \right] \left[\left(f^0 \right) + (\delta f) \right] + \left[\left(D^0 \right) + \left(D^1 \right) \right] \left[\left(v^0 \right) + (\delta v) \right]. \qquad (32)$$

Thus we have 2 sets of linear equations for the 2 sets of unknown variables (δf) and (δv). All the perturbed coefficient matrices $\left(A^1 \right), \left(B^1 \right), \left(C^1 \right), \left(D^1 \right)$ have terms with a $\frac{1}{Q}$ dependence. (δi) is linearly related to (δv) via eqs.(27) and (28). Equating the zeroth and the first order quantities separately in the above system of equations, the quantities (δv) and (δf) are found in terms of $\left(f^0 \right)$ and $\left(v^0 \right)$. The solution is obtained as

$$(\delta f) = (E_1)\left(f^0 \right) + (E_2)\left(v^0 \right) \text{ and } (\delta v) = (F_1)\left(f^0 \right) + (F_2)\left(v^0 \right).$$

Here (E_1), (E_2), (F_1), and (F_2) are coefficient matrices which are obtained by rearranging eqs.(31) and (32). The full expressions for these terms are sufficiently complicated as to preclude their inclusion in this report.

49

IV. CONCLUSIONS

The correct set of eigenvectors, required in the expansion of any arbitrary electromagnetic fields in a cavity with apertures in its surface, are identified and computed. The oscillator equations that describe the time evolution of the amplitude coefficients of the eigenmodes are derived. Using the geometry of a rectangular cavity fed by a waveguide, these coefficients are computed in the frequency domain. A short circuited waveguide geometry is used to check the results obtained. The theory of a cavity enclosed by walls of finite conductivity is investigated. By including the $\vec{J} \cdot \vec{E}$ term on the right hand side of the oscillator equations, the gyrotron cavity problem can also be solved.

REFERENCES

[1] H.Weyl, J.Math. 143, 177 (1913).

[2] J.C.Slater, Microwave Electronics, D.Van Nostrand Company, Inc., New York.

[3] T.Teichmann and E.P.Wigner, "Electromagnetic Field Expansions in Loss-Free Cavities Excited through Holes," J.Appl. Phys.24, pp.262, March, 1953.

[4] S.Bergman and M.Schiffer, Duke Math.J.14, 609 (1947).

[5] O.D.Kellog, Foundations of Potential Theory, J.Springer, Berlin, 1929.

[6] S.Schelkunoff, "On Representation of Electromagnetic Fields in Cavities in Terms of Natural Modes of Oscillation," J.Appl.Phys.26, pp.1231, October, 1955.

[7] F.E.Borgnis and C.H.Papas, "Electromagnetic Waveguides and Resonators," Handbuch der Physik, ed.5.S.Flugge,16, Electric Fields and Waves, Springer-Verlog, Berlin, 1958.

[8] K.Kurokawa, "The Expansion of Electromagnetic Fields in Cavities," IRE Transactions on Microwave Theory and Techniques, pp.178. April, 1958.

FIGURE CAPTIONS

1: Geometry of the waveguide feeding the cavity (dimensions: a=0.01783m, b=0.025m, c=0.00993m, d=0.04m).

2: Geometry of the short circuited waveguide (dimensions: a=0.01783m, b=c=0.00993m, d=0.04m).

3. Normalized aperture admittance as a function of frequency in the shorted waveguide for the TE_{10} mode.

4. Electric field profile along the cavity axis in the short circuited waveguide for the TE_{10} mode (waveguide-cavity aperture at z=0, shorted end at z=0.04m).

5. Expanded view of the electric field profile along the cavity axis in the short circuited waveguide for the TE_{10} mode (waveguide-cavity aperture at z=0, shorted end at z=0.04m).

6. Normalized aperture admittance of the TE_{10} mode as a function of frequency for the cavity depicted in Fig.1.

7. Electric field profile along the cavity axis for the TE_{10} mode in the cavity depicted in Fig.1.

8. Normalized total stored energy in the cavity as a function of frequency for the TE_{10} mode in the shorted waveguide.

52

Figure 1

Figure 2

54

Figure 3

Figure 4

Legend:
- - - - Waveguide Theory
——— Cavity Eigenmode Theory

X-axis: Distance along the Cavity Axis (m)
Y-axis: E$_y$ Amplitude

Figure 5

Legend:
· · · · · Waveguide Theory
——— Cavity Eigenmode Theory

Y-axis: E_y Amplitude (200, 150, 100, 50, 0, -50, -100, -150, -200)

X-axis: Distance along the Cavity Axis (0, 0.002, 0.004, 0.006, 0.008, 0.01)

Figure 6

58

Figure 7

E_y Amplitude

Distance along the Cavity Axis(meters)
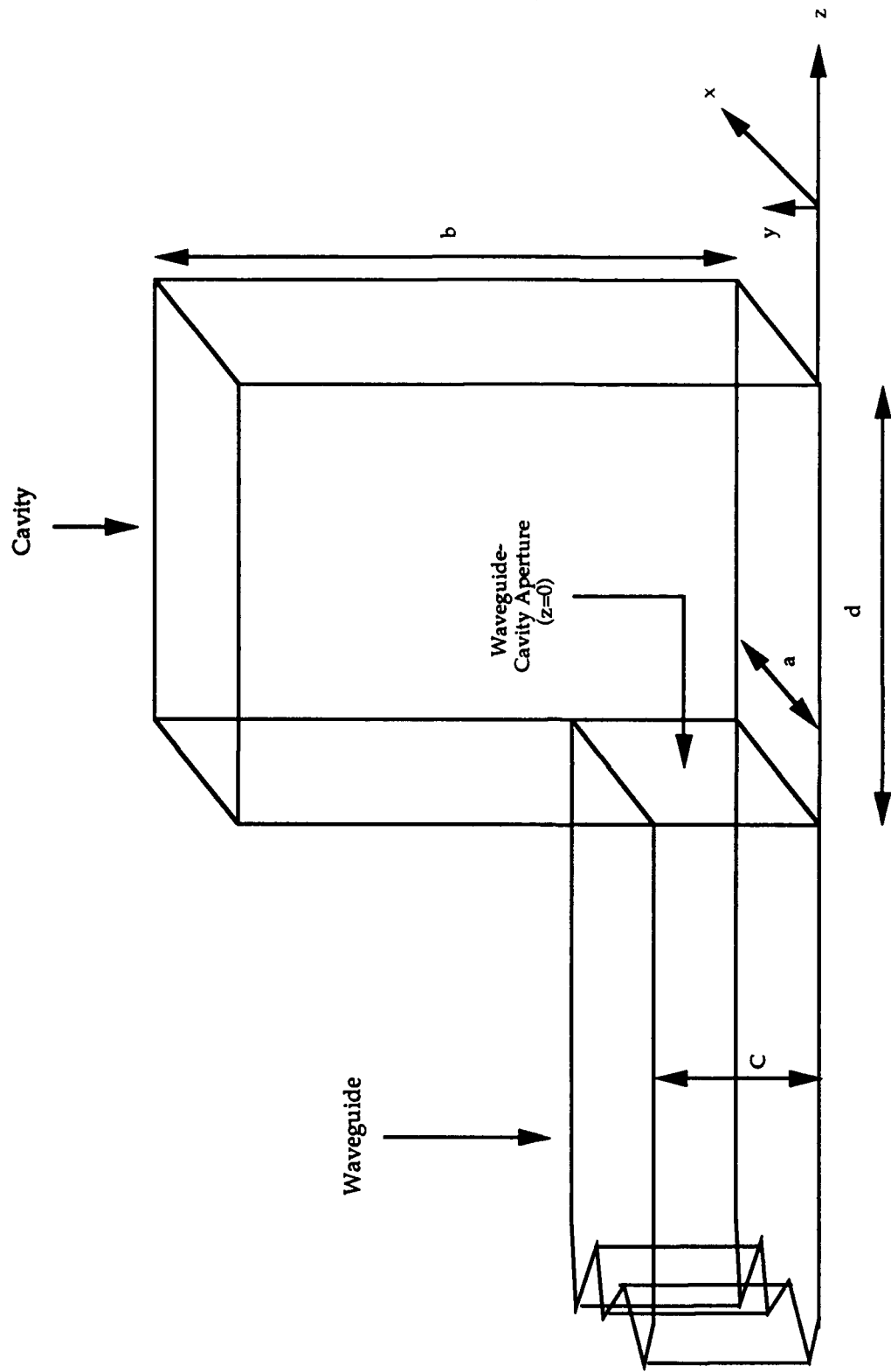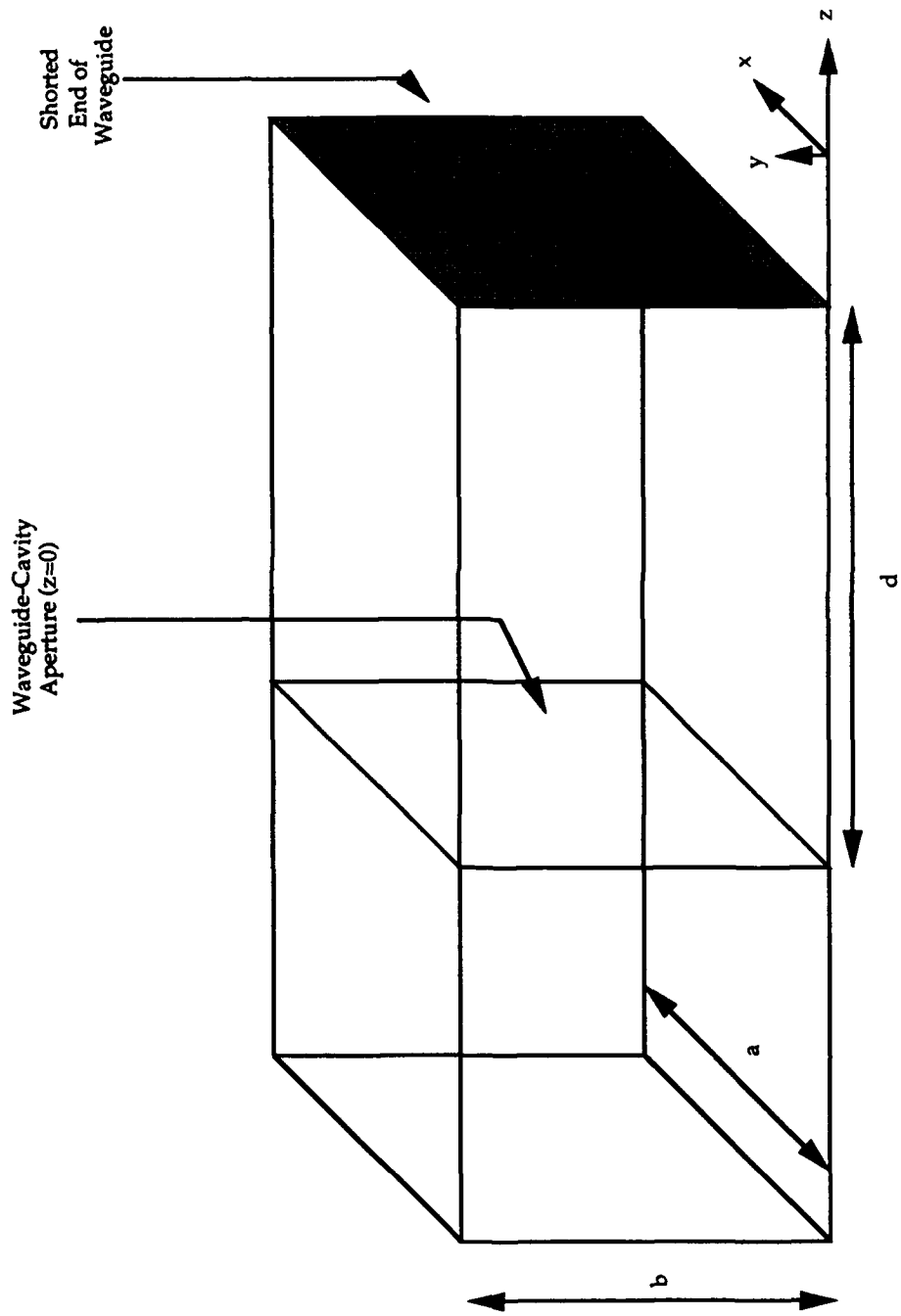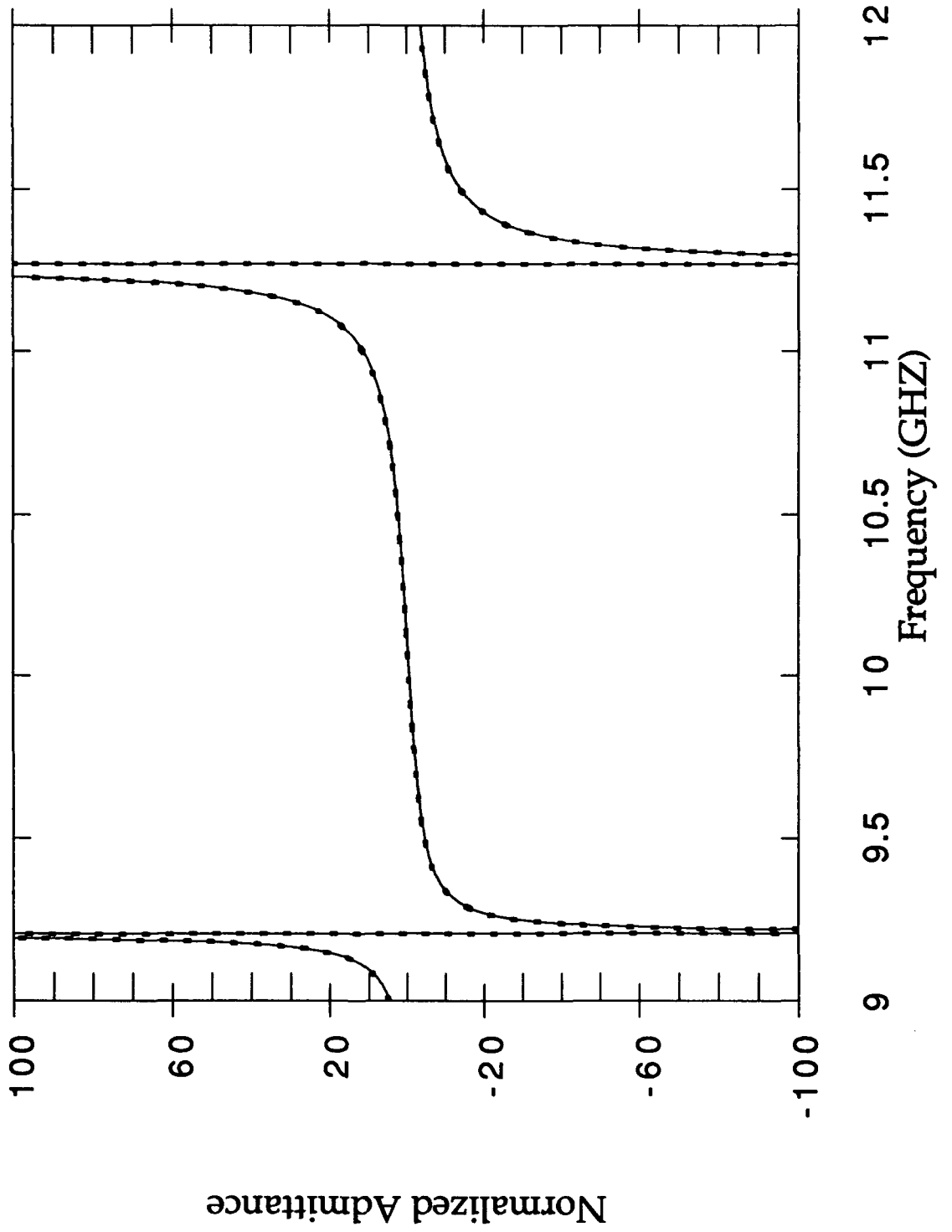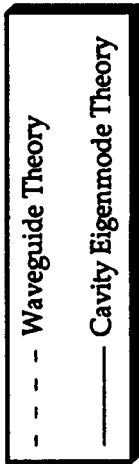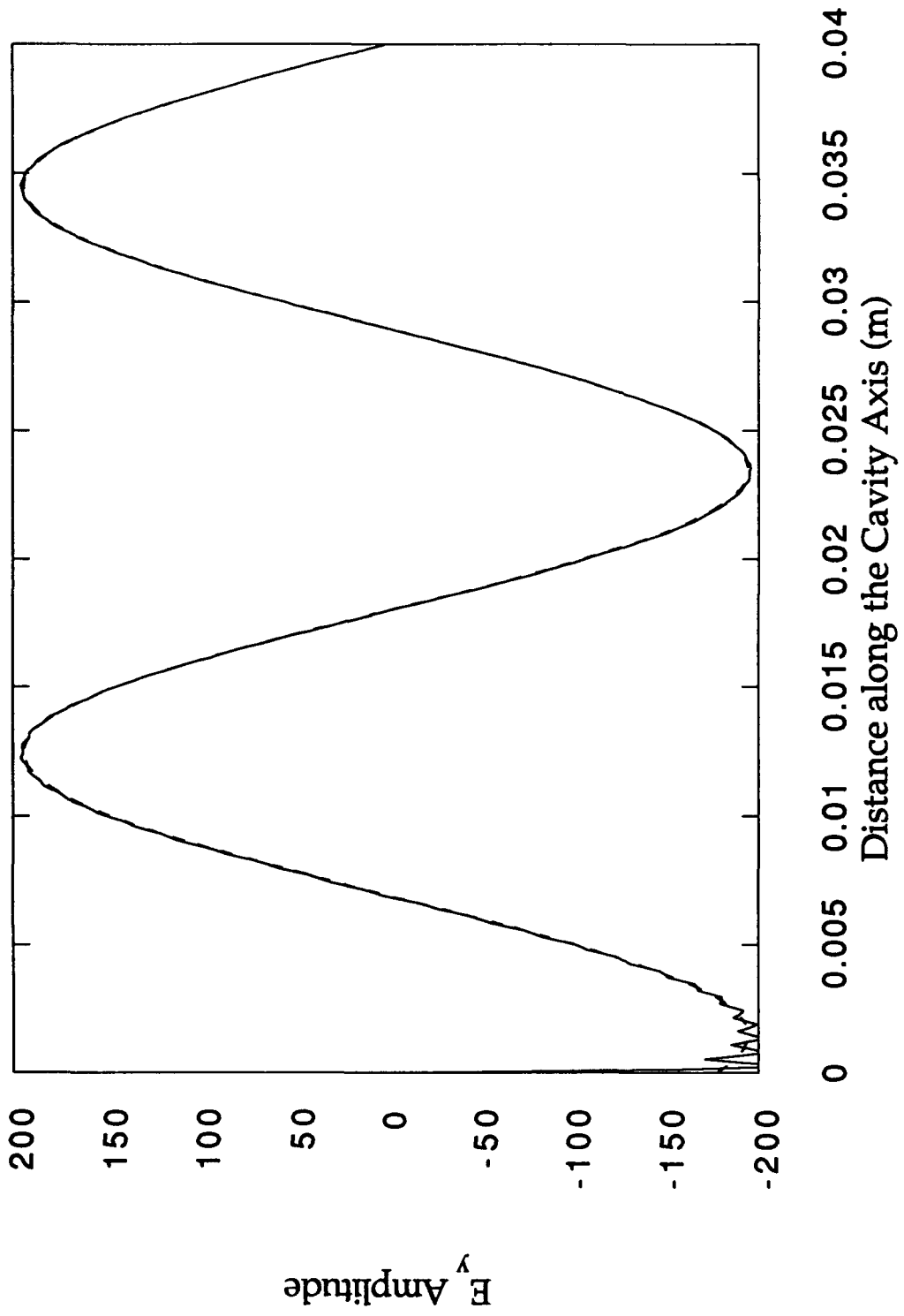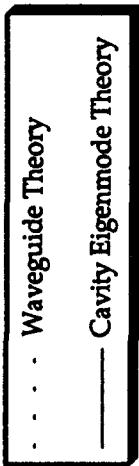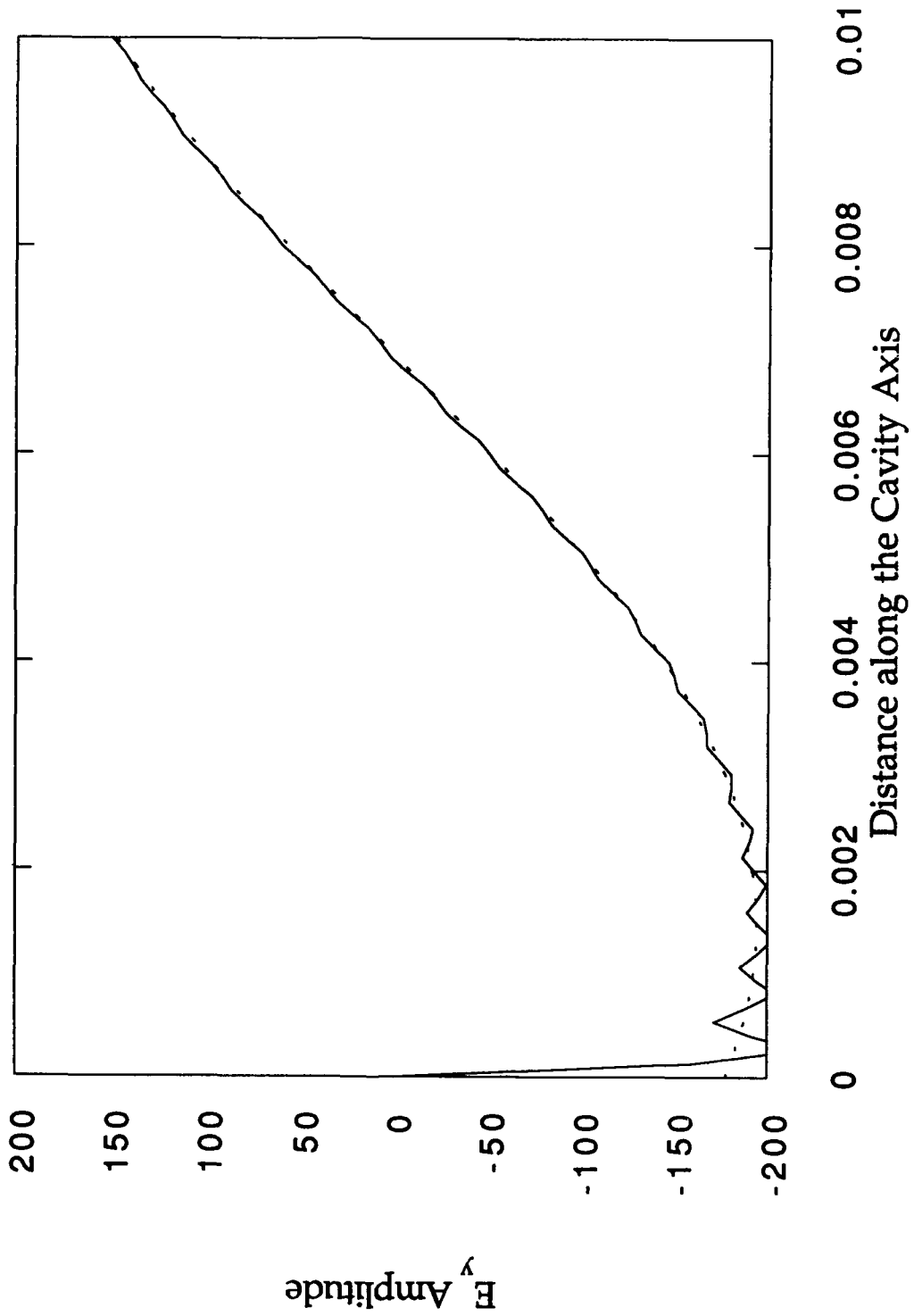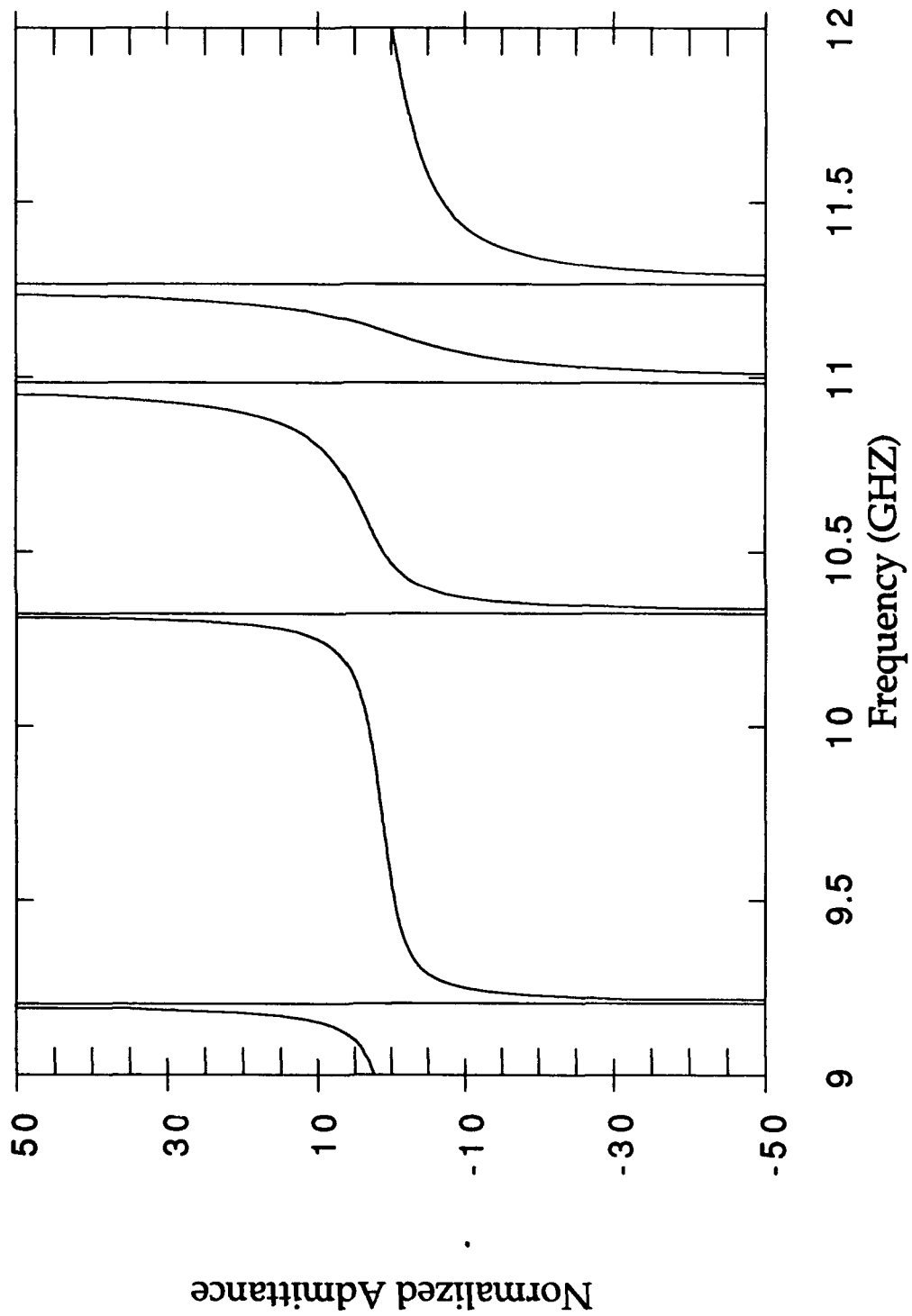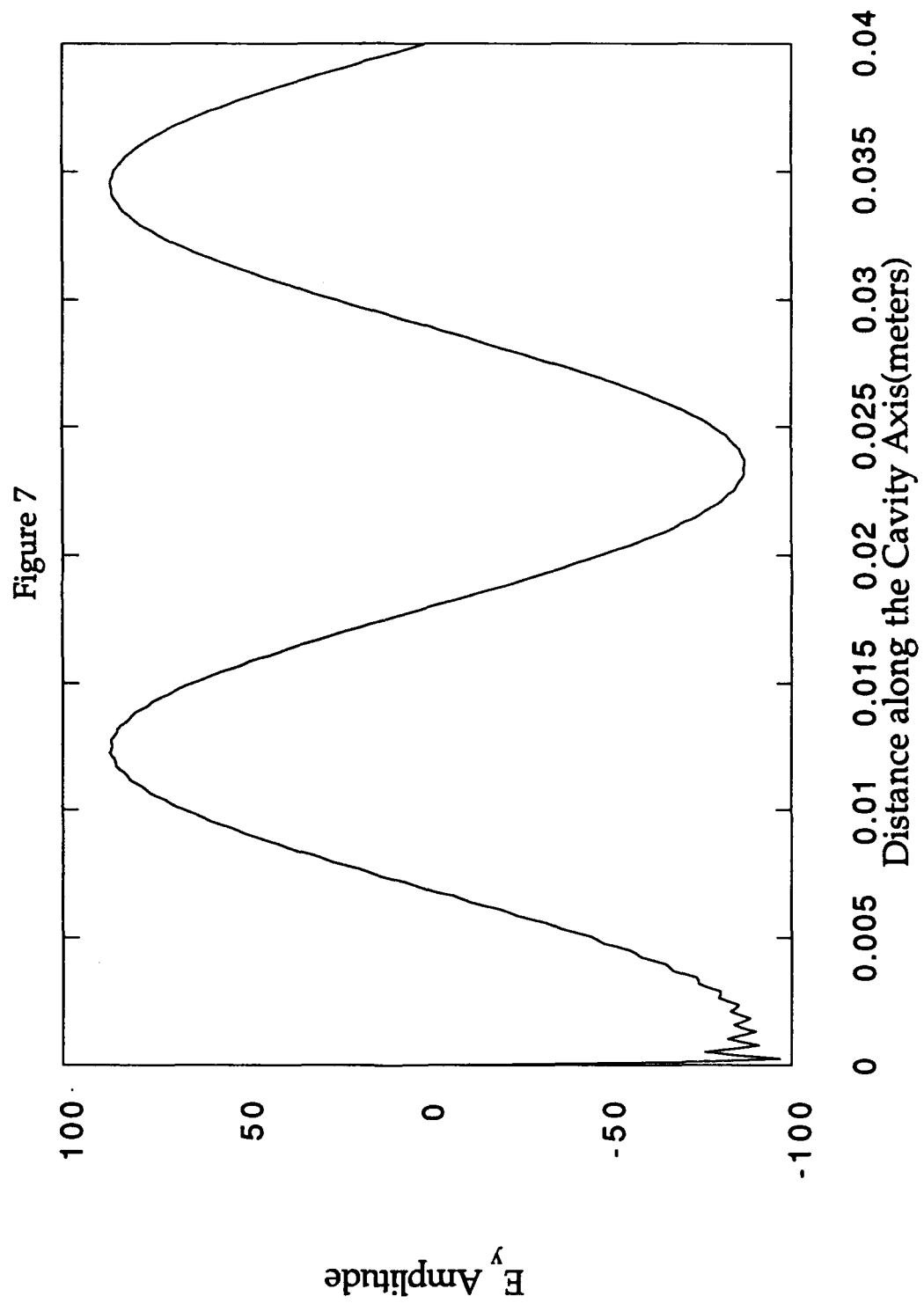
Figure 8
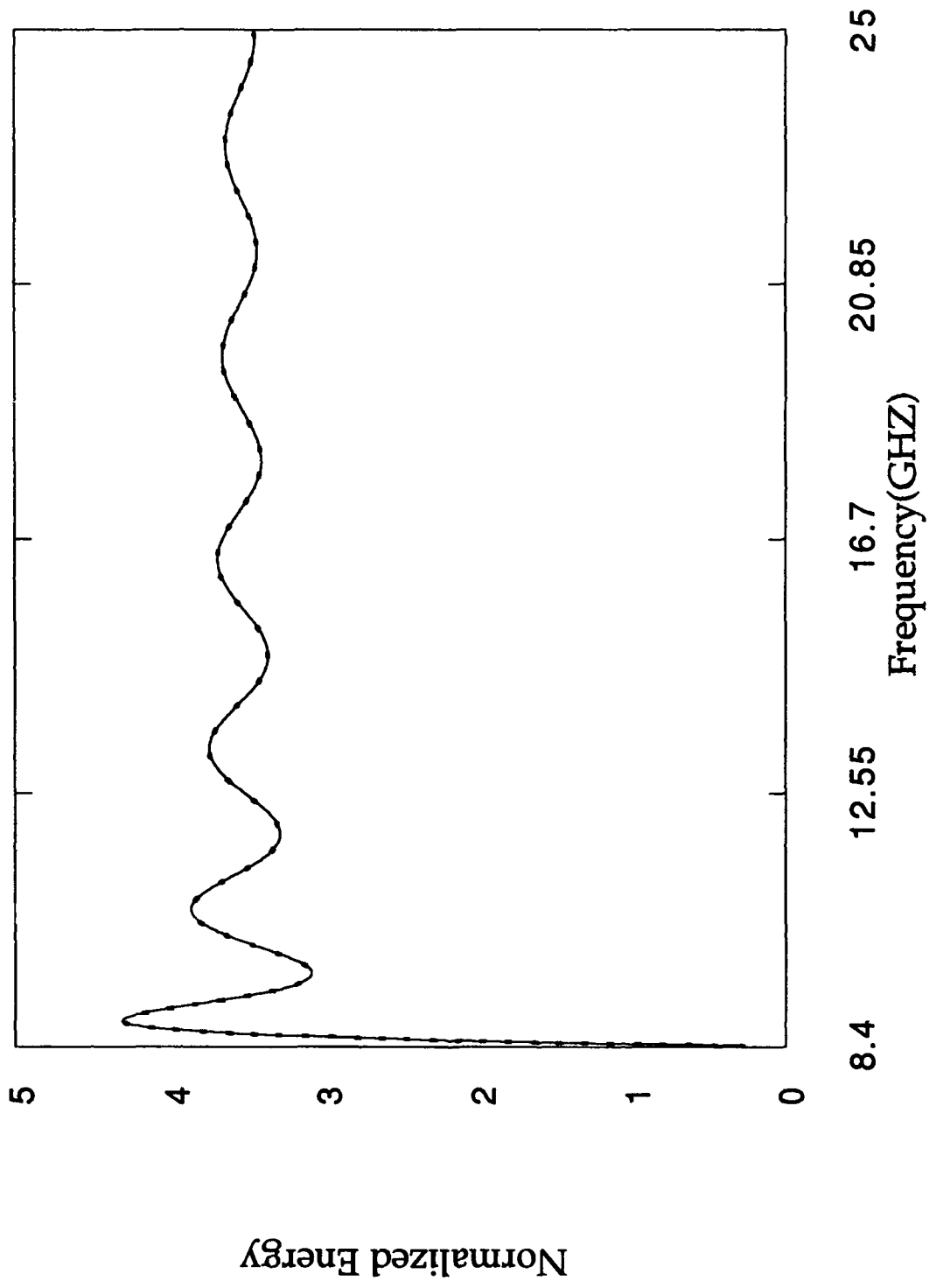
PART III

Experimental Work on a 12 GHz, TE_{101} - TE_{011} Gyrotron Oscillator

Abstract - Part III

Results and discussion are given on the design and test of a two-mode gyrotron oscillator. The predictions of the quasi-linear mode coupling theory for this specific case are given. It is found that the coupling will be quite strong, with the cross-coupling coefficients on the same order as the growth rates. Substantial modal tuning is required to prevent the growth rates of both modes from being identical. In this case only the case $\Gamma=1$ will be tested. (this allows only a restricted regime of predicted phenomena to be examined). The resonator design is outlined and cold test results are given. HFSS simulations of the three dimensional cavity structure and coupling probes are included. It has been found that the coaxial probes can couple very strongly to the cavity (estimated Q on the order of 100-200) without intercepting any electron beam. The design and calibration of beam and rf diagnostics is also described. Electron beam collector design and the design of iron pole pieces for the solenoidal magnet are given. A MAGIC simulation of the propagation of high and low energy gyrating electron beams through the collector region is described. The electron gun trim coil design and POISSON simulations of the trim coil and the main solenoid are given and compared with measurements.

I. INTRODUCTION

The gyrotron quasi-linear theory has been employed to describe the mode competition between two closely spaced modes in a rectangular cavity. A code has been written and growth rates and cross-coupling coefficients can be computed. A summary of results of this investigation are given in Section II. The rectangular cavity and tuning structure have been fabricated and cold tested. The design considerations for this cavity are included in Section III. Results of design and testing of the experimental infrastructure is given in Section IV. This includes the construction of a beam tube (to test beam propagation through the system), electrostatic beam probes, trim coil electromagnet, and electron beam collector. Photographs of these devices are included.

II. RESULTS OF QUASI-LINEAR THEORY

The computation of the linear cross-coupling between rectangular TE_{10q} and TE_{01q} modes has been carried out using the quasi-linear approximation. The rate equations have the form:

$$\dot{P}_j = -\frac{\omega_j P_j}{Q^j_{tot}} + \alpha'_j P_j - \sqrt{P_j P_k}\left(\alpha'_{j,k}\sin\vartheta - \alpha''_{j,k}\cos\vartheta\right)$$

$$\dot{\psi}_j = \omega^0_j - \omega_j - \frac{1}{2}\frac{\omega_j}{Q^j_0} + \frac{1}{2}\alpha''_j + \frac{1}{2}\sqrt{\frac{P_k}{P_j}}\left(\alpha'_{j,k}\cos\vartheta - \alpha''_{j,k}\sin\vartheta\right) \quad .$$

Here P_j and ψ_j are the power and phase of the jth mode, respectively. Primes denote real parts and double primes denote imaginary parts. The phase angle ϑ is defined

$$\vartheta = \left(\omega_j - \omega_k\right) t + \psi_j - \psi_k \quad .$$

The linear growth rate and frequency pushing α_j are defined

$$\alpha_j = -\frac{1}{\gamma_0}\left[1 - \frac{p^2_{\perp_0}}{(\gamma_0 m c)^2}\right]\frac{8 I_0 e}{\pi^2 m \varepsilon_0 \beta^2_{\perp_0} \omega_j \omega_0}\frac{a}{2 b}\left[1 + J_0\left(\frac{2\pi R_0}{a}\right)\right]\int_{\xi=0}^{L} e^{-i\Delta_j \xi}\alpha_j(\xi) f_q d\xi$$

where:

$$\Delta_j = \frac{2}{\omega_o \beta_{\perp_o}^2} \left(\omega_j - \Omega_o \right) \quad .$$

The coefficients of cross-coupling are defined

$$\alpha_{j,k} = \frac{1}{\gamma_o} \left[1 - \frac{p_{\perp_o}^2}{(\gamma_o m c)^2} \right] \frac{8 I_o e}{\pi^2 m \varepsilon_o \beta_{\perp_o}^2 \omega_j \omega_o} \int_{\xi=0}^{L} e^{-i \Delta_j \xi} \alpha_j(\xi) f_q d\xi$$

$$\times \left[J_o\left(\frac{\pi R_o}{a}\right) J_o\left(\frac{\pi R_o}{b}\right) + 2 \sum_{k=1}^{\infty} J_{2k}\left(\frac{\pi R_o}{a}\right) J_{2k}\left(\frac{\pi R_o}{b}\right) \right]$$

where:

$$\alpha_j(\xi) = \int_{\xi'=0}^{\xi} e^{i \Delta_j \xi'} f_q d\xi' - i \int_{\xi'=0}^{\xi} - \int_{\xi''=0}^{\xi'} e^{i \Delta_j \xi''} f_q d\xi'' d\xi'$$

Figure 1 shows the linear coefficients for the TE_{101} mode of the cavity to be described later. The curves represent α' (solid), α'' (dash), $\alpha'_{101,011}$ (chaindot), and $\alpha''_{101,011}$ (x's). Because the resonant frequencies are so close together, the coefficients for the TE_{011} mode are nearly identical. By adding a mismatch at the cavity output, it is possible to increase the cavity quality factor, (these quality factors are dominated by external loss). This variation of quality factor causes the coefficients to be quite different for the two modes. It is of interest to determine the range of validity of this theory. Hence the experiment will be compared with these results. More accurate nonlinear computations can later be made, and a further comparison with experiment can be done.

III. GYROTRON CAVITY DESIGN AND COLD TEST

A. *Design Considerations*

The design of the two-mode experiment proceeded as follows. Once the cavity modes are fixed, there are two free parameters in our design. These are the beam energy and the radiation frequency. All other design values can be derived from these two. The other quantities of interest are the magnetic field, cavity length, beam axial velocity, beam α, cutoff frequency of waveguide, beam guiding center radius, cutoff frequency of beam tunnel.

First the beam energy is fixed. The hard tube modulator in our lab will generate beams with up to 40 keV of energy. We investigated two different beam energies at radiation frequencies between 12 and 13 GHz. The frequency range is chosen because of the ease of obtaining components and the ease of

63

construction of the cavity. Four equations are used to find the parameters suitable for resonance between the beam wave and electromagnetic field. These are:

$$\omega = \sqrt{\omega^2 + k^2 c^2} \tag{1}$$

$$\omega = \Omega/\gamma + k_z v_z \tag{2}$$

$$\alpha = \frac{1.5 \sqrt{B/7}}{\sqrt{1 + 1.5^2 (1 - B/7)}} \tag{3}$$

$$v_\perp = c \sqrt{1 - 1/\gamma^2 - \left(\frac{v_z}{c}\right)^2} \tag{4}$$

The first two equations give the dispersion relations for the electromagnetic wave and the beam wave while the third equation (written for the magnetic field B in kG) gives the beam α based on a cathode magnetic field of 350 G, cathode radius of 1.565 cm which produces a beam with α of 1.5. Equation (4) reflects the definition of γ in terms of the electron velocities. Combining eqns. (3) and (4) we obtain a relation between B and v_z. Further requiring that the wave phase and group velocities be matched at the resonance point results in:

$$v_z = \frac{c^2 k_z}{\sqrt{\omega_c^2 + k_z^2 c^2}} \tag{5}$$

Eliminating ω_c from eqns. (1) and (5) we obtain $v_z = c^2 k_z/\omega$. Using this relation to eliminate v_z from our relation between B and v_z, and eliminating k_z from the same relation by using $v_z = c^2 k_z/\omega$ in (1) we arrive at a solution for B:

$$B = \frac{1/\gamma^2}{\frac{r}{\gamma\omega} - 0.0989 (1 - 1/\gamma^2)}$$

where $r = (2\pi) 2.8 \times 10^9$ and B is in kG. Now the other parameters can be found:

$$k_z = \frac{\omega}{c} \sqrt{1 - \frac{Br}{\gamma\omega}} \quad , \quad v_z = \frac{c^2}{\omega} k \quad , \quad \omega = \sqrt{\omega^2 - k^2 c^2}$$

64

and eqn. (4) for $v_\perp$ and $a = v_\perp/v_z$. From this analysis it is found that for high voltages ($\sim$ 30 kV) the cavity length is quite short ($\sim$ 5 cm), the α is low ($\sim$ 0.8), and the beam tunnels are not well cutoff ($f_c \sim$ 16.5 GHz). The requirement of matched phase velocities was relaxed (in order to make the cavity longer) and it was found that competition from other axial modes became a problem. Short cavities have the disadvantage that the start oscillation current can be quite high for a cavity Q of ~500. Thus a lower voltage was used. For a beam voltage of 18 kV and radiation frequency 12 GHz, it was found that $\alpha = 1.4$, cavity length is 8.38 cm, and the beam tunnel cutoff is 19.87 GHz. This case requires a magnetic field at the cathode of 225 G. Figure 2 shows the phase and group velocity matching and the separation from the next higher mode; the TE_{102}.

The machine drawing for the final cavity design is shown in Figure 3 (all dimensions are in inches). The cavity proper is shown at the bottom of the figure, with nominal dimensions of 1.264×1.264 cm. The cavity length is 8.38 cm as described previously. The upper side of the cavity can be moved by a tuning plunger to allow adjustment of the cavity resonant frequency. The plunger is geared to the outside by an anti-backlash worm gear, a worm, and a 0.25" 303 stainless steel shaft which feeds through the magnet pole piece. The gearing is such that movement of the tuning plunger can be controlled to within 0.10 μm. This accuracy is needed since the cavity resonant frequency is a sensitive function of cavity transverse dimensions. The cavity cap is attached via twelve number 6 screws which compress an OFHC rectangular copper gasket of 80 mil crossectional diameter. The tuning mechanism is supported by an aluminum superstructure attached to the outside of the cavity. The rf seal is performed by a 2 mil thick stainless steel wiper which is electron beam welded to the underside of the plunger. This spring makes a sliding electrical contact with the cavity walls. Not shown in this figure are two rf electrical feedthroughs which penetrate about 1 mm into the cavity through the bottom and side walls.

Figure 4 (a) shows the disassembled rectangular cavity and cylindrical beam tunnels. The tunnel diameter is 0.33" to provide good cutoff properties at 12 GHz and to reduce space charge effects in the small diameter electron beam. In order to make the cavity corners as sharp as possible, the cavity was machined in four pieces, and the end walls were brazed to the cavity body. To keep the beam tunnels perpendicular to the cavity axis, brazing was also used when attaching the tunnels. In all cases, a nonmagnetic Silcoro 75 braze material was used. In the assembled cavity, the deviations of electron beam/drift tunnel wall separation are less than 1 mil. The assembled cavity and cold test setup is depicted in Figs. 4(b) and 4(c). The bronze disk on the cavity cap is the worm gear, with the tuning shaft exiting the picture on either side. Microwave power is fed in through the probe in the cavity side wall. The cavity was leak checked and easily obtained pressures of 10^{-7} torr.

B. Cold Test Results

The degree of coupling of coaxial probes into this rectangular cavity was determined via the High Frequency Structure Simulator (HFSS) in collaboration with Code 6840 of the Naval Research Laboratory.

Figure 5 shows the CAD geometry with the rectangular cavity and a cylindrical beam tunnel on each end. Coaxial lines couple to the cavity from adjacent sides. In the figure shown, a signal, near the resonant frequency of 11.80 GHz. The probe loading causes the decrease of the resonant frequency. The center conductor of the coaxial cables penetrates into the cavity a distance .122 cm, which is about one-tenth of the way across the cavity and is flush with the edge of the beam tunnel. The figure shows the electric field intensity in the z-x plane. The darker the color, the weaker the electric field. The signal is supplied through the top coaxial cable. Several features are immediately apparent. First, the field strength in the beam tunnels is very weak. This is because the 11.8 GHz signal is so far below cutoff. Also the field intensity in the coaxial feed is quite weak. Thus the match between the feed and the cavity is good. Finally, from the light color near cavity center, we see a strong field excited in the appropriate mode in the cavity. Cross-coupling between the coaxial feeds was also measured. This is important because it is we want the probes to couple to only one mode. (Experimentally this will be a good means of mode identification). It is found that there is better than 30 dB isolation between the probes (signal launched through one probe and picked up by the other). When a signal of a given polarization is launched through the cutoff tunnel, similar results are obtained.

The cavity has been constructed and a cold test of cavity resonant frequency and Q-factor has been performed. The setup is pictured in Figs. 4(b) and 4(c). Both reflection and transmission measurements were made on the cavity. The resonant frequencies and Q values were found for the lowest order odd modes by reflection measurements. The frequencies were measured using a sweep oscillator and cavity wavemeter. The Q's were calculated using the FWHM of the resonance curves. Only odd modes can be detected since the coupling probe is at the cavity center. The Q values and resonant frequencies are given in the table below. Note that the resonant frequency of the TE_{101} mode,

	Resonant Frequency	Q
TE_{101}	11.810 GHz	408
TE_{011}	12.062 GHz	670
TE_{013}	13.030 GHz	434
TE_{015}	14.871 GHz	708

the one not affected by the tuning plunger, has a resonant frequency which is very close to that calculated by HFSS. The quality factors are quite low, also in agreement with HFSS. By adding a shorted stub in parallel with the input feeds, these Q's can be increased substantially. A transmission measurement, at

66

the resonant frequency of the TE_{011} mode, indicates that there is about 24 dB isolation between the probes (again in reasonable agreement with HFSS). This is adequate to selectively couple the two modes. Finally, the resonances were unaffected by the introduction of metal at the drift tube ends. This indicates that the tubes are well cutoff to the radiation frequencies used in the experiment.

IV. TUBE DESIGN AND EXPERIMENTAL INFRASTRUCTURE

A. *Tube Design*

One of the first experimental components built was a valve/bellows assembly to be attached to the electron gun. This purpose of this assembly is to allow the electron gun to stay under vacuum while changes in the microwave circuit are made. This assembly is sketched in Fig. 6 and a photograph is shown in Fig. 7. The gate valve is straight-through and is sealed by a Viton O-ring. This prevents baking of the valve at high temperature. Good vacuum was obtained by removing the O-ring and baking at high temperature, then back-filling the system with dry nitrogen and quickly replacing the O-ring. The bellows is guided by two control rods and a screw rod is used to expand the bellows against the force of vacuum. The bellows houses a beam tube which can be inserted into the valve when the gate is open. This prevents the electron beam from being exposed to the non uniform internal structure of the gate valve.

The Varian 8063 gun was activated by applying heater power and a small dc voltage across the mod-anode / cathode gap. The power supply was capable of supplying 10 mA of current, hence we could not run the gun to very high voltage (only about 50 -1 00 V dc). The scaling looked acceptable and we expect full current at high voltage operation.

Capacitive probes are used as beam diagnostics in this experiment. The capacitive probe measures directly the electron beam line charge density. With the knowledge of total beam current, the electron axial velocity can be deduced. The important parameter α ($\alpha = \frac{v_\perp}{v_{//}}$) can then be determined by a knowledge of the beam energy. The probe assembly consists of two sets of 50Ω SMA vacuum feedthroughs on a ConFlat flange as depicted in Fig. 8. The feedthroughs are separated by 180° on the circumference. A small metal disc is welded on the tip of each feedthrough center conductor to increase the probe capacitance. The discs are flush with the drift tube inner surface and electrically isolated from the tube. The probe signal is linearly proportional to the electron beam line charge density when operated in a high impedance mode (1 MΩ.) Equation (6) shows the relationship between the probe voltage V_p and the beam line charge density,

$$\lambda = 2\pi c (\frac{b'}{A_p}) V_p \tag{6}$$

where c is the total capacitance of the measurement set-up, b' is the effective drift tube radius and A_p' is the effective probe area. The constant $c(\frac{b'}{A_p})$ can be determined experimentally through the calibration process.

In the calibration set-up, the actual electron beam was replaced by a metal tube with a similar radius as shown in Photograph 7(b). The metal tube was pulsed to a high voltage, V, to send a displacement current to the probes. The relationship between V and V_p can be written as

$$V = \frac{\ln(b/a)}{\varepsilon_o} c(\frac{b'}{A_p}) V_p \qquad (7)$$

where b and a are the radii for the drift tube and the center metal tube. For a given set-up Equation (7) uniquely determines the constant $c(\frac{b'}{A_p})$. This constant then can be used to determine the line charge density through Equation (6). The axial velocity can be determined as $v_{//} = \frac{I}{\lambda}$, where I is the total beam current.

Fig. 9 shows the calibration results with two different cable length; 5 feet and 13.1 feet. One of the probes is found to be slightly misaligned after the fabrication and is believed to be the reason for the difference in probe response. Since different cable lengths represent different total capacitance, the slopes are therefore different. For example for probe #1 with 13.1 feet cable, the constant $c(\frac{b'}{A_p})$ is found to be 7.14×10^{-8}. The following table gives the values for the constant $c(\frac{b'}{A_p})$ with various cable lengths.

	$c(\frac{b'}{A_p})$
Probe #1, 5 feet cable	3.01×10^{-8}
Probe #1, 13.1 feet cable	7.14×10^{-8}
Probe #2, 5 feet cable	3.84×10^{-8}
Probe #2, 13.1 feet cable	9.09×10^{-8}

The design of the electron beam collector was closely guided by the POISSON and MAGIC PIC simulation. Fig. 10 shows the final design of the collector including the magnet polepiece. In order to provide the flexibility to move the collector in the axial direction, a cup-shape polepiece is incorporated. The function of the polepiece is to create an abruptly divergent magnetic field at the entrance of the

68

collector region so that electrons can be diverted toward the collector wall where cooling is provided. The POISSON simulation generates a magnetic field distribution according to the electromagnet manufacturer's specifications and the proposed polepiece design. This simulation result is then transferred to the MAGIC PIC code as the prescribed field for electron trajectory simulation. The resultant electron spatial distribution will then give the information on the efficacy of the overall collector design. The criteria for success is that after passing through the polepiece the electrons will deposit their kinetic energy on the collector body where a proper cooling is provided. The polepiece thickness and the size of the bore hole play an important role in the electrons behavior inside the collector. The iteration between varying the pole piece shape and checking the electron trajectories is continued until a proper design is achieved. Figure 11 shows the simulated electron trajectory with MAGIC PIC code for a polepiece which is 0.8" thick with a bore hole of 1.23" in diameter. . The electrons are observed to be distributed over a broad area on the collector wall (~ 100 cm^2.) The power density can be estimated to be ≈ 4.0 kW/cm^2.

In order to simultaneously achieve high vacuum capability and good mechanical stability, a ceramic ring structure was chosen to provide the necessary electrical isolation of the collector from the tube body. This d.c. break involved brazing alumina rings to 30 mil thick Kovar disks. These disks were in turn electron beam welded to stainless steel flanges. While Kovar was needed to provide a good brazing interface, the mass of the material was minimized. This in turn minimized the possible perturbation of the magnetic field in the collector entrance. The insert in Fig. 10 depicts the actual dimension of the structure.

The collector body was made of 304 stainless steel tube with 3.0" OD and 0.1" wall thickness. Collector cooling is provided with a water jacket consisted of 7-turn 1/4" copper tubes. With a cooling water flow rate of 0.1 gpm, the collector can handle a beam power of 400 W continuously.

B. *Experimental Infrastructure*

The electromagnet (manufactured by Premiere Microwave, Palo Alto, CA) has been tested and the axial magnetic field measured with an F. W. Bell 9900 Gaussmeter and FAA 9900915 probe. The electromagnet was powered with four 30 kW DC power supplies. In the measurement shown in Fig. 13, DC current from each power supply was 80 A which generated a peak magnetic field $\approx$ 3.2 kG. The current was measured with resistive shunts. The magnetic field was measured at a 0.5" axial increment throughout the whole electromagnet and compared with POISSON simulation. Fig. 13 shows both the measurement and the simulation results. It was observed that some discrepancy existed in region at 15" away from one end of the magnet. The variation was about 2% of the peak magnitude. The actual cause is not yet clearly understood. The electromagnet has also been running with 90% power for $\approx$ 5 hours at a cooling water flow rate of 20 gpm No thermal problems were observed.

The main purpose of the trim coil is that in conjunction with the 7 kG solenoid, it produce the desired field profile near the electron gun cathode. Specifically, for the gun that is being used in this experiment, it has been determined that axial magnetic field at the cathode has to be in the range 325-375 Gauss, and that the field be relatively constant over the surface of the cathode. Other issues in this design are that the B field has to increase from its value of ~350 Gauss at the cathode to a value of about 1 kG in a distance of 1.5" toward the solenoid. This requirement comes about because the gun beam channel is approximately 1.5" away from the cathode center, and has a radius of about 0.05". The design was achieved by using the POISSON code. Figure 14 shows the output from the POISSON simulation. The trim coil is run at 20000 Ampere-turns, and its right edge is 5" away from the left edge of the solenoid. The solenoid is run at 177 amps, to produce a axial B field of 7 KG. There is a 1.6" pole piece at the edge of the solenoid, and the trim coil is surrounded on both sides by iron plates of 0.25" thickness, and with an inner radius of 3.2" and outer radius of 9.5". The fields are me. ꞏ .ed at 0.225" off the axis, since the center of the emitting surface of the cathode is also 0.225" off the axis. As seen from Fig. 14, a relatively flat field of about 350 Gauss is obtained at a distance of about 2.5 inches away from the left edge of the solenoid with this set-up.

The trim coil (Applied Magnetic Products, Oakland, CA) has been fabricated and delivered. The coil consists of 5 pancake sections of electromagnets. A copper sheet provides heat conduction from the center of each section toward the edge where it is then was removed by cooling tubes. The trim coil is 5" long with a center bore of 7". It is powered with an EMI DC power supply. Figure 15 shows the comparison between measurement and POISSON simulation. The result indicates that the measurement and simulation are in good agreement. A trim coil support which is capable of XYZ motion and adjustment has been designed and manufactured. In principle the structure is capable of supporting a weight of 1000 lbs.

Figure 16 shows a sketch of the laboratory setup. The lab features desk space with two MacIntosh computers and an IBM 486 (to run EGUN and MAGIC). A chemical fume hood allows preparation of materials for a high vacuum environment. The high voltage modulator, equipment racks, and d.c. power supplies are all labeled. The magnets rest on the aluminum optical bench.

FIGURE CAPTIONS

1: Linear coefficients for the TE_{101} mode . The curves represent α' (solid), α'' (dash), $\alpha'_{101,011}$ (chaindot), and $\alpha''_{101,011}$ (x's).

2: Phase and group velocity matching and separation of TE_{101} mode from the next higher mode; the TE_{102}.

3: Machine drawing for the final cavity design.

4: Photographs of rectangular cavity and cold test setup. (a) disassembled cavity, (b) and (c) views of cold test.

5: HFSS analysis of electric field excitation at 11.8 GHz in cavity. Standing wave is seen in the feed line and evanscent waves are present in beam tunnels.

6: Sectional drawing of the electron gun and valve/bellows assembly.

7: Tube components (a) electron gun and valve/bellows assembly, (b) calibration setup for capacitive probes, (c) electron beam collector with water cooling coil.

8: Geometry of the capacitive probes (a) detail on vacuum feedthrough and dimensions of probe tip, (b) mounting configuration for probes on ConFlat flange.

9: Capacitive probe response for cable lengths of 5 ft. and 13.1 ft. as a function of voltage applied to center conductor.

10: Machine drawing for electron beam collector and pole piece.

11: MAGIC simulation of 10 keV electron beam trajectories into the collector region.

12: General layout of magnets and experiment (a) solenoidal magnet and high voltage modulator, (b) solenoidal magnet with electron gun and Lucite gun case in foreground (c) trim coil electromagnet and power supply with solenoid power supplies in background.

13: Magnetic field measurement compared to POISSON simulation with 80 A in coils of main solenoid.

14: Superposition of trim coil field and solenoid field with flat region at cathode position.

15: Magnetic field measurement compared to POISSON simulation for 12 A in trim coil.

16: Layout of laboratory.

FIGURE 1

Magnetic Field (kG)

Coefficient

FIGURE 2

frequency (GHz)

wavenumber, kz

TE_{101} .375

TE_{102} .750
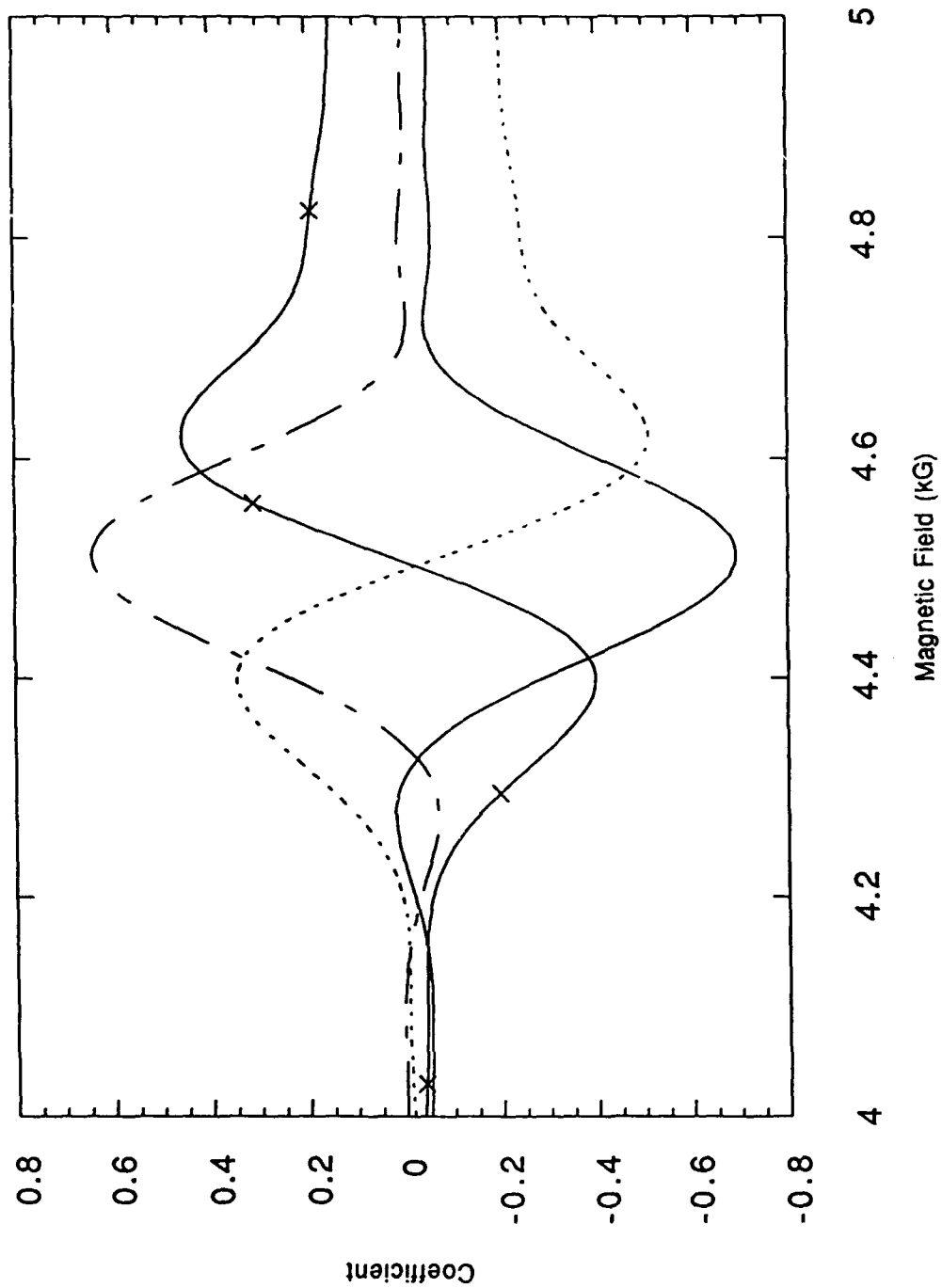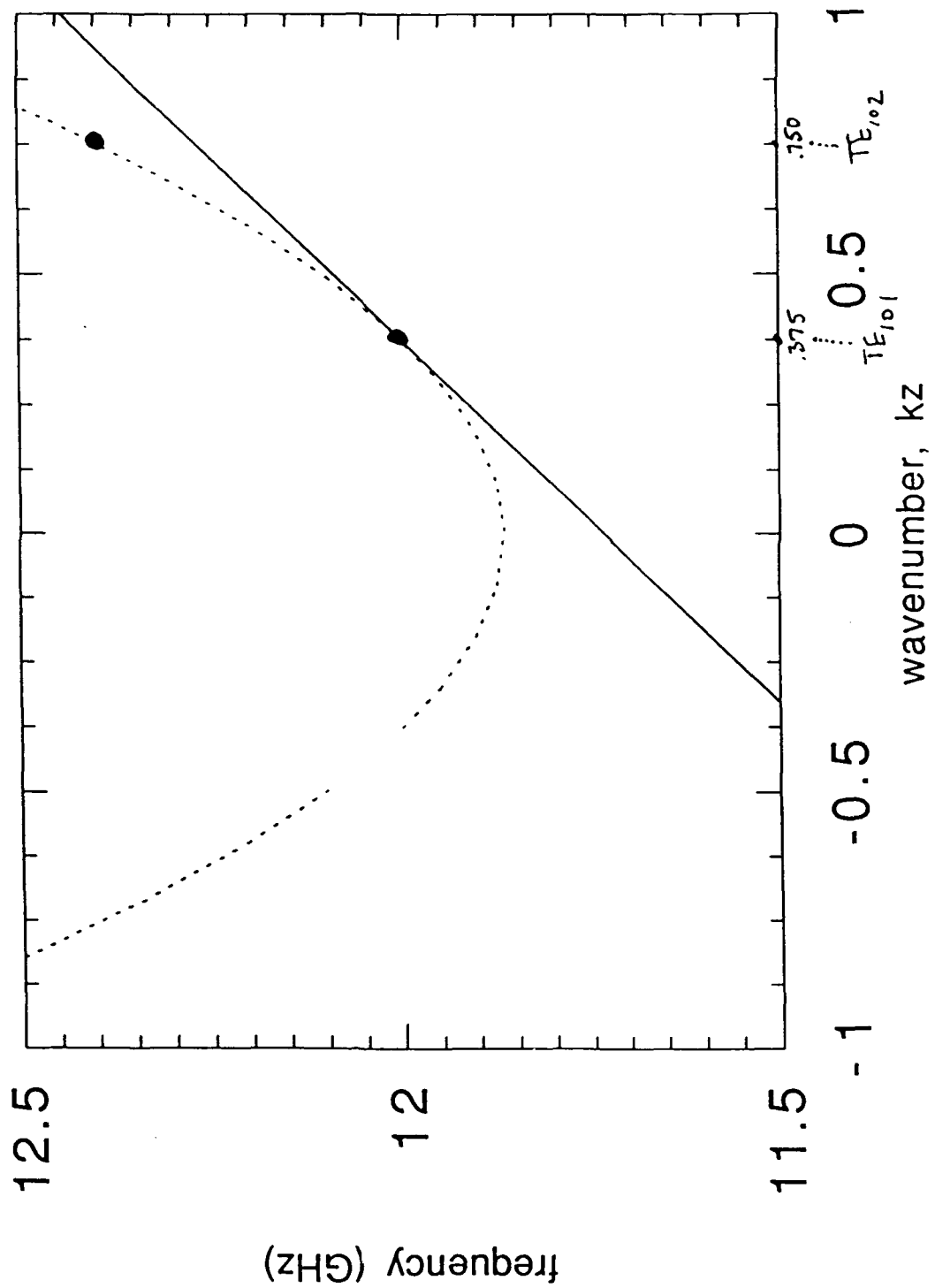
Cavity/Tuner - cross section
(at center)
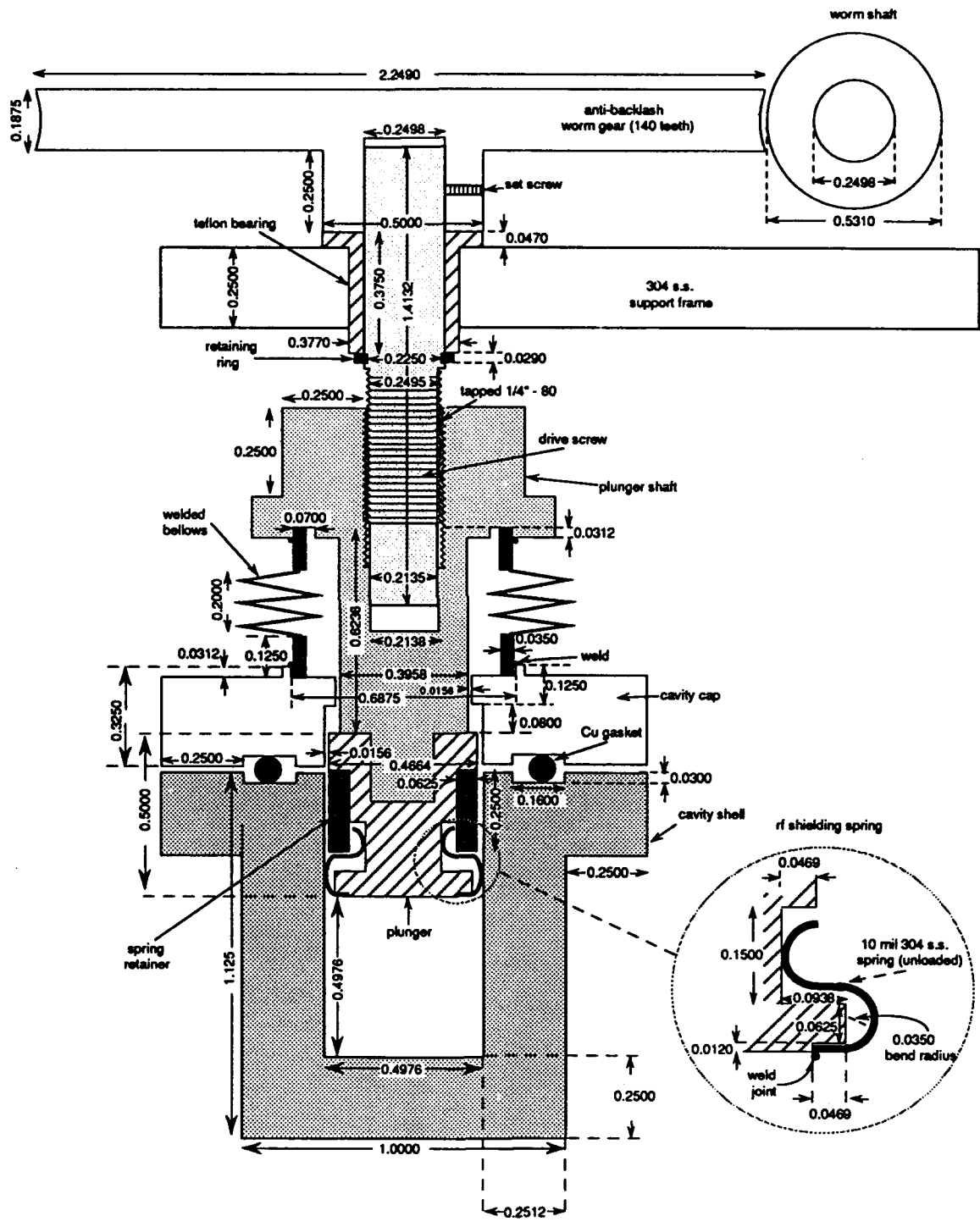
FIG·3

74
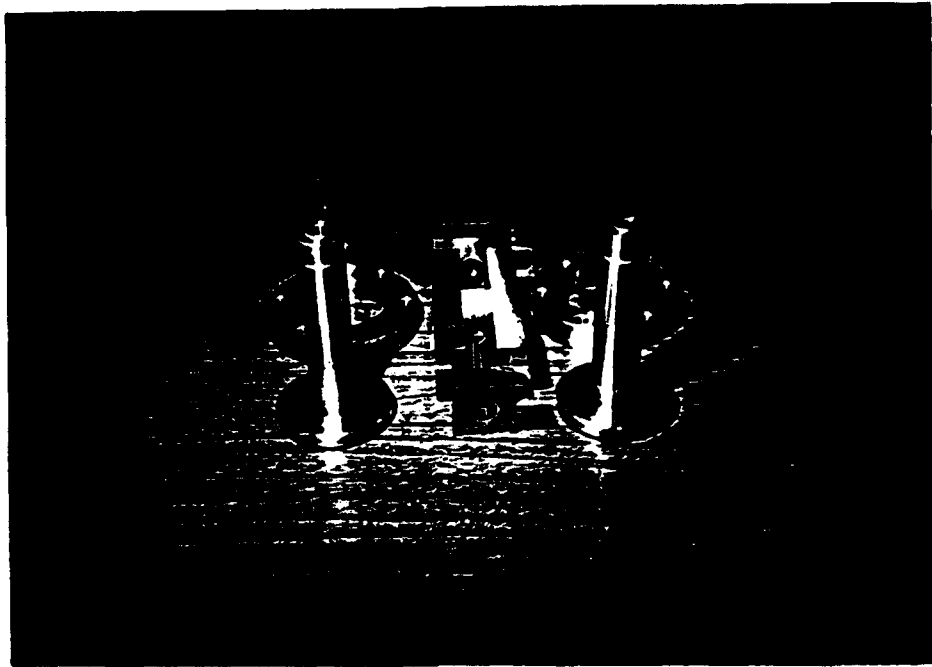
(a)
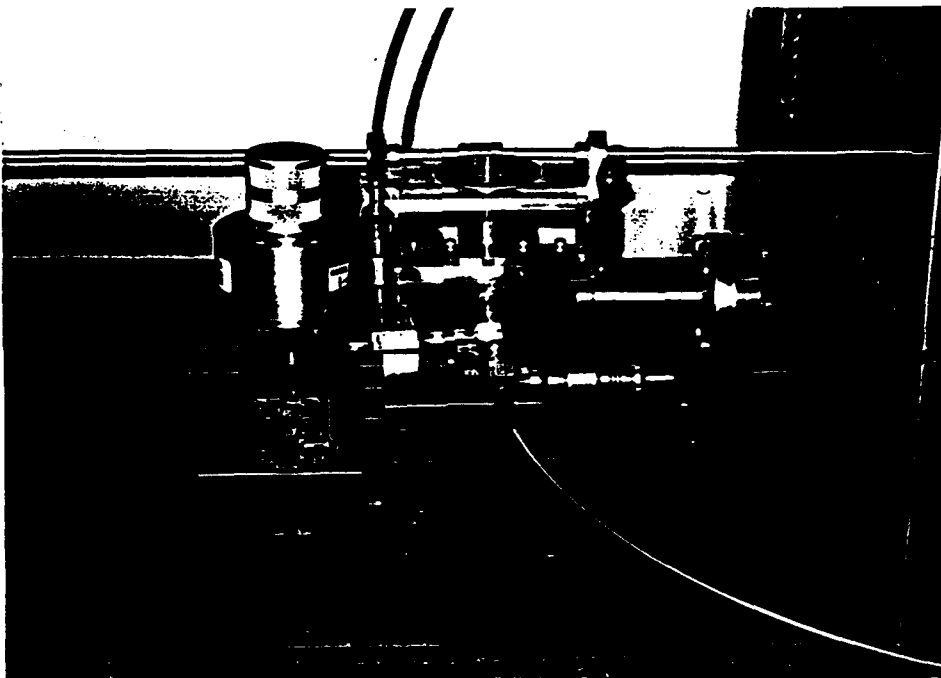
(b)
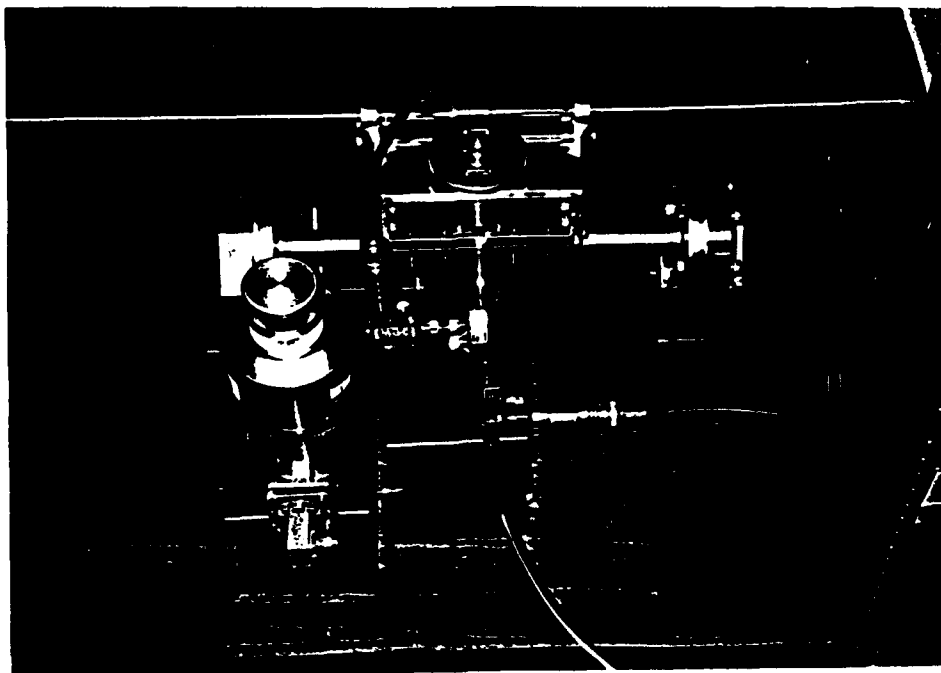
(c)

FIG. 4

Two mode experiment

FIG. 5

FIG. 6

FIG. 7

Figs. 8

.230
diameter
tip

.103
diameter
shaft

Top View

.02

.103

.718

.04

.230

.375

79
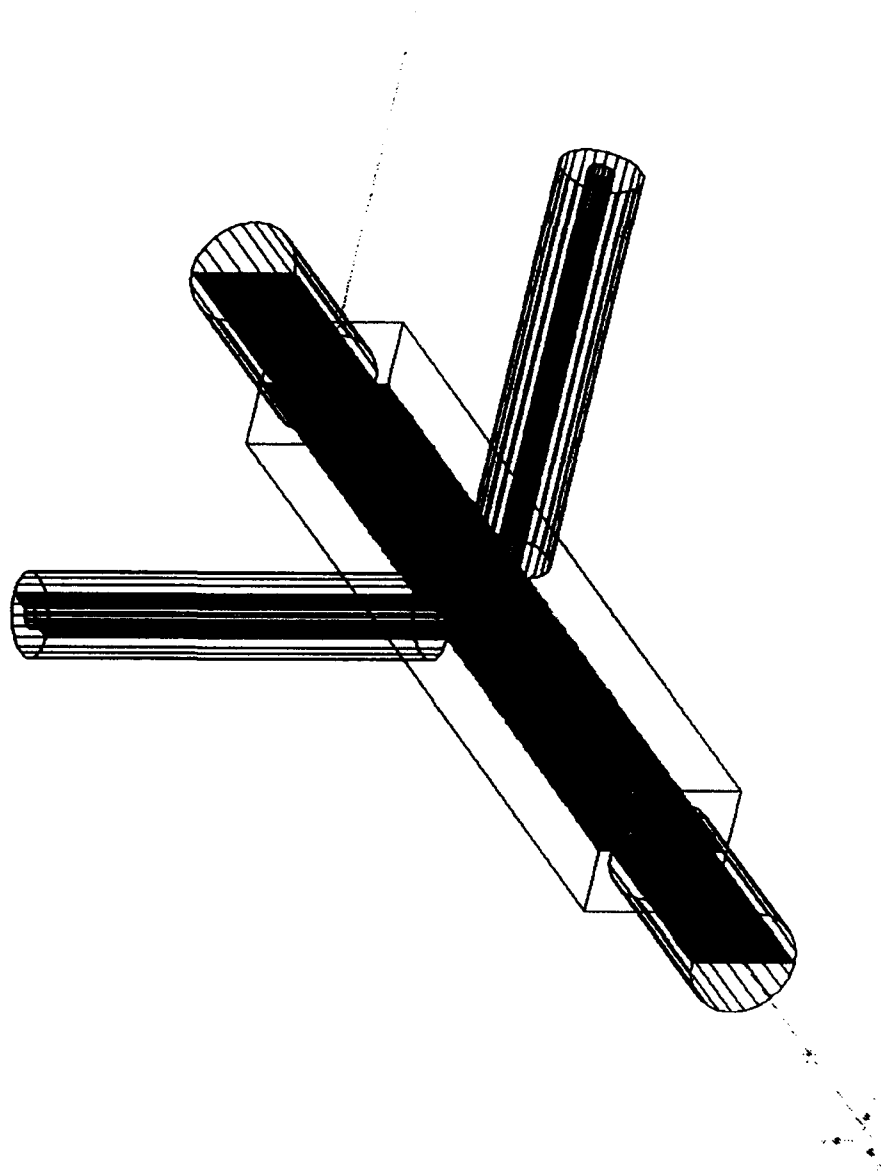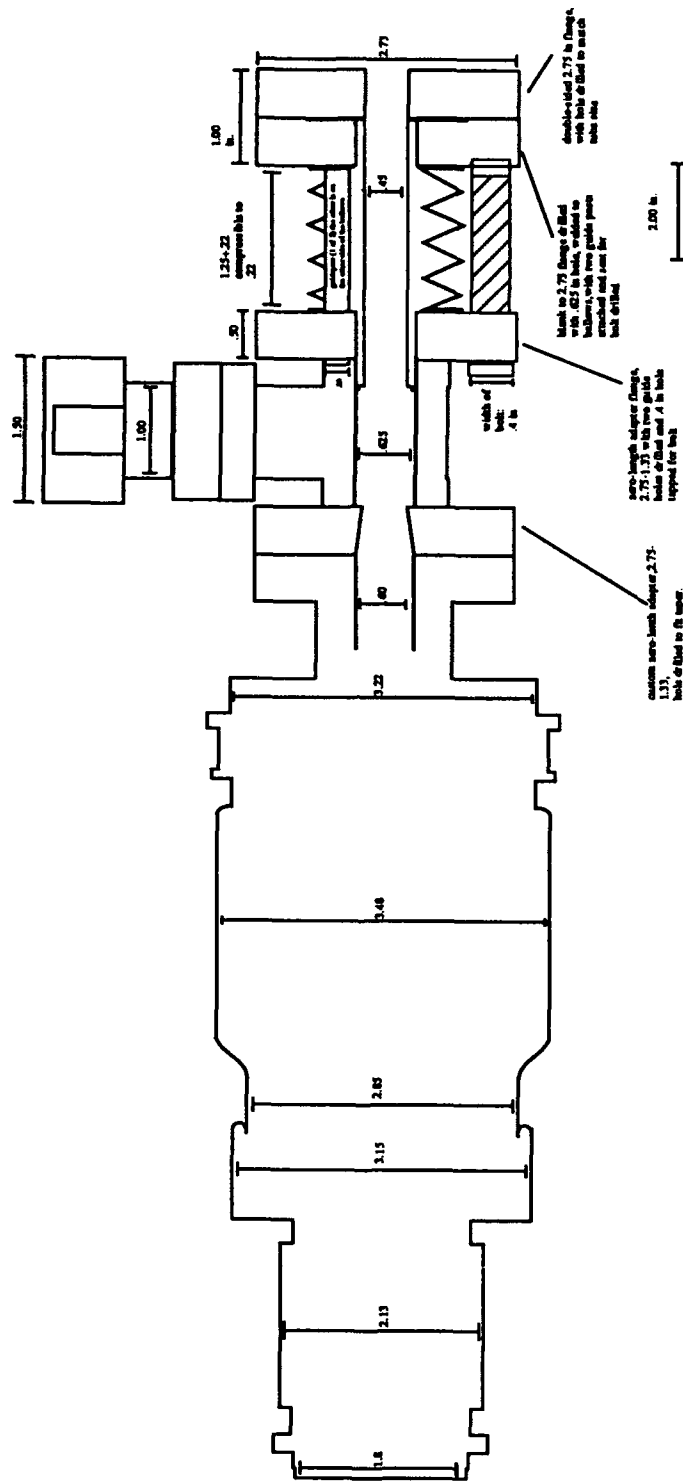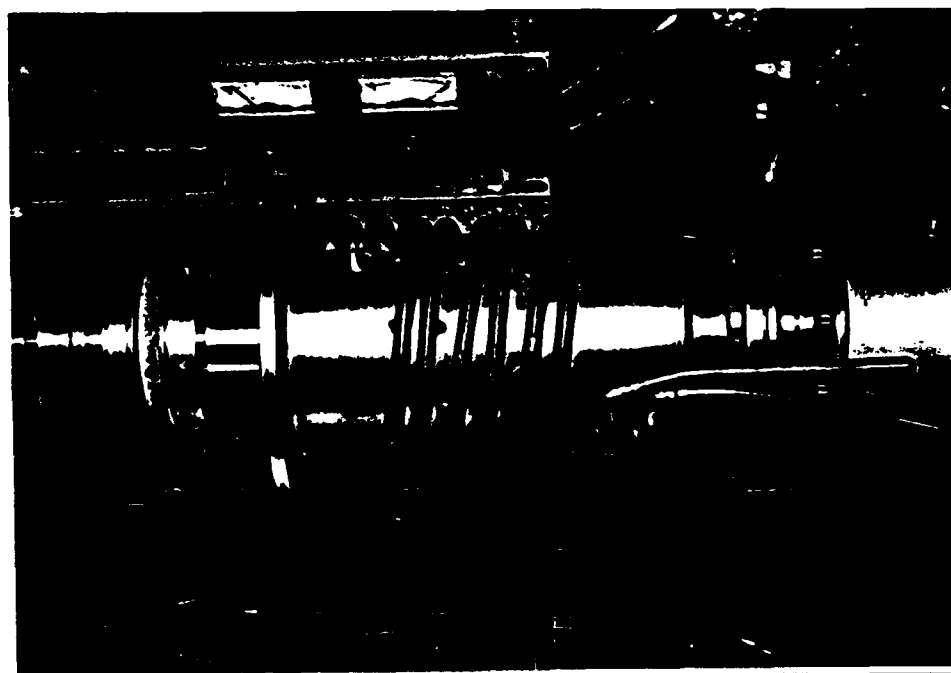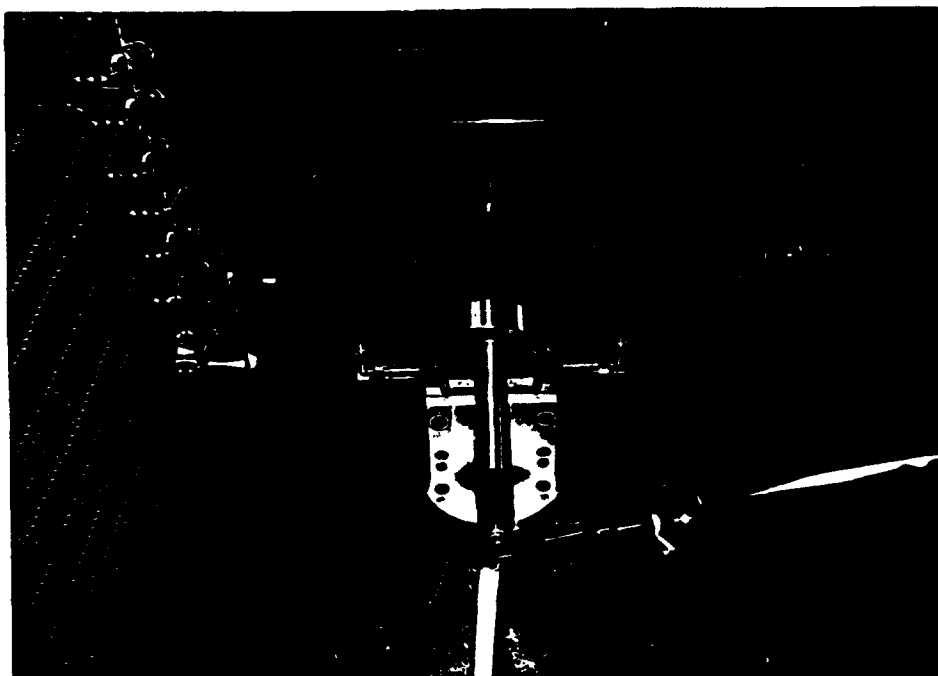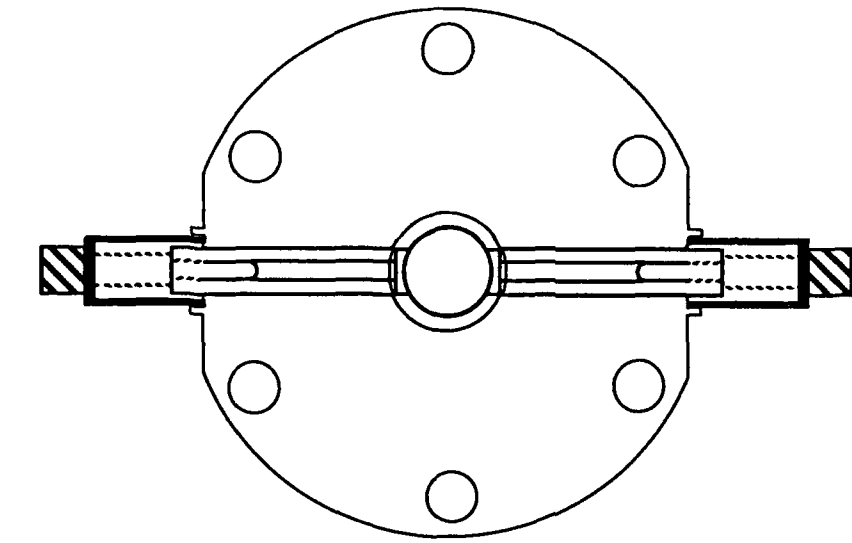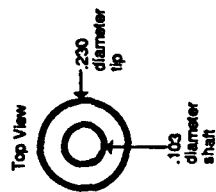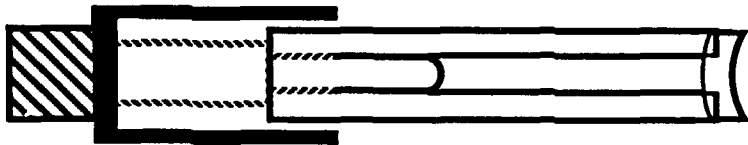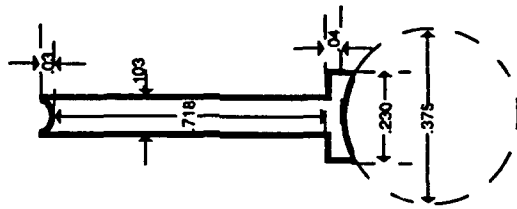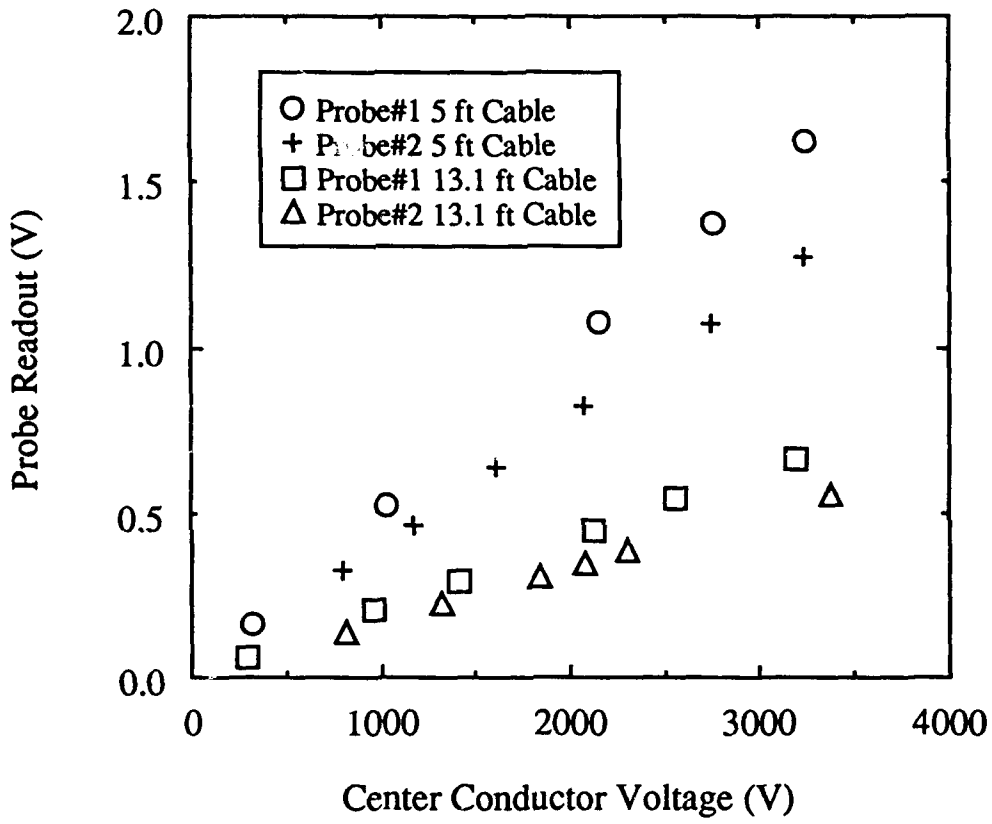
FIG.9

ELECTRON BEAM COLLECTOR
(Including polepiece and support)

FIG. 10

3.00 OD
(Wall thickness=0.12)

0.125

1.37

5.125

SS Half Nipple

8.000
1.50
5.00
4.84
4.17
0.25
1.453
1.00
1.125
0.650
1.500
0.50
1.822
0.35
1.625
2.125
2.75

Insulating Ring

1/32 Clearance

30 mil Kovar Discs

: 304 Stainless Steel
: 1020 Steel
: Ceramic Rings
& : Tig Welding

0.35
1.625
2.125
2.75
30 mil Kovar Discs
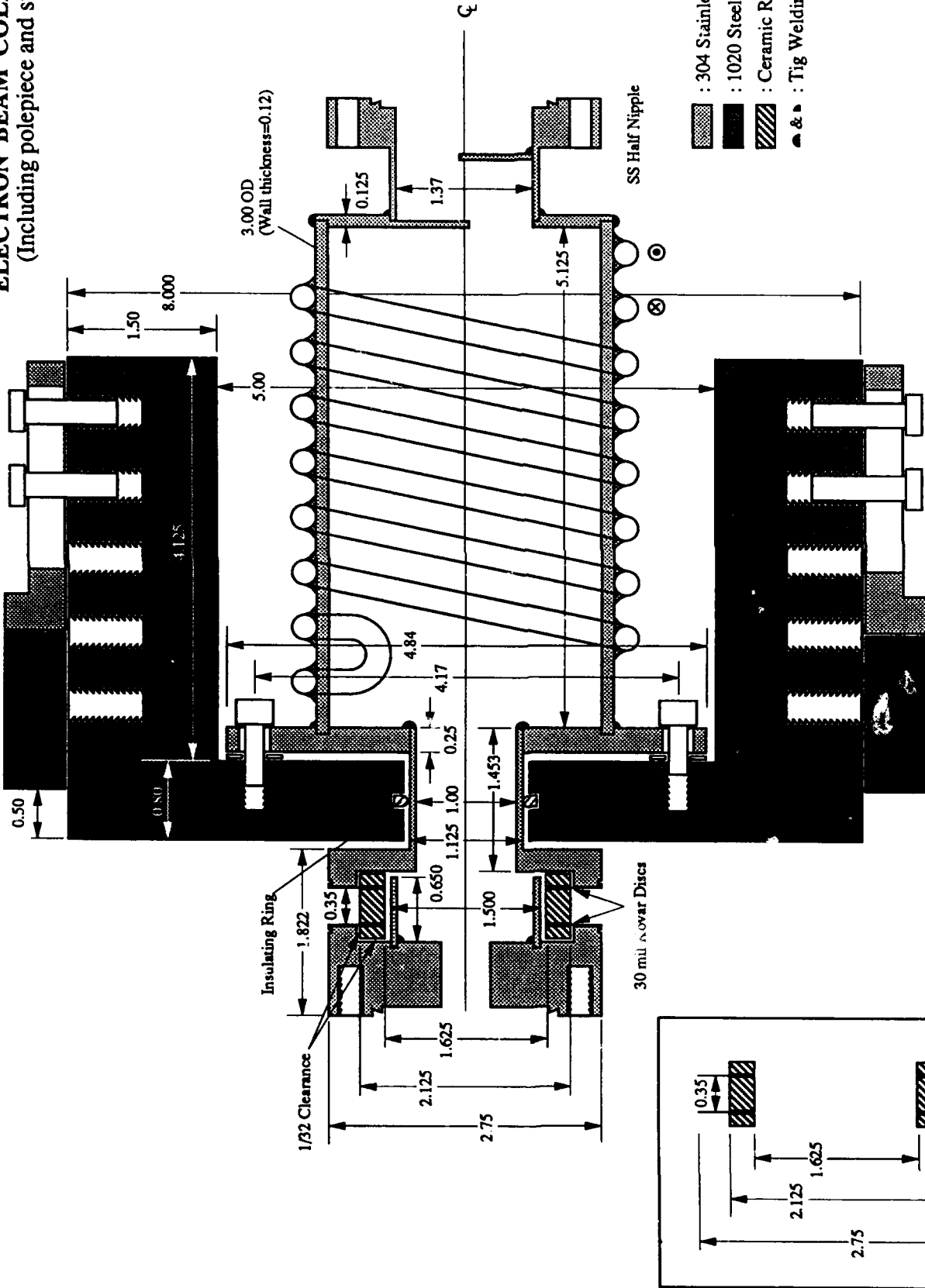
MAGIC VERSION: DATE: 1/28/1994
SIMULATION: CLCTR.MGC

TRAJECTORY PLOT OF ELECTRON
FROM TIME 9.373E-09 SEC TO 9.385E-09 SEC

FIG. 11

FIG. 62

FIG. 13

84
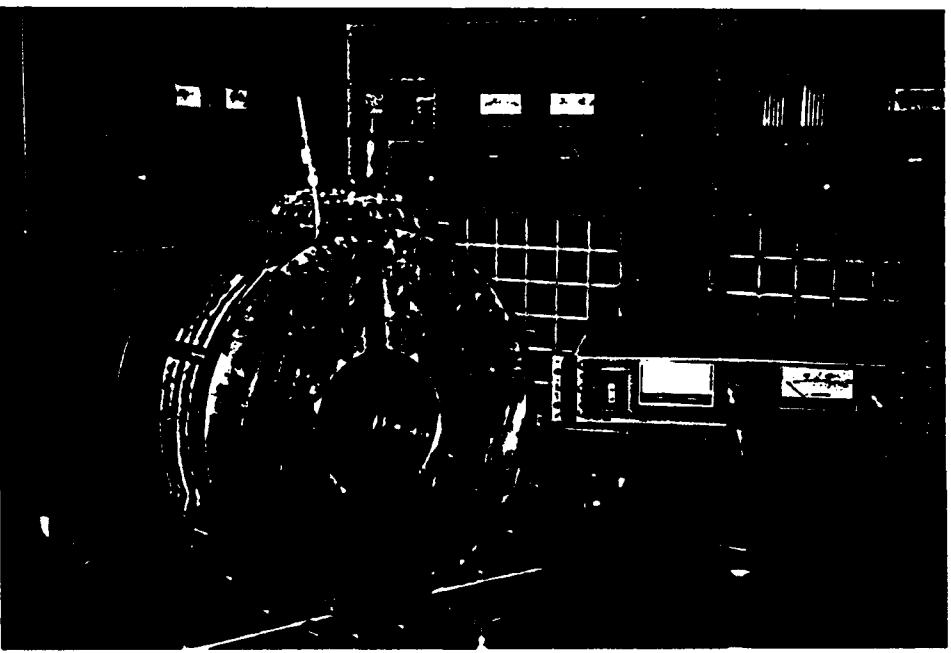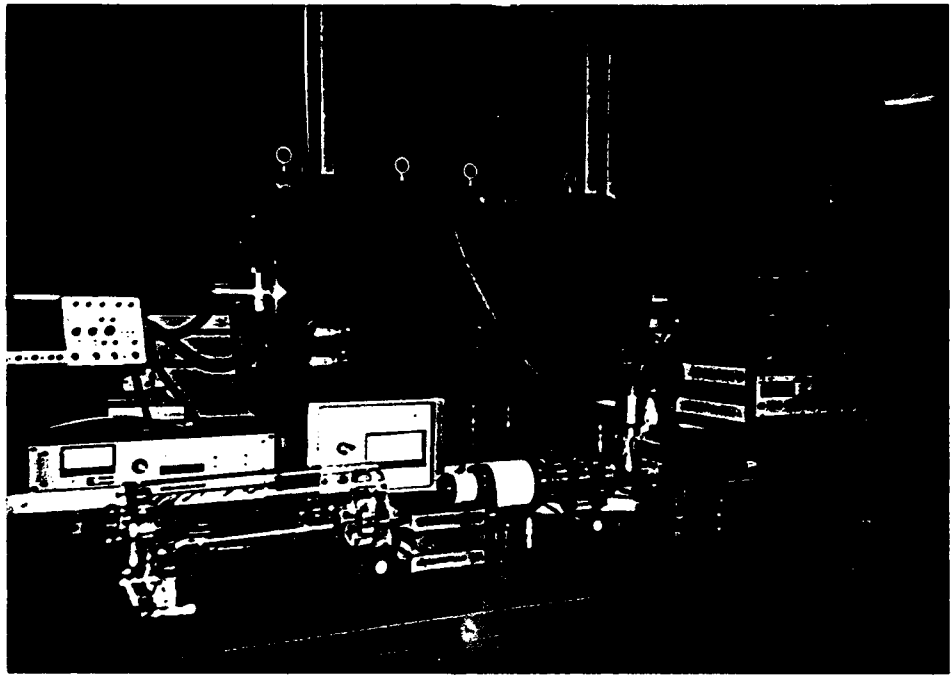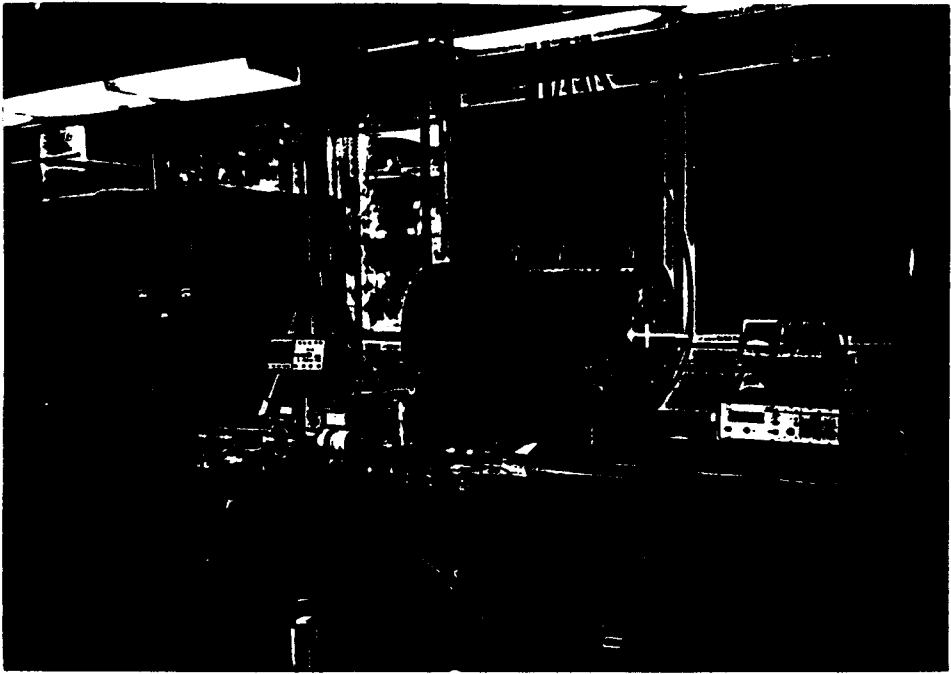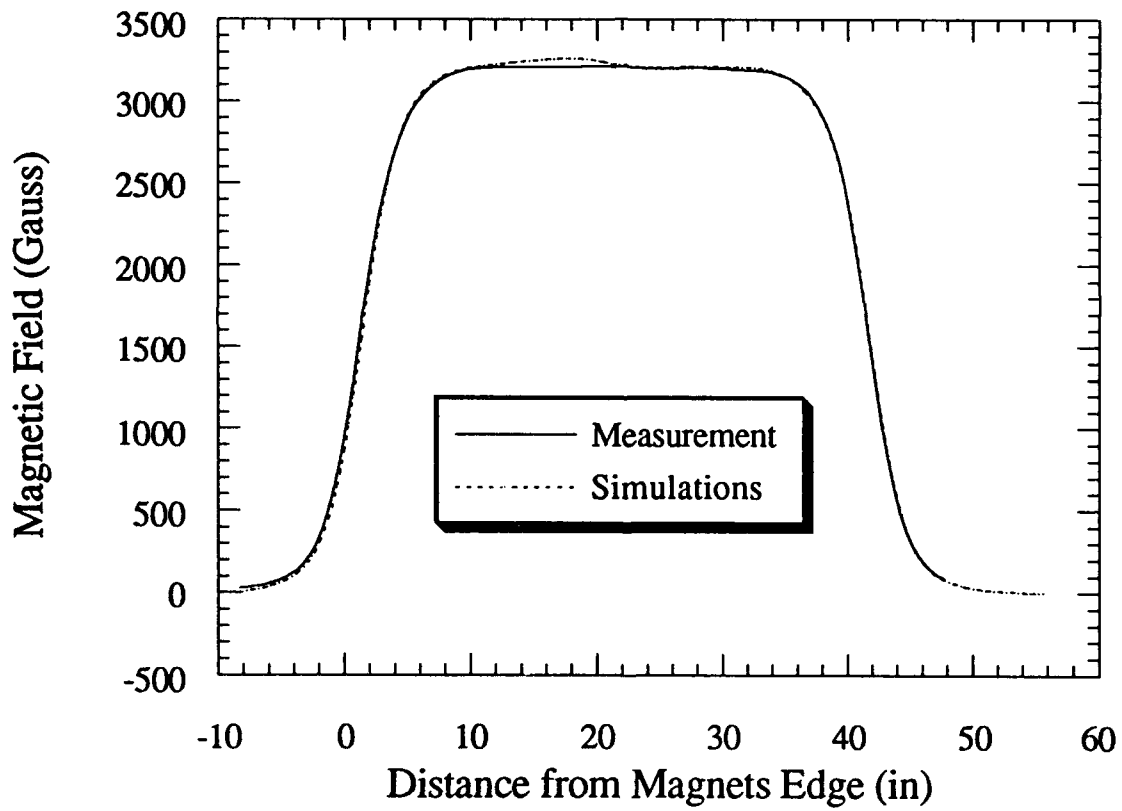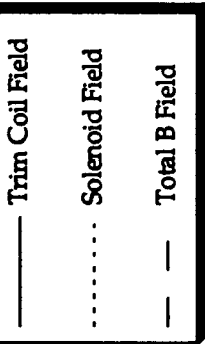
Trim Coil run at 20 KAmp-Turn, with 0.25" iron plate on both sides of the coil.

The right edge of the trim coil is 5" away from the left edge of the solenoid.

(z=0 marks the left edge of solenoid)

The fields shown are 0.225" off the axis

	Trim Coil Field
....	Solenoid Field
— —	Total B Field

Distance along the Axis (inches)

B_z (Gauss)

F/G. /4

FIG. 15

FIG. 16

87